frontiers | Frontiers in Physics

TYPE Review
PUBLISHED 16 September 2024
DOI 10.3389/fphy.2024.1422411

OPEN ACCESS

EDITED BY
Massimo Nocente,
University of Milano-Bicocca, Italy

REVIEWED BY
Guillaume Brochard,
ITER, France
Ruirui Ma,
Southwestern Institute of Physics, China
Yao Yao,
Southwestern Institute of Physics, China

*CORRESPONDENCE
J. Varela,
jacobo.rodriguez@austin.utexas.edu

RECEIVED 24 April 2024
ACCEPTED 12 August 2024
PUBLISHED 16 September 2024

CITATION
Varela J, Spong D, Garcia L, Ghai Y, Ortiz J and FAR3d project collaborators (2024) Stability optimization of energetic particle driven modes in nuclear fusion devices: the FAR3d gyro-fluid code.
Front. Phys. 12:1422411.
doi: 10.3389/fphy.2024.1422411

Stability optimization of energetic particle driven modes in nuclear fusion devices: the FAR3d gyro-fluid code

J. Varela[1]*, D. Spong[2], L. Garcia[3], Y. Ghai[2], J. Ortiz[3] and FAR3d project collaborators

[1]Department of Physics, Institute for Fusion Studies, University of Texas at Austin, Austin, TX, United States, [2]Oak Ridge National Laboratory, Oak Ridge, TN, United States, [3]Department of Physics, Universidad Carlos III de Madrid, Madrid, Spain

The development of reduced models provide efficient methods that can be used to perform short term experimental data analysis or narrow down the parametric range of more sophisticated numerical approaches. Reduced models are derived by simplifying the physics description with the goal of retaining only the essential ingredients required to reproduce the phenomena under study. This is the role of the gyro-fluid code FAR3d, dedicated to analyze the linear and nonlinear stability of Alfvén Eigenmodes (AE), Energetic Particle Modes (EPM) and magnetic-hydrodynamic modes as pressure gradient driven mode (PGDM) and current driven modes (CDM) in nuclear fusion devices. Such analysis is valuable for improving the plasma heating efficiency and confinement; this can enhance the overall device performance. The present review is dedicated to a description of the most important contributions of the FAR3d code in the field of energetic particles (EP) and AE/EPM stability. FAR3d is used to model and characterize the AE/EPM activity measured in fusion devices as LHD, JET, DIII-D, EAST, TJ-II and Heliotron J. In addition, the computational efficiency of FAR3d facilitates performing massive parametric studies leading to the identification of optimization trends with respect to the AE/EPM stability. This can aid in identifying operational regimes where AE/EPM activity is avoided or minimized. This technique is applied to the analysis of optimized configurations with respect to the thermal plasma parameters, magnetic field configuration, external actuators and the effect of multiple EP populations. In addition, the AE/EPM saturation phase is analyzed, taking into account both steady-state phases and bursting activity observed in LHD and DIII-D devices. The nonlinear calculations provide: the induced EP transport, the generation of zonal structures as well as the energy transfer towards the thermal plasma and between different toroidal/helical families. Finally, FAR3d is used to forecast the AE/EPM stability in operational scenarios of future devices as ITER, CFETR, JT60SA and CFQS as well as possible approaches to optimization with respect to variations in the most important plasma parameters.

KEYWORDS

Alfv én Eigenmodes, gyro-fluid, optimization, FAR3d, stability

1 Introduction

Substantial efforts have been dedicated to analysis of the effects of energetic particle components (EP) on plasma stability over several decades, leading to a reasonably good understanding of the phenomena in present day devices. Nevertheless, some open questions still remain with respect to the EP driven instability in burning plasmas, especially with multiple EP populations, as will be present in future fusion reactors. Future fusion regimes will deviate from existing experiments, such as the last Deuterium-Tritium JET campaign, which had only a negligible density of alpha particles. In addition, the consequences of Alfvén Eigenmodes (AE) on the transport of fusion produced alpha particles, energetic hydrogen neutral beams or particle heated using ion cyclotron resonance heating (ICRF) is not well understood yet [1–3]. Experiments in tokamaks as TFTR, JET and DIII-D or stellarators as LHD and W7-AS measured the excitation of AE, leading to a drop of the device performance [4–9]. The resonance of energetic particles with velocities similar or a fraction of the Alfvén velocity can destabilize the plasma driving instabilities that enhance particle losses, leading to a lower heating efficiency, more restrictive operation requirement for plasma ignition and also an enhancement of the EP losses [10–14]. Future fusion devices will require extrapolations to energetic particle distributions that may deviate from present day experiments, with a special attention to the EP gyroradius/minor radius, Alfvén Mach number ($< v_{EP} > / v_{Alfven}$), and EP pressure gradient, placing an emphasis on well-tested simulation methods.

The frequency of EP-driven modes depends on the drive induced by the gradients of the EP distribution function, particularly the density gradient; the dispersion relation of EP-driven instabilities can be expressed by an implicit equation for $\omega + i\gamma$ [15], with ω the frequency and γ the growth rate of the mode. The resonance between EPs and plasma waves can exist even if the EP density is low; that is, the EPs can affect the stability of the plasma even though the amount of EPs in the system is not large enough to overcome the threshold to trigger an EP-driven mode [16, 17]. Indeed, there can be an EP stabilizing effect on thermal plasma instabilities caused by the non-reactive part of the resonance term in the dispersion relation at low EP density. On the other hand, as the EP density increases, the reactive and non-reactive elements compete until the EP-driven branch is destabilized [18]. In case of a resonance with a plasma instability, fish-bones [19, 20] or ballooning modes [21] can be kinetically destabilized. AE modes can also be destabilized in low magnetic field operational regimes if the velocity of injected neutral beams particles or ICRF tails are in the same range as the Alfvén velocity [22, 23], because the AEs frequencies are proportional to the Alfvén velocity and the EP bounce/transit and precessional frequencies scale with the EP velocity. In addition, Alfvén-character oscillations can be induced in tokamak plasmas during ohmic heating phases without NBI or ICRH, presumably by the edge pressure gradient [24–26]. On top of that, AEs can be triggered by electron cyclotron waves (ECW) by fast electrons in the regimes with low collisionality, particularly at the edge of low density plasma [27–31, 330, 331].

Alfvén Eigenmodes are driven in the spectral gaps of the shear Alfvén continua [32, 33], destabilized by super-Alfvénic alpha particles and energetic particles from external sources (e.g., beams, ICRF tails). AE activity has been observed in several different discharge regimes and configurations [34–37]. The different Alfvén eigenmode families (n is the toroidal mode and m the poloidal mode) are linked to frequency gaps produced by periodic variations of the Alfvén speed, for example: toroidicity induced Alfvén Eigenmodes (TAE) couple m with $m + 1$ modes [38–40], beta induced Alfvén Eigenmodes driven by compressibility effects (BAE) [41], Reversed-shear Alfvén Eigenmodes (RSAE) due to local minima in the safety factor q profile [42], Global Alfvén Eigenmodes (GAE) observed in the minimum of the Alfvén continua [14, 43], ellipticity induced Alfvén Eigenmodes (EAE) coupling m with $m + 2$ modes [44, 45], noncircularity induced Alfvén Eigenmodes (NAE) coupling m with $m + 3$ or higher [46, 47] and helical Alfvén Eigenmodes (HAE) where different toroidal modes and helicities (m/n) are coupled [48]. In addition, energetic particle modes (EPMs) can be unstable for frequencies that intersect the shear Alfvén continua if the continuum damping is not strong enough and/or the drive is strong enough to keep them above marginal stability thresholds [49–53].

There are different strategies to improve the AE/EPM stability in nuclear fusion devices. Towards that goal, the destabilizing effect of the EPs can be analyzed with respect to the EP population features, the thermal plasma parameters and the magnetic field configuration. An example is the application of external actuators such as neutral beams (NBI) that can alter the magnetic field topology through the generation of non inductive currents [54, 55]. Neutral beam current drive (NBCD) can be used to achieve steady state operation in advanced tokamaks [56–58] or to modify the magnetic field configuration [59–62]. NBCD can also affect the stability of AEs [63, 64]. Another technique is the injection of ECW [65, 66] that also generate non inductive currents in the plasma. In particular, the electron cyclotron current drive (ECCD) [67–71] can improve the stability of the pressure/current gradient driven modes and AEs in tokamaks [72–77] and stellarators [78–82]. Regarding the thermal plasma parameters, a modification of the thermal ion density changes the plasma Alfvén velocity (defined as $V_A = B/\sqrt{N\mu_0 m_p n_i}$ with B the magnetic field intensity, μ_0 the vacuum magnetic permeability, n_i the thermal ion number density, m_p the proton mass and N the ion species mass/proton ratio) and the AE/EPM stability. The resonance induced by the EPs can be defined with respect to the ratio between the velocity of the EP $V_f = \sqrt{T_{f,i}/N m_p n_i}$ and V_A with $T_{f,i}$ the energy of a given EP population. If V_f/V_A is near unity (or a fraction of) the EP resonance is strong and the EP β AE stability threshold is lower (defined as $\beta_f = 2\mu_0 n_f k_b T_{f,i}/B^2$ with n_f the density of EPs and k_b the Boltzmann constant), leading to the AE destabilization if the EP drive is strong enough (depending on the local gradient of the EP distribution function). In addition, modifying the thermal plasma density changes the EP β because the NBI deposition rate and EP slowing down time are altered. Regarding the thermal plasma temperature, the EP slowing down time (τ_{ep}) is proportional to $T_e^{3/2}/n_e$ with T_e (n_e) is the thermal electron temperature (density) [83]; this explains why EPMs such as the energetic-ion-driven resistive interchange mode (EIC) are stabilized by off-axis ECH injection, which increases the temperature in the plasma periphery [84–86]. Another possibility is modify the operational regime of the NBI by balancing the NBI voltage and power injection while keeping the EP β constant [87, 88] or by displacing the NBI deposition region

outwards [89, 90]. The application of resonant magnetic perturbations (RMPs) in NSTX and LHD has also succeeded in AE stability improvements [91, 92].

The coexistence of multiple EP species also affects the AE stability of fusion devices. This effect was originally observed in early DT experiments on the TFTR device, which had both fusion alpha populations that coexisted with the neutral beam ions used for heating. Alpha particle driven AEs were stabilized by the presence of NBI driven EP species through Landau damping on the lower energy NBI ions. Alpha-drive AEs were only measured at the end of the discharge after the beam injection was turned off [93–95]. Numerical studies using the TAEFL gyrofluid model were used to develop an optimization strategy for the TFTR DT plasma by increasing q_0, resulting in more strongly alpha-driven TAEs through alignment of gap locations with regions of maximum alpha density gradient [96, 97]. The application of this strategy led to discharges in a new reversed shear confinement regime. Similar observations indicating a stabilizing effect of NBI EPs on alpha particle driven modes were reported in JET D-T campaigns [98, 99]. Consequently, there is experimental evidence indicating the AE stability is affected by the presence of multiple EP species. It should be noted that this is not surprising from the theoretical point of view since EP mode stability may depend on the combined contribution of all the EP species, in particular the gradient sign and amplitude of each EP distribution function in the vicinity of the wave-particle resonances in phase space [100]. Numerical studies performed to analyze the AE stability in ITER and CFETR including alpha particle and NBI EP populations show a lower AE growth rate if multiple EP effects are included in the simulations, as compared to single EP species cases [101–103]. In addition, studies of the AE stability in the LHD and DIII-D devices indicate that the combination of multi EP populations (i.e., as generated by different beam line parameters) can lead to important multiple EP effects, and identification of operational scenarios with improved AE stability as the NBI voltage and injection power are varied [104].

The present review is dedicated to summarizing the different strategies that have been used to improve the AE stability in nuclear fusion devices based on comparisons between experiment and numerical models. In particular, the discussion is based on the simulations performed by the gyro-fluid FAR3d code [97, 105–109]. The numerical model, with the appropriate Landau closure relations, solves the reduced non-linear resistive MHD equations including the linear wave-particle resonance effects required for Landau damping/growth [110]. The code follows the evolution of MHD and Alfvén frequency instabilities, based on starting from equilibria, calculated by the VMEC or EFIT codes [111, 112].

The main motivation of performing the analysis with the gyro-fluid code FAR3d is the computational efficiency; this is due to its reduction of selected kinetic effects to a set of 3D fluid-like equations rather than more complex approaches, for example initial value gyrokinetic codes as EUTERPE [113], GEM [114], GYRO [115], GTC [116], ORB5 [117] and GENE [118] or kinetic-MHD hybrid codes as MEGA [119] and M3d-C1 [120]. FAR3d can be used for rapid parameter/profile scans in order to perform optimization/design studies, which are facilitated by the efficient evaluation of physics target functions. Also, the code can be used to identify AE stability trends since critical fast ion characteristics, such as the density profile often cannot directly be measured. It should be noted that the Landau closure model used in the FAR3d code leads to an eigenmode equation, which can be analyzed in similarity to the linear gyrokinetic code LIGKA [121] and the linear kinetic-MHD code MARS-K [122]. Finally, in comparison to particle-based methods, this approach has the advantages of zero noise levels, exact implementation of boundary conditions and an improved ability to include extended mode coupling effects. On the other hand, the simplification of the kinetic effects can lead to a deviation of FAR3d results compared to more complete approaches, although a methodology has been developed for calibrating the Landau-closure against more complete kinetic models through optimization of the closure coefficients [110]. A detailed comparison between FAR3d and other gyro-fluid, gyro-kinetic and hybrid codes was recently performed [123]. Consequently, FAR3d is a tool that complements more complex numerical models by providing a first estimate of AE/EPM linear and non-linear stability, helping to narrow down the parameter selection for the resonance identification with respect to the experimental observations [124]. In addition, the computationally efficient analysis that FAR3d offers can provide a new tool for fast experimental data interpretation and aid in the design of future devices.

This paper is organized as follows. First, a description of the numerical model and simulation parameters is given in Section 2. A description of the research methodology is included in Section 3. The analysis of the AE/EPM activity in different devices is discussed in Section 4. Optimization strategies to minimize the AE/EPM activity is introduced in Section 5. The analysis of the nonlinear AE/EPM saturation phase is done in Section 6. Predictions of the AE/EPM stability in future fusion devices is mentioned in Section 7. The main finding of the FAR3d research lines, the discussion of advantage and drawback of the model and bench-marking with other codes are introduced in Section 8. Next, the conclusions of this paper are presented in Section 9. Finally, ongoing and future research topics as well as projected code updates are commented in Section 10.

2 Numerical model

This section is dedicated to discuss the main features of the FAR3d code. Details of the main model equations, EP distribution function, damping effects and trapped EP operator are introduced. Moreover, the numerical method used to solve FAR3d model is briefly discussed. For a further detailed discussion of the FAR3d code equations and derivation.

2.1 Model equations

The model is based on reduced MHD with acoustic couplings for the thermal plasma and a two-pole (two moments) energetic ion closure model, leading to a six evolution equations for the perturbed poloidal magnetic flux (ψ), toroidal component of vorticity (U), thermal plasma pressure (p_{th}), thermal plasma parallel momentum moment ($\rho_m v_{\parallel th}$), perturbed energetic particle density (n_f) and energetic particle parallel momentum ($m_f n_{f0} v_{\parallel f}$) moments. In the following, the equations are expressed in the vector operator form,

later transformed to Boozer coordinates and normalized for code implementation. The model includes convective nonlinearities in the vorticity, thermal plasma and energetic particle moment equations, $J \times B$ nonlinearity in the vorticity equation, and a $B \cdot \nabla\Phi$ nonlinearity in the magnetic flux evolution equation. These nonlinearities generate effects such as zonal flows, zonal currents, and modification/transport of the energetic particle density that are important in establishing a nonlinear saturated state. The EP destabilizing effect is introduced through the Landau closure terms in the equation for the EP parallel velocity moment and involves the absolute value of the parallel gradient of the parallel velocity moment and the parallel gradient of the EP density. This introduces the phase-mixing associated with the parallel linear Landau resonance ($\omega = k_\parallel v_\parallel$) leading to the destabilization of neutrally stable Alfvén eigenmodes by the EPs. The absolute value of the parallel gradient operator is simplified by the Fourier series representation in toroidal/poloidal angles for all dynamical variables; this allows the poloidal and toroidal gradients to be reduced to a multiplication by mode numbers.

The model formulation assumes high aspect ratio, medium β (of the order of the inverse aspect ratio $\varepsilon = a/R_0$), small variation of the fields and small resistivity. The fluctuating plasma velocity and magnetic field are defined as:

$$\mathbf{v} = \frac{\hat{\mathbf{b}}_{\mathbf{eq}} \times \nabla\boldsymbol{\Phi}}{B}, \qquad \tilde{\mathbf{B}} = \nabla\zeta \times \nabla\tilde{\psi} \tag{1}$$

where ζ is the toroidal angle, Φ the electrostatic potential, and ψ is the perturbed poloidal flux.

The evolution equations of the perturbed quantities are:

$$\frac{\partial\tilde{\psi}}{\partial t} = \frac{R_0}{B}\left(\mathbf{B}_{\mathbf{eq}} \cdot \nabla\boldsymbol{\Phi} + \tilde{\mathbf{B}} \cdot \nabla\boldsymbol{\Phi}\right) + \eta \mathbf{J}_\zeta \tag{2}$$

$$\frac{\rho_m}{\sqrt{g}}\frac{\partial\tilde{U}}{\partial t} = \rho_m \frac{\partial}{\partial t}\left[\nabla \times \left(\sqrt{g}\, v\right)\right]^\zeta = -\rho_m v_{eq}^\zeta \frac{\partial\tilde{U}}{\partial\zeta} - \left[\nabla \times \left(\rho_m \sqrt{g}\, v \cdot \nabla v\right)\right]^\zeta + \left[\nabla \times \sqrt{g}\left(\tilde{J} \times B_{eq} + J_{eq} \times \tilde{B} + \tilde{J} \times \tilde{B}\right)\right]^\zeta - \left[\nabla\sqrt{g} \times \nabla\left(p_{th} + T_f \tilde{n}_f\right)\right]^\zeta + D_U \nabla_\perp^2 \tilde{U} \tag{3}$$

$$\frac{\partial\tilde{p}_{th}}{\partial t} = -v_{eq}^\zeta \frac{\partial\tilde{p}_{th}}{\partial\zeta} - \mathbf{v} \cdot \nabla\tilde{\mathbf{p}}_{\mathbf{th}} - \mathbf{v} \cdot \nabla\mathbf{p}_{\mathbf{th,eq}} + \Gamma\mathbf{p}_{\mathbf{th,eq}}\nabla \cdot \mathbf{v} + \mathbf{D}_{\mathbf{p_{th}}}\nabla_\perp^2\tilde{\mathbf{p}}_{\mathbf{th}} \tag{4}$$

$$\rho_m \frac{\partial\tilde{v}_{\parallel th}}{\partial t} = -\rho_m v_{eq}^\zeta \frac{\partial\tilde{v}_{\parallel th}}{\partial\zeta} - \rho_m \mathbf{v} \cdot \nabla\tilde{\mathbf{v}}_{\parallel\mathbf{th}} - \hat{\mathbf{b}}_{\mathbf{eq}} \cdot \nabla\tilde{\mathbf{p}}_{\mathbf{th}} - \frac{\tilde{\mathbf{B}}}{\mathbf{B}_{\mathbf{eq}}} \cdot \mathbf{p}_{\mathbf{th,eq}} + \mathbf{D}_{\mathbf{v}_{\parallel\mathbf{th}}}\nabla_\perp^2\tilde{\mathbf{v}}_{\parallel\mathbf{th}} \tag{5}$$

$$\begin{aligned}\frac{\partial\tilde{n}_f}{\partial t} = &-v_{eq}^\zeta \frac{\partial\tilde{n}_f}{\partial\zeta} - \mathbf{v} \cdot \nabla\tilde{\mathbf{n}}_{\mathbf{f}} - \boldsymbol{\Omega}_{\mathbf{d}}\left(\tilde{\mathbf{n}}_{\mathbf{f}}\right) - \mathbf{n}_{\mathbf{f0}}\nabla_\parallel\tilde{\mathbf{v}}_{\parallel\mathbf{f}} \\ &-n_{f0}\Omega_d\left(\frac{q_f\Phi}{T_f}\right) + n_{f0}\Omega_*\left(\frac{q_f\Phi}{T_f}\right) + D_{n_f}\nabla_\perp^2\tilde{n}_f\end{aligned} \tag{6}$$

$$\begin{aligned}\frac{\partial\tilde{v}_{\parallel f}}{\partial t} = &-v_{eq}^\zeta \frac{\partial\tilde{v}_{\parallel f}}{\partial\zeta} - \mathbf{v} \cdot \nabla\tilde{\mathbf{v}}_{\parallel\mathbf{f}} - \boldsymbol{\Omega}_{\mathbf{d}}\left(\tilde{\mathbf{v}}_{\parallel\mathbf{f}}\right) \\ &-\sqrt{2}a_1 v_{th,f}|\nabla_\parallel|\tilde{v}_{\parallel f} - 2a_0 T_f \nabla_\parallel\tilde{n}_f \\ &-en_{f0}\Omega_*\left(\frac{\psi}{R_0}\right) + D_{v_{\parallel f}}\nabla_\perp^2\tilde{v}_{\parallel f}\end{aligned} \tag{7}$$

Equation 2 is derived from Ohm's law coupled with Faraday's law, Equation 3 is obtained from the toroidal component of the momentum balance equation multiplied by the operator $\nabla \times \sqrt{g}$, Equation 4 is obtained from the thermal plasma continuity equation with compressibility effects and Equation 5 is obtained from the parallel component of the momentum balance, the Equations 6, 7 are moments of the gyro-kinetic equation for the energetic particles. For more derivation details for the thermal plasma and EP equations. Here ρ_m is the ion mass density, R_0 is the device major radius, η is the plasma resistivity, $\rho = \sqrt{\phi_N}$ the effective radius with ϕ_N the normalized toroidal flux and θ the poloidal angle, $\tilde{J}^\zeta$ is the perturbation of the toroidal current density, $v_{\parallel th}$ is the parallel velocity moment of the thermal plasma and $v_{\zeta,eq}$ is the equilibrium toroidal rotation. n_{f0} is the EP radial density profile. $v_{th,f} = \sqrt{T_f/m_f}$ is the radial profile of the energetic particle average velocity. q_f is the charge, T_f is the radial profile of the effective EP temperature and m_f is the mass of the EP. The parameters a_0 and a_1 are the closure coefficients of the gyro-fluid terms. Each equation has a perpendicular dissipation term normalized to a^2/τ_{A0}. The Ω operators are defined as:

$$\Omega_d = \frac{v_{th,f}^2}{\Omega_c}\frac{\hat{b}_{eq} \times \nabla B_0}{B_0} \cdot \nabla \tag{8}$$

$$\Omega_* = -\frac{T_f}{q_f B_0 n_{f0}}\nabla n_{f0} \cdot \hat{b}_{eq} \times \nabla \tag{9}$$

Here the $\Omega_d = v_d \cdot \nabla$ operator models the average drift velocity of passing particles (v_d is the drift velocity) and Ω_* models the diamagnetic drift frequency. Here, $v_{th,f}^2 = T_f/M_f$ and $\Omega_c = q_f B/M_f$.

We also define the parallel gradient, perpendicular gradient squared (lowest order) and curvature operators as

$$\nabla_\parallel = \hat{b}_{eq} \cdot \nabla, \tag{10}$$

$$\nabla_\perp^2 = \left(\nabla - \nabla_\parallel\right)^2 \tag{11}$$

with the Jacobian of the transformation,

$$\sqrt{g} = \frac{B_0}{R_0}\frac{J - \iota I}{B^2}. \tag{12}$$

with *iota* the rotational transformation profile.

Equations 4, 5 introduce the parallel momentum response of the thermal plasma. These are required for coupling to the geodesic acoustic waves, accounting for the geodesic compressibility in the frequency range of the geodesic acoustic mode (GAM) [110]. The coupling between the equations of the EP and thermal plasma is done in the equation of the perturbation of the toroidal component of the vorticity (Equation 3) introducing the EP destabilizing effect caused by the gradient of the fluctuating EP density/pressure.

Equilibrium flux coordinates (ρ, θ, ζ) are used. Here, ρ is a generalized radial coordinate proportional to the square root of the toroidal flux function, and normalized to the unity at the edge. The flux coordinates used in the code are those described by Boozer [125], and $\sqrt{g}$ is the Jacobian of the coordinate transformation. All functions have equilibrium and perturbation components represented as: $A = A_{eq} + \tilde{A}$.

Two versions of the FAR3d code have been developed: nonlinear and linear. The linear version is designed to solve the linearized system of equations, facilitating the study of linear phases of different instabilities and phenomena (e.g., determining growth rates, spatial scales, and frequencies), and enabling rapid parametric studies to explore the parameter space associated with each magnetic equilibrium computed via equilibrium codes. The

10.3389/fphy.2024.1422411

nonlinear version is dedicated to study the instabilities saturation phase and their long-term behavior, providing information of the EP transport induced by AEs and thermal plasma instabilities, the generation of zonal structures as well as nonlinear couplings between perturbations and thermal plasma, different toroidal mode families and EP species. The nonlinear version utilizes MPI parallelization over toroidal mode groups for the linear solver and over radial domains for the nonlinear convolution products coupled with OpenMP parallelization over loops; a GPU-based version has also been recently developed.

Two numerical schemes to solve the linear equations can be used in the code: a semi-implicit initial value or an eigenvalue solver. The initial value solver calculates the mode with the largest growth rate (dominant mode) and the eigen-solver provides both the stable and unstable modes (sub-dominant modes). The eigensolver uses a Jacobi-Davidson algorithm, which allows solutions near targeted values of frequency/growth rate. The analysis of the sub-dominant modes is required to calculate the growth rate of the multiple AE families that can be unstable or marginally unstable during the discharge. In addition, the study of the sub-dominant modes is motivated by the fact that the equilibrium profiles are not known precisely from the experiment. This can result in a more close correspondence of sub-dominant modes with the experimentally observed modes than the fastest growing mode. In this way, the eigenmode can provide an uncertainty characterization both in the modeling and the measurements.

A finite difference method is applied for the radial discretization, while Fourier expansions are used for poloidal and toroidal directions. The numerical scheme employs semi-implicit discretization for linear terms and explicit one for nonlinear terms using a two semi-step method to ensure $(\Delta t)^3$ accuracy (Adams-Moulton predictor-corrector method [126]).

2.2 Trapped EP approximation

The effect of helically or toroidally trapped EPs are introduced in the model through modification of the average drift velocity operator normally designed to model passing EP average drifts). Using the expressions 6.72, 6.77 and 6.83 of the Ref. [127], the trapped EP trajectory can be derived in the $\rho-\theta$ plane, described by the period of the guiding center motion in the helical or toroidal ripple (T) and the second adiabatic invariant Λ, called action in classical mechanics and defined as the integral of the Poisson brackets of the canonical conjugate position and momentum vectors of the EP guiding center along the magnetic field line:

$$\Lambda = \int_{\zeta_-}^{\zeta_+} \hat{b}_{eq,\zeta} \cdot p d\zeta = 2B_{eq,\zeta} \int_{\zeta_-}^{\zeta_+} \frac{m v_\parallel}{B_0} d\zeta = \frac{4\tilde{\psi}}{a^2\sqrt{g}} \int_{\zeta_-}^{\zeta_+} \frac{m v_\parallel}{B_0} d\zeta \tag{13}$$

Here, $B_{eq,\zeta} = 2\tilde{\psi}/(a^2\sqrt{g})$. Thus, the averaged drift equations of the trapped EP can be derived from the expression:

$$m\frac{d\rho}{dt} = \frac{1}{R_0}\frac{\partial \Lambda}{\partial \theta} = \frac{1}{R_0}\frac{4\tilde{\psi}}{a^2}\frac{\partial}{\partial \theta}\left(\frac{1}{\sqrt{g}}\int_{\zeta_-}^{\zeta_+} \frac{m v_\parallel}{B_0} d\zeta\right) \tag{14}$$

$$mR_0\frac{d\theta}{dt} = -\frac{\partial \Lambda}{\partial \rho} = \frac{1}{R_0}\frac{4\tilde{\psi}}{a^2}\frac{\partial}{\partial \rho}\left(\frac{1}{\sqrt{g}}\int_{\zeta_-}^{\zeta_+} \frac{m v_\parallel}{B_0} d\zeta\right) \tag{15}$$

The bounce length of the guiding center (d_b) is defined as:

$$d_b = \frac{4\tilde{\psi}}{a^2\omega_b}\int_{\zeta_-}^{\zeta_+} \frac{v_\parallel}{B_0} d\zeta = \frac{4\tilde{\psi}}{a^2\omega_b} \lim_{\Delta\zeta\to\infty} \sum_{\zeta_-}^{\zeta_+} \frac{v_\parallel}{B_0} d\zeta \tag{16}$$

Here, $\omega_b = 1/2\pi T$ is the bounce frequency of the guiding center. The experimental data indicates that the EP participating in the resonance have specific velocity-space characteristics. Thus, for simplicity we assume that the velocity-space properties of the EP involved in the resonance can be modeled by the guiding center bounce frequency and length. The trapped EP orbit topology can be determined by the variables $(p_\parallel, \mu, E)$, the canonical momentum along the magnetic field line, the magnetic moment and the kinetic energy, respectively. The present approximation assumes the kinetic energy of the trapped EP integrated along the path is conserved. In addition, because the EPs participating in the resonance have specific velocity-phase properties, the model only considers EPs with a given EP velocity and pitch. The trapped EP velocity is functionally related to the bounce velocity and the pitch angle by the bounce distance. Consequently, the approximation is based in the following transformation:

$$(p_\parallel, \mu, E) \to \left(v_b, d_b, \int_0^T \int_0^{d_b} E d\zeta dt\right) \tag{17}$$

fixed the canonical and magnetic momentum of the trapped EP participating in the resonance. The bounce velocity and distance are linked to the parallel canonical and magnetic momentum as:

$$v_b^2 = v_\parallel^2 + v_\perp^2 = \frac{2\mu B}{m} + \left(\frac{p_\parallel B}{m B_\zeta}\right) \tag{18}$$

$$d_b = \frac{d_\parallel}{cos(\alpha)} = \frac{2\pi v_\parallel}{\omega_b cos(\alpha)} \tag{19}$$

with the pitch angle of the trapped EP defined as $\alpha = tan^{-1}(v_\perp/v_\parallel)$. Consequently, the magnetic momentum and kinetic energy of the trapped EP analyzed can be parameterized in terms of the bounce distance and frequency as:

$$\mu = d_b^2\omega_b^2 m\left(\frac{2\pi^2}{B} - \frac{B cos^2(\alpha)}{8\pi^2 B_\zeta^2}\right) \tag{20}$$

Now, the expression of the bounce length is replaced in the Equations 14, 15, extracted from the integral by assuming, as first order approximation, no radial or angular dependency of the bounce length is included in the model, thus:

$$\frac{d\rho}{dt} = \omega_b d_b \frac{\partial}{\partial \theta}\left(\frac{1}{\sqrt{g}}\right) = \frac{v_b}{2\pi}\frac{\partial}{\partial \theta}\left(\frac{1}{\sqrt{g}}\right) \tag{21}$$

$$\frac{d\theta}{dt} = -\omega_b d_b \frac{\partial}{\partial \psi}\left(\frac{1}{\sqrt{g}}\right) = -\frac{v_b}{2\pi}\frac{\partial}{\partial \psi}\left(\frac{1}{\sqrt{g}}\right) \tag{22}$$

defining the bounce velocity of the guiding center as $v_b = 2\pi\omega_b d_b$, the drift equations can be reformulated as:

$$v_b = 2\pi\rho\left[\int_{t_-}^{t_+} \frac{\partial}{\partial \theta}\left(\frac{1}{\sqrt{g}}\right) dt\right]^{-1} = -2\pi\theta\left[\int_{t_-}^{t_+} \frac{\partial}{\partial \rho}\left(\frac{1}{\sqrt{g}}\right) dt\right]^{-1} \tag{23}$$

Next, the Jacobian is extracted from the integral because it is an equilibrium variable independent of the time. Consequently:

$$\int_{t_-}^{t_+}\frac{\partial}{\partial\theta}\left(\frac{1}{\sqrt{g}}\right)dt=\frac{\partial}{\partial\theta}\left(\frac{1}{\sqrt{g}}\right)\int_{t_-}^{t_+}dt=\frac{\partial}{\partial\theta}\left(\frac{1}{\sqrt{g}}\right)T \tag{24}$$

The modified operator to describe the averaged drift velocity of the trapped particles ($\Omega_{d,trap}$) is defined by taking the ratio of the bounce frequency of the trapped particles with respect to the averaged frequency of the passing particle orbit along the torus $\omega_\parallel = v_{th,f}/(2\pi R_0)$:

$$\begin{aligned}\Omega_{d,trap}&=\frac{\omega_b}{\omega_\parallel}\Omega_d=\frac{v_b}{2\pi d_b}\frac{2\pi R_0}{v_{th,f}}\Omega_d\\&=\frac{2\pi\rho}{2\pi d_b}2\pi\omega_b\frac{2\pi R_0}{v_{th,f}}\left[\frac{\partial}{\partial\theta}\left(\frac{1}{\sqrt{g}}\right)\right]^{-1}\Omega_d\end{aligned} \tag{25}$$

thus, the modified operator of the drift velocity of the trapped particles is (after normalization):

$$\Omega_{d,trap}=\frac{4\pi^2\rho\omega_b}{v_{th,f}d_b}\left[\frac{\partial}{\partial\theta}\left(\frac{1}{\sqrt{g}}\right)\right]^{-1}\Omega_d \tag{26}$$

The new drift velocity operator includes information of the bounce frequency and length of the guiding center of the trapped EP. Using the correct set of bounce frequency and length values the resonance induced by barely or deeply trapped EP can be approximated. In addition, a first order estimation of the resonance caused by EPs with different pitch angles can be obtained.

2.3 EP distribution function

The FAR3d two-moment gyro-fluid model is based on a two-pole approximation to the resonant response function (equivalent to a Lorentzian distribution function) that can be approximately matched to a Maxwellian or to a slowing-down distribution by choosing an equivalent average energy. The EP distribution in the model is a Maxwellian which has the same second moment, the effective EP temperature, as that of the equivalent slowing-down distribution defined below [128, 129]:

$$\begin{aligned}f_{SD}=&\frac{\tau_s}{v^3+v_c^3}\left(\frac{v^3}{v^3+v_c^3}\right)^{b/3}\\&\int_\infty^v\left(\frac{v'^3}{v'^3+v_c^3}\right)^{-b/3}S(v')dv'^3\end{aligned} \tag{27}$$

and the Maxwellian distribution as:

$$f_{Max}=N_M e^{\frac{-mv^2}{K_BT}} \tag{28}$$

where $v_c=(3\sqrt{\pi}\,m_e/4m_i)^{1/3}\cdot v_e$, with m_e the electron mass, m_i the ion mass and v_e the electron velocity, and $v_{EP,NBI}=\sqrt{2E_{EP,NBI}/m_{EP,NBI}}$ the beam particles velocity with $E_{EP,NBI}$ the beam particles energy and $m_{EP,NBI}$ the beam particles mass. τ_s is the slowing down time, b is a dimensionless parameter that indicates the effect of transport, N_M is defined as $(m/2\pi KT)^{3/2}$ and $S(v)$ is the source term of the EPs. For simplicity, we consider the effect of the transport negligible, a mono-energetic source and an isotropic distribution function, thus:

$$f_{SD}=\frac{S_0\tau_s}{4\pi}\frac{1}{v^3+v_c^3}H(v-v_{EP,NBI}) \tag{29}$$

with $H(v-v_{EP,NBI})$ Heaviside function. The averaged square velocity of the slowing down and Maxwellian distribution is selected to be the same ($\langle v^2\rangle_{Max}=\langle v^2\rangle_{SD}$), where the averaged square velocity is defined as:

$$\langle v^2\rangle=\frac{\int_V fv^2dv^3}{\int_V fdv^3} \tag{30}$$

The assumption of the model is that the averaged Maxwellian energy can be matched to the thermalized energy of the EP, thus:

$$\begin{aligned}\langle v^2\rangle_{Max}&=\frac{\left(\frac{K_BT_f}{m_f}\right)^{5/2}\int_0^\infty e^{-x^2}x^{5/2}dx}{\left(\frac{K_BT_f}{m_f}\right)^{3/2}\int_0^\infty e^{-x^2}x^{3/2}dx}\\&\approx\frac{K_BT_f}{m_f}\approx v_{th,f}^2\end{aligned} \tag{31}$$

with $x^2=\frac{m_fv^2}{K_BT_f}$, where:

$$\langle v^2\rangle_{SD}=\frac{\int_0^{v_{EP,NBI}}\frac{v^4dv}{v^3+v_c^3}}{\int_0^{v_{EP,NBI}}\frac{v^2dv}{v^3+v_c^3}}=v_c^2\frac{\int_0^{v_{EP,NBI}/v_c}\frac{x^4dx}{x^3+1}}{\int_0^{v_{EP,NBI}/v_c}\frac{x^2dx}{x^3+1}} \tag{32}$$

with $x=v/v_c$. Consequently, if the electron temperature is 1 keV:

$$T_f=0.573E_{NBI} \tag{33}$$

Here, T_f is a radial profile. The consequence of these simplifications is that the EP model requires performing parametric studies with respect to the EP energy and β to reproduce the resonances triggered by a slowing down or any other kind of EP distribution function. Consequently, a set of Maxwellian EP distributions is used to approach the resonance induced by a given EP distribution function. It should be noted that not all the resonances identified by the simulations may be equivalent to the destabilization of AEs in the experiment, because the drive is determined by the gradient of the phase space distribution and the gradient depends on the phase space shape of the distribution function of the EP. Nevertheless, this information is useful for optimization studies and a first characterization of the AE/EPM activity measured in the experiments. In addition, the simulations cannot distinguish co- and ctr-EP using a single Maxwellian because the Maxwellian distribution function is symmetric and the reduced MHD model contains AEs propagating in both directions along magnetic field lines. This leads to an equal destabilization of modes with the same growth rate and frequency although opposite propagation directions. Again, this limitation is approximately corrected by performing parametric studies.

2.4 Damping effects

EP FLR effects in the gyrokinetic equation and gyro-Landau closure model enter in through the functions Γ and $1-\Gamma$ with:

$$\Gamma=e^{-k_\perp^2\rho_i^2}I_0\left(k_\perp^2\rho_i^2\right) \tag{34}$$

here, ρ_i is the gyro-radius, $k_\perp$ the perpendicular wavenumber ((which is treated in this model as a differential operator) and I_0

the modified Bessel function. Using Padé approximations, these can be approximated for $k_\perp \rho_i \leq 1$ as [108, 130]:

$$\Gamma = \frac{1}{1 + k_\perp^2 \rho_i^2} \tag{35}$$

$$1 - \Gamma = \frac{k_\perp^2 \rho_i^2}{1 + k_\perp^2 \rho_i^2} \tag{36}$$

These operators can be inverted by identifying $k_\perp^2 \rho_i^2$ as $-\rho_i^2 \nabla_\perp^2$, defining functions Q and W as (based on how the FLR terms occur in the evolution equations):

$$Q = \Gamma \psi \tag{37}$$

$$W = (1 - \Gamma)\phi \tag{38}$$

Then, after multiplying through by $1 + k_\perp^2 \rho_i^2$ two auxiliary equations can be added:

$$0 = \left(1 - \rho_i^2 \nabla_\perp^2\right) W + \nabla_\perp^2 \phi \tag{39}$$

$$0 = \left(1 - \rho_i^2 \nabla_\perp^2\right) Q - \psi \tag{40}$$

that define the functions W and Q in terms of the evolving dynamical variable ϕ and ψ. The contribution of the thermal ion FLR damping effect is included in the equations of the poloidal flux $(\tilde{\psi})$ and the vorticity $(\tilde{U})$ following the derivation in the references:

$$\frac{\partial \tilde{\psi}}{\partial t} = \ldots + \rho_i^2 \sqrt{\frac{\pi}{2}} \frac{v_A^2}{v_{Te}} |\nabla_\parallel| \nabla_\perp^2 \tilde{\psi} \tag{41}$$

$$\frac{\partial \tilde{U}}{\partial t} = \ldots + \omega_r \rho_i^2 \nabla_\perp^2 \tilde{U} \tag{42}$$

with ρ_i normalized to the minor radius, the Alfvén velocity (v_A) and thermal velocity (v_{Te}) normalized to the Alfvén velocity at the magnetic axis and the ω_r the target AE frequency normalized to the Alfvén time. The contribution of the EP FLR effect is included in the equations of the EP density $(\tilde{n}_f)$ and parallel velocity $(\tilde{v}_{\parallel,f})$:

$$\frac{\partial \tilde{n}_f}{\partial t} = \ldots + \epsilon^2 \omega_r \omega_{cy} \frac{n_{f0}}{v_{th,f}^2} W - n_{f0} \Omega_* (W) \tag{43}$$

The EP FLR term in the parallel velocity moment equation is:

$$\frac{\partial \tilde{v}_{\parallel,f}}{\partial t} = \ldots + v_{th,f}^2 \frac{1}{J - + I} \frac{1}{n_{f0}} \frac{1}{\rho} \frac{dn_{f0}}{d\rho} (IX_1 - JX_2) \tag{44}$$

with J the poloidal current, I the toroidal current, $-\iota$ the rotational transform and X_1, X_2 the auxiliary variables given by the Pade approximation. Thus, two new equations are added to the numerical model:

$$\left(1 - \rho_f^2 \nabla_\perp^2\right) X_1 - \frac{\partial \tilde{\psi}}{\partial \zeta} = 0 \tag{45}$$

$$\left(1 - \rho_f^2 \nabla_\perp^2\right) X_2 - \frac{\partial \tilde{\psi}}{\partial \theta} = 0 \tag{46}$$

The contribution of the electron-ion Landau damping effect is included in the vorticity equation through a term of the form:

$$\frac{\partial \tilde{U}}{\partial t} = \ldots - \frac{\beta_{0i}}{2\epsilon^2 \omega_r} \frac{T_i}{T_e} p_{i,eq} (S_{ei})_{imag} \Omega_d^2 (\Phi) \tag{47}$$

with β_{0i} the thermal ion β at the magnetic axis, T_i/T_e the ratio of the ion and electron temperature, $p_{i,eq}$ the equilibrium pressure of the thermal ions and $(S_{ei})_{imag}$ the imaginary component of the e-i damping term. The complete definition of $(S_{ei})_{imag}$ is written in [108].

2.5 Simulation equilibria and parameters

FAR3d can use equilibria calculated by either the VMEC or EFIT codes [111, 112]. VMEC and EFIT data is first transformed to Boozer coordinates; then, the metric elements and various combinations of equilibrium magnetic data are produced as input to FAR3d.

The main profiles of the model require an initial input that can be introduced using analytical expressions or experimental data, particularly the thermal electron/ion density and temperature, EP density and energy as well as the equilibrium toroidal plasma rotation (Doppler effect).

The dynamic and equilibrium toroidal and poloidal modes used in the simulations are chosen to resolve the range of surfaces that characterize the instability of interest. In linear simulations, the equilibrium modes ($n = 0 + iN$ with N the number of device periods and i an integer) represent the magnetic steady-state configuration and do not evolve in time. On the other hand, the equilibrium components in nonlinear simulations can be allowed to evolve, capturing the feedback between thermal plasma and EP profiles required to study the generation of profile flattening effects, and zonal structures during the saturation phase of AE/EPM. Dynamic modes represent the perturbations evolving in time in both linear and nonlinear simulations.

The dynamic variables add both mode parities because the moments of the gyro-kinetic equation break the MHD symmetry. The convention used by the code for the Fourier decomposition is, taking the example of the pressure: $n > 0$ represents the $cos(m\theta + n\zeta)$ and $n < 0$ the $sin(m\theta + n\zeta)$. The eigenfunctions (f) representation is done with respect to the sine and cosine components:

$$\begin{aligned} f(\rho, \theta, \zeta, t) = &\sum_{m,n} f_{mn}^s (\rho, t) sin(m\theta + n\zeta) \\ &+ \sum_{m,n} f_{mn}^c (\rho, t) cos(m\theta + n\zeta) \end{aligned} \tag{48}$$

The same way, the eigenfunction can be also expressed in terms of real (R) and imaginary (I) components:

$$\mathrm{Re}[f(\rho, \theta, \zeta, t)] = \mathrm{Re}\left[\sum_{m,n} \left(f_{mn}^R (\rho) + i f_{mn}^I (\rho)\right) (cos\omega_R t - isin\omega_R t) e^{i(m\theta + n\zeta)}\right] \tag{49}$$

Equilibrium variables also may include both parities if up-down asymmetric configurations are analyzed (e.g., a tokamak with a single-null divertor).

It should be noted that for all of the cases discussed it is assumed that the AE/EPM are destabilized by passing EP, that is to say, the pitch angle of the EPs is assumed to be zero. The only exception is the analysis of the EIC in LHD plasma including the trapped EP approximation. A detail analysis of the EP-driven mode stability with respect to the EP bounce distance and frequency is performed in Ref. [131]. The analysis identifies a resonance leading to the destabilization of a 1/1 instability in the plasma periphery with a

frequency around 4 kHz if the EP bounce distance is $d_b/R_0 > 0.01$ and the bounce frequency is $\omega_b < 80$ kHz ($v_b < 2.3 \cdot 10^3$ m s^{-1}). Studies using the 3D Monte Carlo code GCR [132], tracking the guiding center of the helically trapped EP, show the bounce length is several centimeters and the bounce frequency is ≤ 100 kHz, thus $v_b \approx 2.3 \cdot 10^3$ m s^{-1}, consistent with the resonance regime of helically trapped EP, not deeply helically trapped EP. In the analysis of the linear and nonlinear stability of the EICs, the parameters selected for the hellicaly trapped EP are: $\omega_b < 40$ kHz, $d_b = 0.072$ m and $v_{th,f}/v_{A0} = 0.25$.

3 Analysis methodology

Fast tools dedicated to analyze the AE/EPM stability are required to provide timely support/interpretation during and in between experimental campaigns. It is well know there is a time gap between theoretical analysis and experimental results caused by the large computational demand of gyro-kinetic and hybrid codes as well as the accuracy of the input data (profiles, equilibrium, realistic EP distributions, etc), leading to a time-lag between experimental group observations and theory attainments. Reduced models can cover this gap providing a first characterization of the AE/EPM activity observed in the experiment as well as useful information of the AE/EPM stability trend with respect to the main operation parameters of the device.

The FAR3d code is routinely used in several research institutions as a means to provide theoretical support for experimental groups in the analysis of the AE/EPM activity. FAR3d studies consist in identifying the EP resonance that causes the destabilization of the AE/EPM by comparing code output and experimental data. A successful instability identification requires the dominant modes, frequency range, radial location and eigenfunction structure obtained in the linear simulations must be consistent with the experimental observations. Towards that aim, the simulation results are compared with the magnetic fluctuations measured by Mirnov coils or Langmuir probes ($\tilde{B}$), electron density ($\tilde{n}_e$) and temperature fluctuations ($\tilde{T}_e$) from electron cyclotron emission (ECE) plus Thomson scattering diagnostics, heavy ion beam probe diagnostic measurements of the plasma electrostatic potential ($\tilde{\Phi}$) and tomographic reconstructions of the instability using soft X-ray diagnostics. Several examples are provided in the Section 4.

Once the AE/EPM activity in the experiment is reproduced, the next step of the analysis consist in the identification of operation scenarios with reduced AE/EPM activity. On that aim, parametric studies are performed to identify optimization trends with respect to different simulation variables directly connected to experimental parameters. The analysis provides information about configurations that may show improved AE/EPM stability. Promising operational scenarios that can be explored in the device are suggested and dedicated experiments are performed. Some examples of these studies are discussed in Section 5.

Linear simulations are useful to identify the instabilities that can be triggered in a given configuration but not how such perturbations will evolve in time, that is to say, no information of the instability saturation is provided. Consequently, it is mandatory performing nonlinear simulations to study the saturation phase of AE/EPM, in particular the induced EP transport, the energy exchange between different toroidal/helical families and the thermal plasma as well as the generation of zonal structures. There is experimental evidence of the important effects of the AE/EPM saturation on the confinement of nuclear fusion devices, in particular the bursting activity which is characterized by transitory strong magnetic fluctuations and large EP losses. Such instabilities are caused by presence of a wide single AE/EPM or the overlapping of individual AEs/EPMs. This kind of analysis is included in Section 6.

Another topic to study is forecasting possible AE/EPM stability issues of future devices, in particular if the device is able to explore reactor relevant configurations. This is the case of devices as JT60SA, ITER or DEMO. In addition, smaller devices dedicated to explore interesting magnetic field symmetries are also explored, identifying the benefits of such symmetries on the plasma AE/EPM stability. Such studies are introduced in Section 7.

4 Identification of AE/EPM

The first applications of the FAR3d code were dedicated to analyze the AE stability in the stellarators LHD and TJ-II. These devices use tangential NBIs to heat the plasma by injecting neutrals up to 180 keV in the case of LHD and 40 keV in the case of the TJ-II plasma [133, 134]. In addition, LHD can also heat the plasma periphery using perpendicular NBIs by injecting 32 keV neutrals. Strong NBI injection leads to the destabilization of AE/EPM in LHD [53, 135–137] and in TJ-II discharges [138, 139]. In the following, a mode is identified as a AE if the perturbation eigenfunction is fully located in the frequency range and radial location of an Alfvén gap. On the other hand, a mode is identified as an EPM if the perturbation eigenfunction crosses the continuum and the maximum of the mode amplitude is located inside the continuum.

4.1 Stellarator: large helical device

The EP resonance is particularly intense in LHD operation scenarios with low magnetic field and density, leading to the destabilization of AEs if the plasma is strongly heated by the tangential NBIs. Particularly, high thermal β discharges in the LHD inward shifted configurations with low magnetic fields (≈ 0.5 T) show a sudden increase of the MHD activity measured by the Mirnov coils in the frequency range of the 40 – 80 kHz, combined with an enhancement of the EP fluxes measured by the tangential neutral particle analyzer (NPA) (see Figure 9 of Ref. [140]), particularly EPs with energies around 135 keV. Such MHD activity is identified with the destabilization of a AE burst. The analysis of the continuum gap structure and EP distribution function indicates the destabilization of an $n/m = 1/1 - 1/2$ TAE in the middle-outer plasma region (see Figure 10 of Ref. [140]). In addition, the frequency spectra show multiple signals pointing out the destabilization of several AEs. TAE bursts were originally observed in hydrogen plasma heated by hydrogen NBIs, although recent experiments showed the destabilization of TAE burst in deuterium plasma [141]. The FAR3d study was dedicated to analyze the modes destabilized in the experiment, identifying unstable $n = 1$ and 2 TAEs in the frequency range of 50–80 kHz,

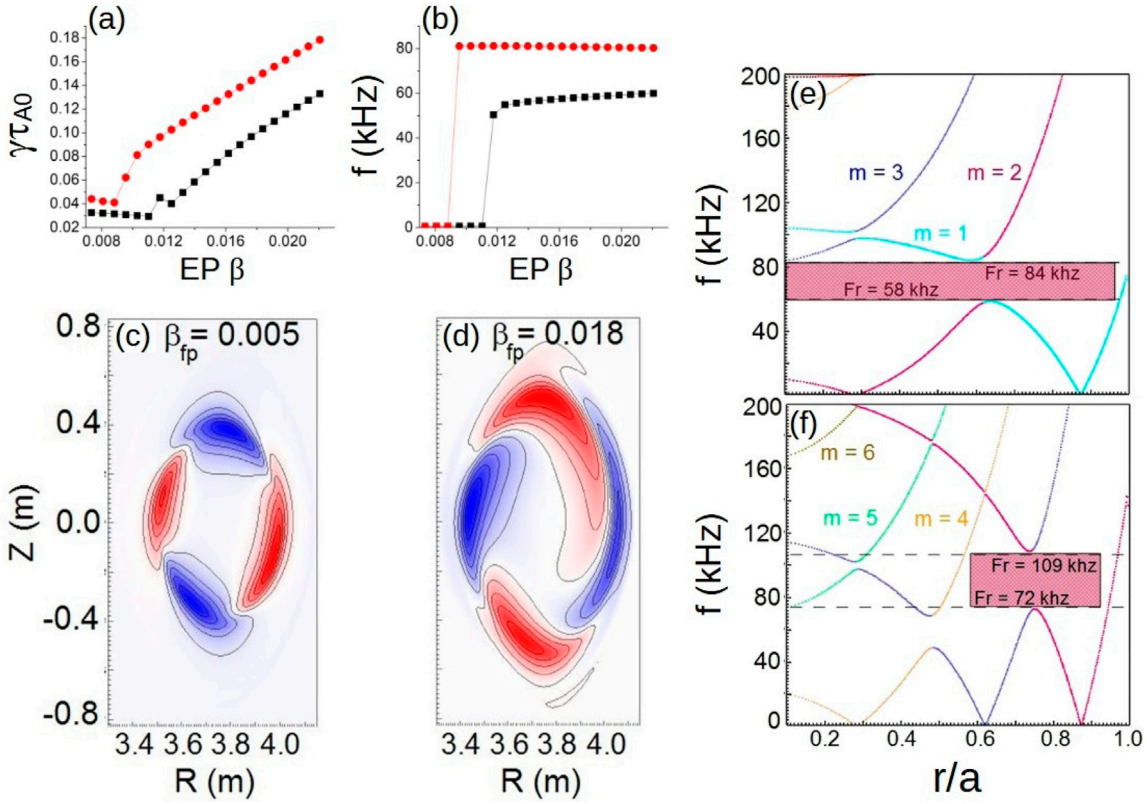

FIGURE 1
Analysis of TAE stability in LHD plasma. Growth rate **(A)** and frequency **(B)** of $n = 1$ and $n = 2$ TAEs for different EP β values. 2D plots of the electrostatic potential of $n = 1$ perturbation if the EP β is **(C)** 0.005 and **(D)** 0.018. Alfvén gaps of **(E)** $n = 1$ and **(F)** $n = 2$ toroidal modes. Reproduced courtesy of IAEA, IOPScience, Nuclear Fusion journal. Figure adapted from [109]. Copyright (2017) IAEA.

consistent with the experimental observations [109]. Figure 1, panels a and b, indicates the growth rate and frequency of $n = 1$ and $n = 2$ TAEs in the range of β_f values similar to the experiment, indicating a critical EP $\beta = 0.012$ for $n = 1$ TAE and 0.01 for $n = 2$ TAE. Similar results are obtained in simulations performed by the MEGA code [142, 143]. Panels c and d indicate the transition from a $n = 1$ pressure gradient driven mode (PGDM) to a TAE as the EP β of the simulation increases. The TAE destabilization leads to a wider perturbation, up-down asymmetric patterns and the poloidal rotation of the mode. Panels e and f show wide Alfvén continuum gaps covering all the normalized plasma radius in the frequency range of 58–84 kHz for the $n = 1$ toroidal mode family, displaced to the middle-outer plasma region and the frequency range of 72–109 kHz for the $n = 2$ toroidal mode family, consistent with the radial location and frequency range of the TAEs calculated by FAR3d. Alfvén continuum gaps are calculated using the Stellgap code [144]. It should be noted that Stellgap simulations are performed from the first to the last flux surface of the equilibrium. No extrapolations are applied between the magnetic axis and the first flux surface; for this reason no information on the radial gap structure is included in the figures between the magnetic axis and the first flux surface.

Another dangerous instability observed in LHD plasma is the energetic-ion-driven resistive interchange mode (EIC), destabilized in discharges with low density and high ion temperature if the plasma is heated by perpendicular and tangential NBIs; these show magnetic fluctuations similar to the fishbone oscillations [84, 145]. In these discharges, the β of the thermal plasma is small due to the low electron density and the large magnetic field strength, comparable with the β of the EP injected by the perpendicular NBI ($\beta_{f,\perp}$). EIC events are observed as a bursting instability with a frequency around 9 kHz triggered nearby the rational surface $n/m = 1/1$ at the plasma periphery if the perpendicular NBI injection overcomes some threshold, chirping down to 4 kHz before stabilization [85]. Additionally, previous studies pointed out that the resistive interchange modes (RIC) are unstable in the magnetic hill region of LHD [1, 146–149]. The RIC can resonate with the precessional motion of the helically trapped EP generated by the perpendicular NBI in the range of $f = 10$ kHz, leading to the enhancement of the EP radial transport [150, 151]. Such an instability was identified as the trigger of the EIC events [84, 85]. Consequently, EIC events can be grouped into the family of the energetic partile modes (EPM). The FAR3d code was used to analyze the destabilizing effect of helically trapped EPs during an EIC event, identifying the threshold of the perpendicular NBI injection intensity required to destabilize the EIC [131]. Figure 2, panel a, shows the frequency of the perturbation driven by the $n = 1$ toroidal family (black line) and the helical family $n = 1, 9, 11$ (red line), identifying the $\beta_{f,\perp}$ threshold to destabilize the EIC as 0.0028 for $n = 1$ toroidal family, although it is 0.0032 for the helical family $n = 1, 9, 11$, pointing out that EIC could be first destabilized by the 1/1 mode and, if $\beta_{f,\perp}$ further increases, the $n = 1, 9, 11$ helical family

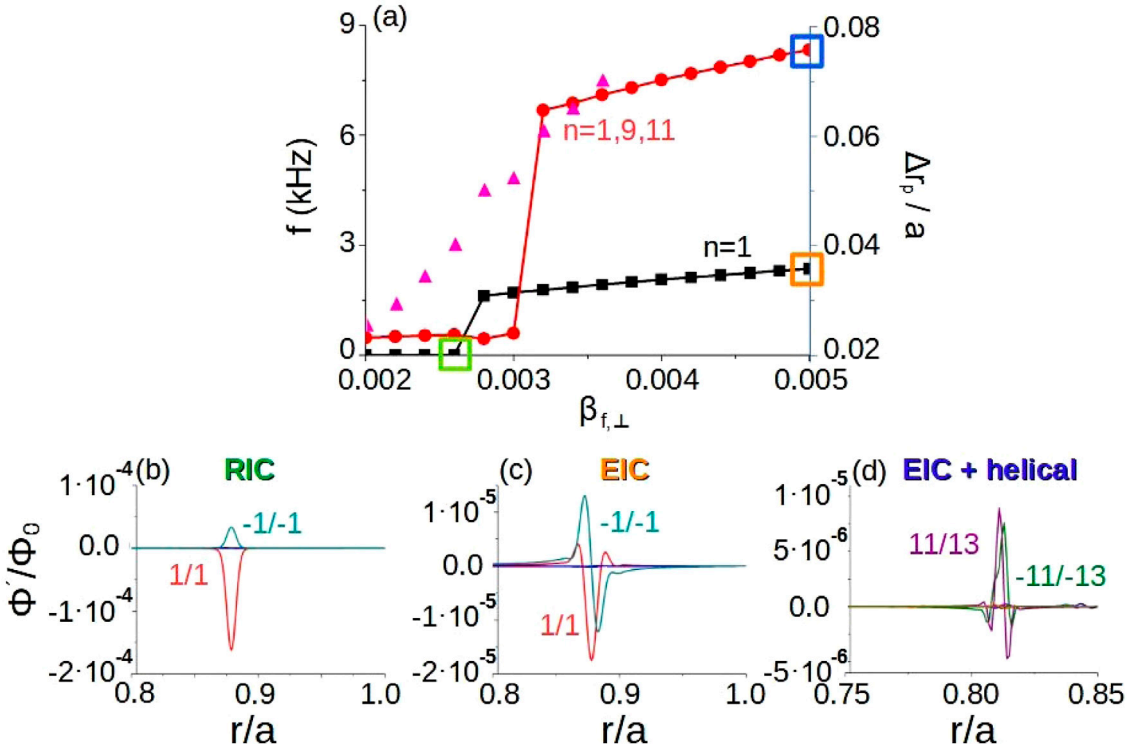

FIGURE 2
Analysis of the EIC stability in the LHD plasma. **(A)** Perturbation frequency for different values of the EP β linked to the perpendicular NBI injector ($\beta_{f,\perp}$) near the transition between RIC and EIC for the $n = 1$ toroidal family (black line) and helical family $n = 1, 9, 11$ (red line). The pink triangles show the instability eigen-function width (normalized to the minor radius). Eigenfunction of the $n = 1$ electrostatic potential perturbation if **(B)** $\beta_{f,\perp} = 0.0025$ and **(C)** $\beta_{f,\perp} = 0.005$. **(D)** Eigenfunction of the $n = 1, 9, 11$ electrostatic potential perturbation if $\beta_{f,\perp} = 0.005$. Reproduced courtesy of IAEA, IOPScience, Nuclear Fusion journal. Figure adapted from [131]. Copyright (2019) IAEA.

is unstable with the $n/m = 11/13$ mode dominating. The normalized width of the perturbed eigen-function (pink triangles) increases with $\beta_{f,\perp}$. Below the $\beta_{f,\perp}$ threshold to destabilize the 1/1 EIC the normalized eigen-function width of the 1/1 RIC is $r/a = 0.04$, similar to the instability width measured in the experiment during the phase I and early phase II (please see Figure 7 of [85]). Above the 1/1 EIC $\beta_{f,\perp}$ threshold the eigen-function width keeps increasing, up to $\Delta r_p/a = 0.07$ for $\beta_{f,\perp} = 0.0036$, consistent with the inward extension of the instability observed in the experiment during the late phase II and the transition to the phase III. In addition, the radial location of the EIC in the simulations, around $r/a = 0.88$, and the frequency range of the perturbation, $f = 4$ kHz for the 1/1 EIC and $f = 8.5$ kHz after the helical family $n = 1, 9, 11$ destabilization, is consistent with the EIC phases observed in the experiment.

4.2 Stellarator: TJ-II

TJ-II plasmas heated by "co-/counter-" injected NBI along/against the toroidal field show an increase/decrease of the rotational transform by the NBI driven currents. The NBIs destabilize multiple AEs in the range of 150–300 kHz, resulting in frequency sweeps that are connected to the evolution of the iota profile [138, 139]. The FAR3d code was used to analyze the AE destabilization by EPs in different TJ-II configurations, comparing simulation results and experimental observations, reproducing the AE frequency sweeping as the rotational transform profile is modified by the current induced by the NBI [152]. Figure 3, panels a, indicates that the dominant mode in the simulation changes as the iota profile is modified, showing an anti-correlation between the growth rate of different helical families. Panel b shows the sweeping of the mode frequency as the iota profile is displaced, similar to the experiment observations. Panels c to f indicate the radial displacement, frequency range variation and opening/closing of the Alfvén continuum gaps as the iota profile is displaced. The evolution of the gaps may explain the modification of the AE stability observed in the experiment. Panels g to i show the destabilization of 9/6, 11/7 and 13/8 dominant modes as the iota is displaced from $\Delta - \iota = -0.03$ to 0.08. It should be noted that the analysis reveals the essential role of the helical couplings in the analysis of the AE stability in TJ-II plasma, predicting the destabilization of helical AEs (HAE) by NBI EPs.

The combination of NBI heating with electron cyclotron heating (ECH) and electron cyclotron current drive (ECCD) in TJ-II plasma lead to a modification of the AE activity observed in the experiments [153]. Several TJ-II operational scenarios are explored using FAR3d to identify and characterize the unstable AEs for discharges combining NBI with ECH/ECCD injection. Figure 4, panels a to d, shows the AE activity measured in the discharge 44,257 heated only by the NBI. AEs are triggered in a rather narrow frequency range around 100 and 200 kHz as well as chirping AE activity

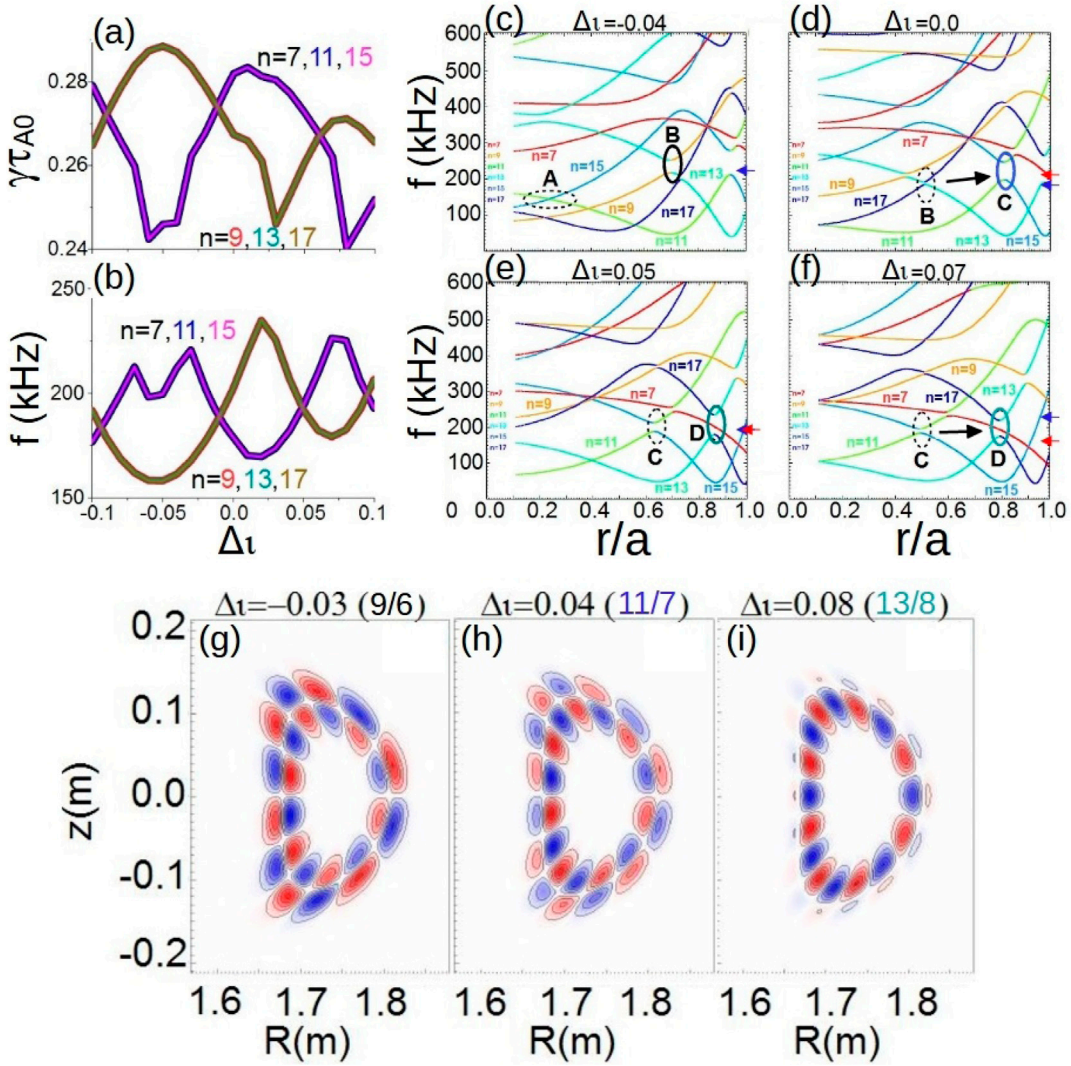

FIGURE 3
Analysis of HAE stability in the TJ-II plasma. **(A)** Growth rate and **(B)** frequency of the simulation dominant modes if the iota profile is displaced by $-\iota \pm \Delta - \iota \cdot i$ with $\Delta - \iota = 0.01$ and $i = [1,10]$. Alfvén gaps evolution for different iota profile displacements: **(C)** $\Delta - \iota = -0.04$, **(D)** 0.0, **(E)** 0.05 and **(F)** 0.07. The gaps where the dominant mode is triggered are highlighted by an oval solid line color coded by the mode number. The black arrow indicate a transition between different helical families. The color arrows at the right side of the panels indicate the frequency range of the mode identified in the simulations for each iota profile displacement and helical family (blue for $n = 7, 11, 15$ and red for $n = 9, 13, 17$ helical families). 2D plots of the electrostatic potential perturbation for different iota profile displacements **(G)** $\Delta - \iota = -0.03$, **(H)** 0.04 and **(I)** 0.08. Reproduced courtesy of IAEA, IOPScience, Nuclear Fusion journal. Figure adapted from [152]. Copyright (2017) IAEA.

between 160 and 210 kHz observed from $t = 1210$ ms. Panels e to j show the AEs calculated by FAR3d with respect to the Alfvén continuum gaps, indicating the destabilization of HAEs and EPM in a frequency range (Mirnov coil data) and radial location (HIBP diagnostic) consistent with the experimental observations (see Figures 19, 20, 22 of Ref. [153]). The analysis confirms the important effect of the neutral beam current drive (NBCD) and ECCD on the Alfvén continuum and AE stability. In addition, the application of ECCD is shown as an efficient actuator to control the AE stability in TJ-II plasma.

The effect of the iota profile evolution on the AE stability is further analyzed in TJ-II plasma by modifying the current flowing in the vertical field coils of the device, performing experiments that show oscillating patterns of the AE frequency [154]. FAR3d is used to reproduce the AE frequency sweeping as the current in the vertical field coils changes and modifys the iota profile. Figure 5, panel a, shows the sweeping of the measured AE frequency along the discharge as successive maxima and minima correlated with the up or down-shift of the iota profile. Panel b indicates the AE frequency sweeping calculated by FAR3d approximately reproduces the experimental observation. Panel c shows the $n/m = 8/5$ mode identified at the plasma periphery. Panels d to g indicate the evolution of the Alfvén continuum as the iota profile evolves, showing the 8/5 mode is nearby the radial location and frequency range of a continuum gap minimum at the plasma periphery, pointing out the mode can be classified as a GAE. The modeled plasma potential perturbations show reasonable similarities to the measurements by the dual HIBP (see

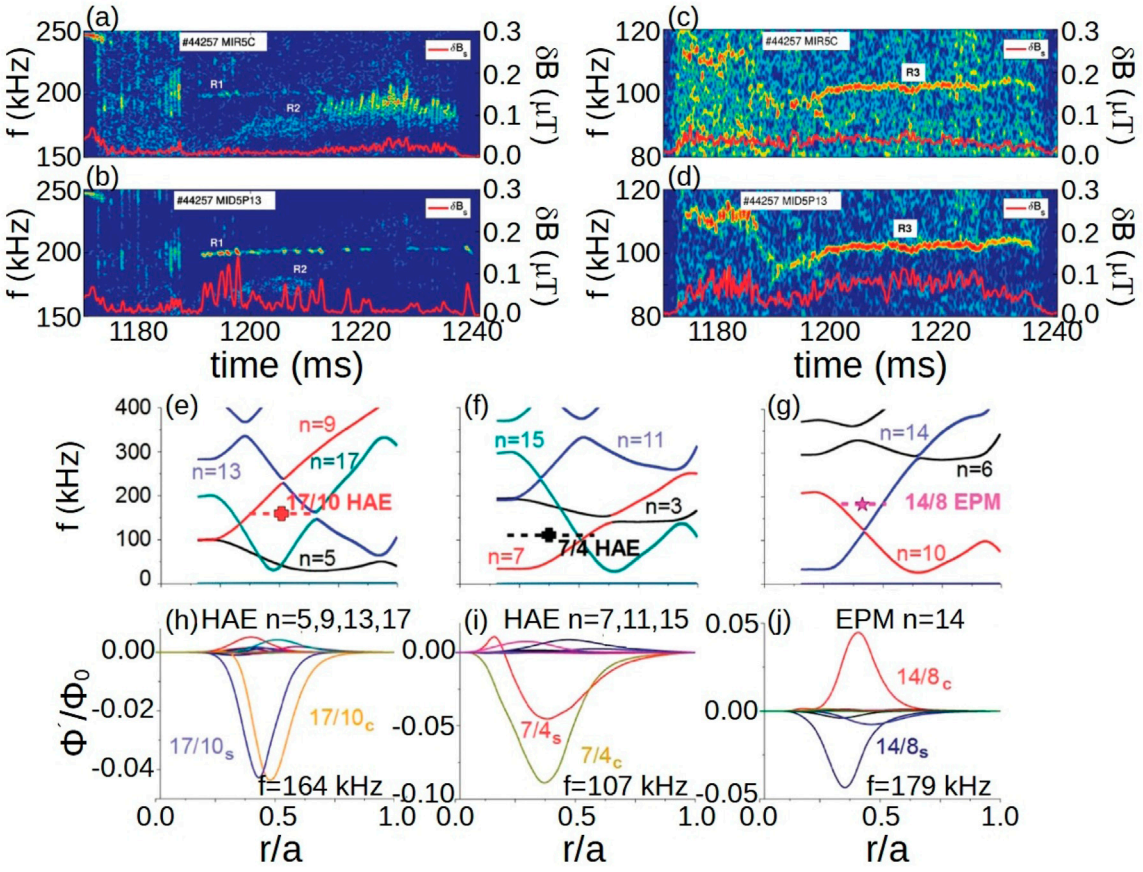

FIGURE 4
Analysis of AEs destabilized in NBI heated TJ-II plasma. Magnetic fluctuations spectrograms in the 150 – –250 kHz frequency range and mode amplitude $\delta B(t)$ measured by the magnetic coils **(A)** *MIR5C* and **(B)** *MID5P13*. Magnetic fluctuation spectrograms in the 80 – –120 kHz frequency range and mode amplitude $\delta B(t)$ measured by the magnetic coils **(C)** *MIR5C* and **(D)** *MID5P13*. Alfvén wave continua for the helical families **(E)** $n = 5, 9, 13, 17$, **(F)** $n = 7, 11, 15$ and **(G)** $n = 6, 10, 14$. Eigenfunctions of the electrostatic potential perturbation triggered by the helical families **(H)** $n = 5, 9, 13, 17$, **(I)** $n = 7, 11, 15$ and **(J)** $n = 6, 10, 14$. Reproduced courtesy of IAEA, IOPScience, Nuclear Fusion journal. Figure adapted from [153]. Copyright (2021) IAEA.

Figure 7 of Ref. [154]; Figure 21 of Ref. [155]); this is the only method allowing non-perturbative direct measurements of the electric potential in the hot plasma core [156–158].

4.3 Tokamak: DIII-D

The FAR3d code is also used for analyzing AE instabilities in tokamak devices. AE activity induced by strong NBI heating has been extensively studied in the DIII-D device, detecting a large variety of Alfvénic instabilities as GAE [159], TAE [160], RSAE [161], BAE [162], EAE [163] and NAE [32]. The NBI system in DIII-D can provide up to 20 MW of injection heating power with EPs in the energy range of 40–85 keV. AE instabilities caused by the NBIs reduce DIII-D performance, increasing the EP transport and enhancing energetic particle losses [164–166]. FAR3d was applied to study the AEs destabilized at the DIII-D pedestal during transient thermal β drops in high poloidal β discharges with internal transport barriers (ITBs), driven by $n = 1$ external kink modes [167]. The stability of AEs in this DIII-D configuration is an important topic because high poloidal β discharges are required for tokamak steady state operation [168–170], in order to achieve adquate bootstrap current and non inductive current drive [171, 172]. In particular, AE activity is enhanced after the onset of the external kink, inducing larger fast-ion transport losses and inhibiting or even preventing the recovery of the thermal β, resulting in a deterioration of the DIII-D performance. Two scenarios were observed after the collapse: discharges with bifurcation (two instability branches with different frequencies driven in the middle plasma and at the pedestal) and without bifurcation (single instability branch). The energetic particle losses driven by the destabilized AEs lead to a decrease of the expected neutron measurements up to a 50% in the bifurcation case and up to 60% in the non bifurcation case after the collapse of the thermal β [173]. FAR3d is applied to study the stability properties of AE and ballooning modes in both scenarios. Figure 6 compares the growth rate and frequency of the dominant modes in the simulations, panel a and b, with the instabilities measured in the discharge using the CO2 interferometer data, panel c. Before the collapse (A1) $n = 2$ to 6 AEs are unstable showing frequencies between 15 and 20 kHz for $n = 2$ to 4 AEs, 75 kHz for $n = 5$ AE and 90 for $n = 6$ AE. On the other hand, the dominant $n = 1$ perturbation is the external kink. During the collapse phase (A2), the dominant $n = 1$ perturbation is an AE with a frequency of

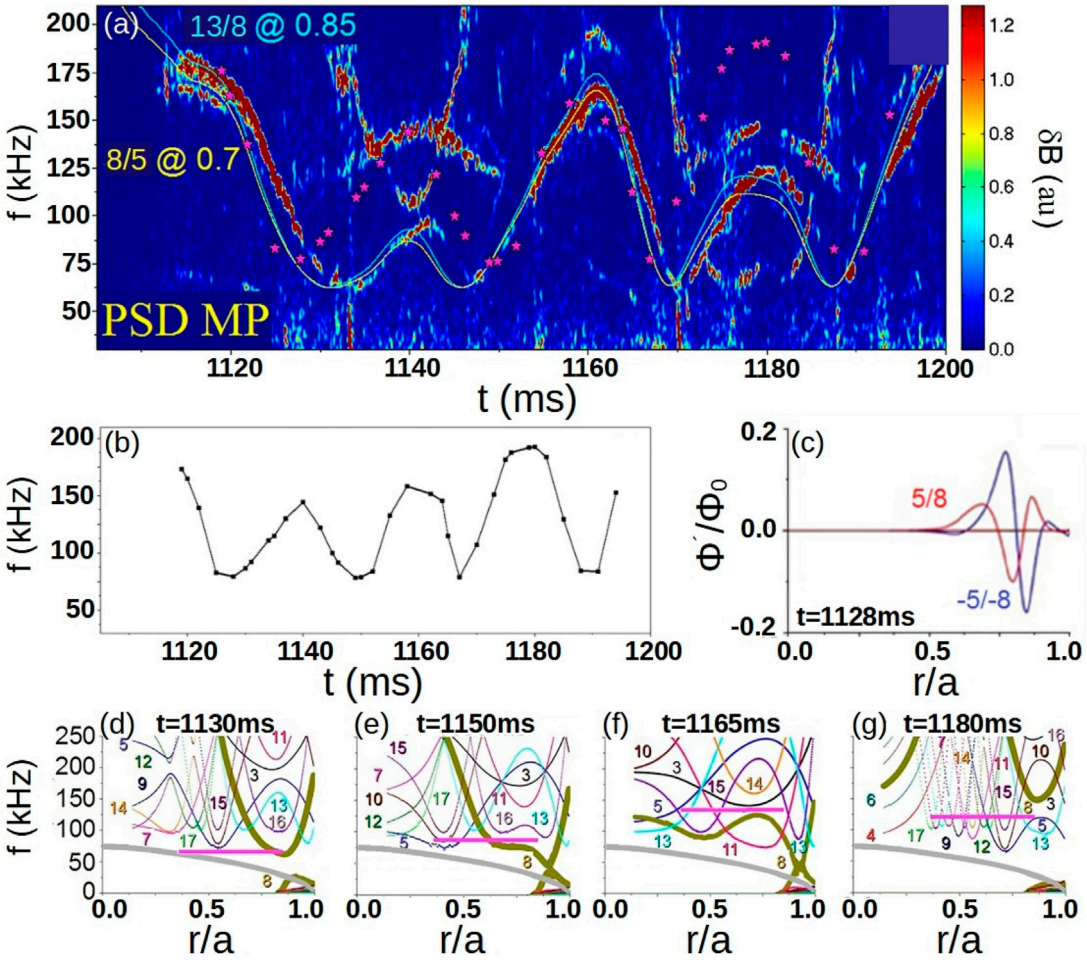

FIGURE 5
Analysis of AEs frequency sweeping in TJ-II plasma. **(A)** Power spectrogram of magnetic fluctuations measured by the Mirnov probes. The blue and yellow lines indicate the analytical prediction of n/m = 13/8 and 8/5 GAM frequency evolution (see Equations 1–3 of Ref. [154]). The pink stars show the frequency of the mode calculated by FAR3d. **(B)** Frequency of the 8/5 GAE calculated by FAR3d along the discharge. **(C)** Eigenfunction of the electrostatic potential perturbation of 8/5 GAE at t = 1128 ms. Alfvén gaps structure at **(D)** t = 1130, **(E)** t = 1150, **(F)** t = 1165 and **(G)** t = 1180 ms. The colored lines indicate the n = 3 to 17 toroidal mode numbers. The gray lines show the GAM frequency, the pink line the radial location and frequency range of the 8/5 GAE. Reproduced courtesy of AIP Publishing, Physics of Plasma journal. Figure adapted from [154]. Copyright (2019) AIP Publishing.

20 kHz. The other mode frequencies increase, particularly n = 4, reaching the same frequency range as the n = 5 and 6 AEs, around 125 kHz. After the collapse (A3), the AEs frequency further increases up to 125–225 kHz. On the other hand, if the simulations are limited to the plasma pedestal, the frequency of high n modes ranges from 25 to 40 kHz, consistent with the two instability branches observed in the bifurcation case. Consequently, the low frequency instability branch is linked to the destabilization of the pedestal region, while the high frequency instability branch is linked to AEs destabilized between the middle plasma and the pedestal. Panels d and e show the eigenfunction of the TAEs triggered in the middle-outer plasma region and the ballooning modes nearby the plasma periphery. Consequently, the analysis may indicate the bifurcation case is driven if the plasma pedestal ($r/a > 0.9$) is decoupled from the rest of the plasma, due to the large thermal ion density and temperature gradient near the periphery, as well as a local maximum of the plasma toroidal rotation near the pedestal.

AE destabilization in advanced DIII-D high poloidal β discharges causes a deterioration of the device performance due to the strong NBI injection [174]. This configuration was tested as a candidate for the steady state operational scenarios in ITER [175] and CFETR [176, 177]. In particular, the regimes that were explored show an improved energy confinement due to the generation of a robust internal transport barrier and a wide region with negative magnetic shear. FAR3d has been applied to calculate the AE activity in the reference shot 173,880 [178]. Figure 7, panel a, indicates the destabilization of several AEs at various frequency ranges between 60 and 200 kHz. Panel b shows several gaps in the Alfvén continuum for n = 1 to 6 toroidal mode families, particularly wide TAE and EAE gaps covering the main part of the plasma radius. Panel c indicates the destabilization of different AE families including the BAE, TAE, EAE and NAE. Introducing FLR effects in the simulations results in a strong stabilizing effect on high frequency AEs, such as the EAE and NAE modes. The eigenfuction of the fastest growing AEs in the simulation are shown in the panels d to h; these are generally localized in the inner plasma region.

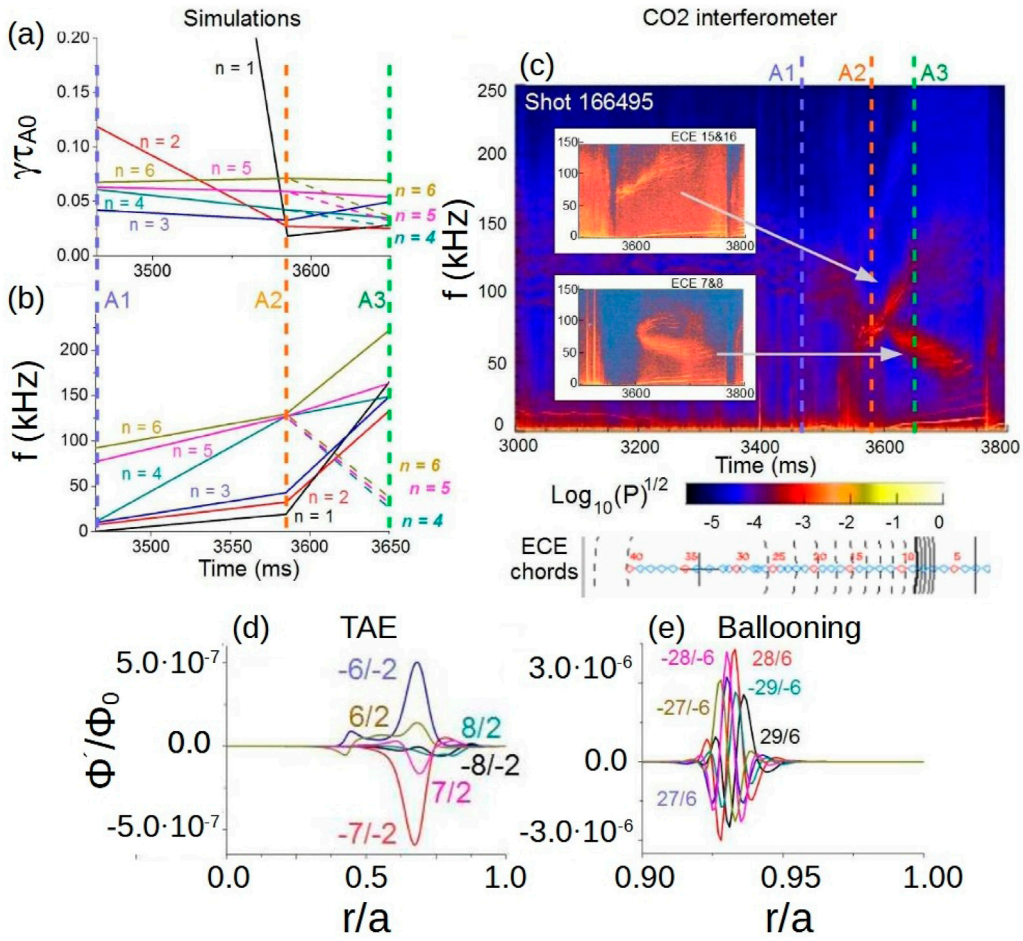

FIGURE 6
Analysis of the AEs destabilized in DIII-D high poloidal β discharges. Instability growth rates **(A)** and frequencies **(B)** in the bifurcation case at different discharge phases: before the collapse (A1), during the collapse (A2) and after the collapse (A3). The solid lines indicate the simulations that include all the modes and the dashed lines the simulations limited to the pedestal. The solid italic symbols indicate the mode number of the simulations limited to the pedestal. Panel **(C)** shows the CO2 interferometer data (sub-panels indicate the ECE data at different chords and the gray arrows the instability analyzed). Eigenfucntions of the electrostatic potential perturbation of **(D)** $n = 2$ TAE and **(E)** $n = 6$ ballooning mode. Reproduced courtesy of IAEA, IOPScience, Nuclear Fusion journal. Figure adapted from [138]. Copyright (2018) IAEA.

4.4 Tokamak: EAST

Another example dedicated to tokamaks is the study of the AE activity in the Experimental Advanced Superconducting tokamak (EAST) discharges with high thermal β and low toroidal magnetic field; this operational scenario is intended to explore the ITER baseline scenario [180]. EAST plasmas are heated by two NBIs providing 4 MW power with a voltage about 80 kV [181] leading to the destabilization of AE activity only in particular operational scenarios [182, 183]. In particular, FAR3d is used to study the AE activity observed after an accidental plasma contamination with Tungsten [184, 185]. Figure 8 shows the destabilization of AEs after the Tungsten contamination around $t = 6$ seconds in the magnetic and ECE data, panels a and c. The strongest AE activity is divided in two branches. The first branch has almost constant frequency around 90 kHz and there is a second branch showing a frequency up-shift from 60 kHz to 90 kHz. In addition, there is another instability around 60 kHz. The analysis of the magnetic perturbation shows the AE activity is mainly linked to an $n = 2$ perturbation [186] (see panel b). The modes with the largest growth rate calculated by FAR3d are the $n = 2$ and 3 modes in the frequency range of 55 and 85 kHz, panel d. Panels e to h indicate the perturbations include an $m/n = 3/2 - 4/2$ TAE, a 4/2 EPM and a mix between a 6/3 EPM and a 6/3 − 7/3 TAE. Consequently, the frequency range, radial location and mode numbers of the identified $n = 2$ perturbation are consistent with the observations.

FAR3d has also participated in other research efforts dedicated to identify AE activity in the LHD [92, 187], TJ-II [188, 189], JET [190], EAST [191] and Heliotron J [192] plasmas; the simulations show a reasonable agreement with the experimental data. Once the AE activity is validated with the code, optimization studies can be performed to identify operational scenarios resulting in reduced AE activity which may lead to reduced EP transport and improved plasma heating performance. Such analysis is the topic of the next section.

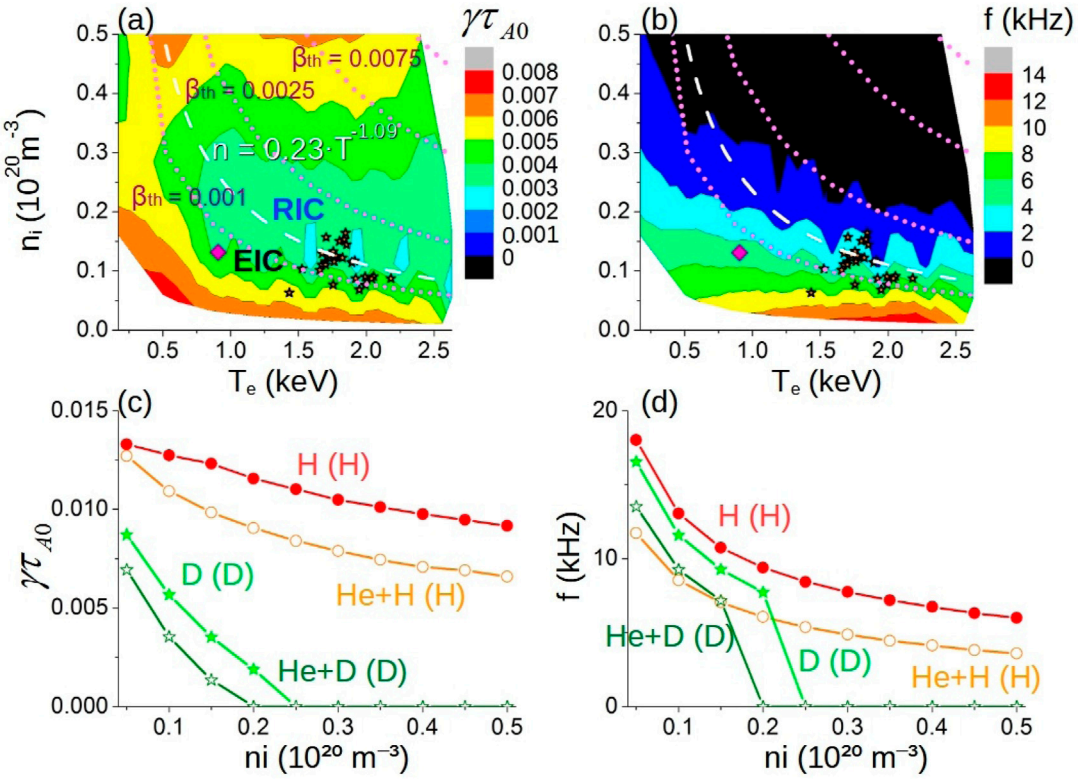

FIGURE 7
Analysis of EIC stability trends in LHD plasma. **(A)** Growth rate and **(B)** frequency of the instabilities in simulations with different values of the thermal plasma ion density and electron temperature at the $-\iota = 1$ rational surface. The dashed purple lines indicate the iso-lines of the simulations with the same thermal β. The dashed white line shows the transition between scenarios with dominant 1/1 EIC and RIC fitted by the non-linear curve $n = aT^b$. The stars show the EIC destabilized in LHD discharges with respect to the thermal plasma density and temperature at the $-\iota = 1$ rational surface. The pink diamonds indicate the reference case. **(C)** Growth rate and **(D)** frequency of the 1/1 EIC for different thermal plasma densities (β_t = 0.01) in Hydrogen plasma with Hydrogen NBI (red line and dots), Helium + Hydrogen plasma with Hydrogen NBI (orange line and circles), Deuterium plasma with Deuterium NBI (green line and stars) and Deuterium + Helium plasma with Deuterium NBI (dark green line and stars). Reproduced courtesy of IAEA, IOPScience, Nuclear Fusion journal. Figure adapted from [179]. Copyright (2020) IAEA.

5 Optimization studies

There are different techniques to reduce the AE/EPM activity in fusion devices, for example, modifying the properties of the thermal plasma and magnetic field configuration, applying external actuators (NBI, ECH, ECCD) or the interaction between different EP species present in the plasma [193]. This section is dedicated to a discussion of the application of FAR3d to explore different optimization strategies.

5.1 Effect of the thermal plasma

Modifying the thermal plasma properties can influence AE stability through various channels. A change of the thermal plasma density and temperature modifies the EP resonance energy (through changes in the Alfvén velocity), EP slowing down time, plasma resistivity as well as continuum, FLR and electron-ion Landau damping effects. Consequently, an optimized selection of the thermal plasma properties may lead to configurations with reduced AE activity. It must be recalled the EP resonance associated with EPM destabilization is not affected by a modification of the thermal plasma density/temperature; however, the Alfvén gap structure, FLR and electron-ion Landau damping effects will change. For this reason the EPM growth rate and frequency can also depend on thermal plasma properties.

In the LHD stellarator, several stabilization strategies to mitigate the 1/1 EIC have been identified experimentally, for example, increasing the thermal plasma temperature above a given threshold through the application of ECH at the plasma periphery [86] or the modification of the magnetic field topology using resonant magnetic perturbations (RMP) [194]. An analysis of the 1/1 EIC stability in different LHD operational scenarios was performed using the FAR3d code [179], identifying optimization trends with respect to the thermal plasma parameters, the operational regime of the tangential and perpendicular NBIs as well as the magnetic field topology and strength. Figure 9, panels a and b, indicate regimes where the 1/1 EIC is stable if the thermal β is $\geq 0.25\%$ for a Hydrogen plasma (dotted purple lines). The EIC is unstable up to a thermal plasma β of almost 0.2% if the thermal ion density is $\leq 0.15 \cdot 10^{20}$ m^{-3} and the electron temperature is ≥ 1.5 keV. The EIC is also unstable if the thermal ion density is $\leq 0.25 \cdot 10^{20}$ m^{-3} and if the electron temperature is ≤ 0.5 keV. The dashed white line indicates the transition between unstable 1/1 EIC and unstable RIC, calculated by fitting the simulation data of the parametric studies with respect to the thermal ion density/electron

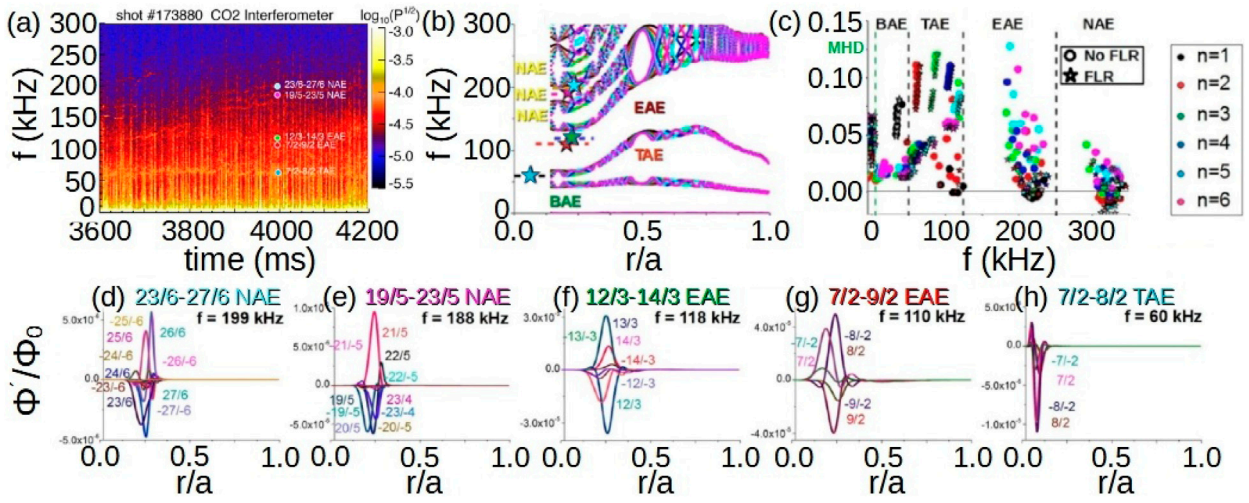

FIGURE 8
Analysis of the AE stability in DIII-D high poloidal β discharges with an internal transport barrier. **(A)** Cross-power density fluctuation spectra from CO2 interferometer. **(B)** Alfvén gaps and **(C)** growth rate/frequency of the AEs calculated in the simulation with (circle) and without (star) FLR effects. Eigenfunction of the electrostatic potential perturbation of the **(D)** $n = 6$ NAE, **(E)** $n = 5$ NAEs, **(F)** $n = 3$ EAE, **(G)** $n = 2$ EAE, and **(H)** $n = 2$ TAE. The radial location and frequency range of the dominant modes identified in the simulations are included in the Alfvén gaps. Reproduced courtesy of IAEA, IOPScience, Nuclear Fusion journal. Figure adapted from [178]. Copyright (2020) IAEA.

temperature using the non-linear curve $n = aT^b$. The stars indicate the parametric range where the 1/1 EIC are destabilized in LHD discharges, showing a reasonable agreement with the 1/1 EIC threshold predicted by the simulations. Panels c and d indicate the thermal ion density threshold to stabilize 1/1 EIC in a deuterium plasma is $n_i = 0.25 \cdot 10^{20}$ m^{-3}, smaller compared to density required for hydrogen plasma, $n_i = 0.5 \cdot 10^{20}$ m^{-3}. In addition, if a Hydrogen or Deuterium plasma is mixed with Helium, 1/1 EIC growth rate is smaller for all the thermal ion densities tested and the stabilization threshold decreases, $n_i = 0.2 \cdot 10^{20}$ m^{-3} for a Deuterium + Helium plasma. Also, 1/1 EIC frequency decreases in a Deuterium plasma compared with a Hydrogen plasma, just as for a Hydrogen or Deuterium plasma mixed with Helium, a reasonable result because the EP poloidal bounce/transit frequency and Alfvén velocity scale as $(Nm_i)^{-1/2}$, with N the ion atomic mass and m_i the ion mass. This results are consistent with the experimental observations.

5.2 Effect of the magnetic field configuration

The analysis of the plasma and EP stability for stellarator fusion devices with different magnetic field configurations (i.e., types of quasi-symmetry) is essential for the design and optimization of future stellarator reactors. Examples of devices taking advantage of quasi-symmetries are the Chinese First Quasi-Axisymmetric stellarator (CFQS) [195–197] and National Compact stellarator Experiment (NCSX) [198], the Quasi Poloidal stellarator (QPS) [199] and the Helically Symmetric Experiment (HSX) [200]. In addition, there are generalized symmetries such as omnigenity where the mean radial collisionless guiding center magnetic drift is minimized, leading to good collisionless orbit confinement [201]. The optimization of the AE stability in these configurations is important in order to attain efficient plasma heating, reduce operational power requirements and improve the economic viability of reactor devices.

The CFQS plasma will be heated by a tangential neutral beam injector (NBI) with an injection energy of 30 keV and a power of 0.9 MW that may lead to the destabilization of AEs [202]. FAR3d was applied to study the AE destabilization threshold of $n = 1$ to 4 toroidal mode families triggered by EPs with energies between 10 and 30 keV [203]. In addition, the effect of the NBI deposition region, finite thermal β, helical couplings, Finite Larmor Radius (FLR) and electron-ion Landau damping on the AE stability was analyzed. Figure 10, panel a, shows an example of the CFQS Alfvén continuum gaps if the thermal β is 0.01, indicating a TAE gap in the frequency range of 160–210 kHz that covers the entire plasma radius. Panel b shows an unstable $1/2 - 1/3$ TAE with $f = 208$ kHz triggered in the inner plasma region if $\beta_f = 0.005$ and EP energy is 17 keV. The analysis concludes that the heating efficiency of a CFQS plasma heated by tangential NBI can decrease due to the destabilization of $n = 1$ to 4 BAE/TAEs and $n = 2, 4$ HAEs above a given injection intensity threshold, particularly if the thermal β of the discharge is low.

Another example is the QPS design that combines quasipoloidal symmetry and low aspect ratio [204, 205] to achieve particle and energy confinement at high β, second ballooning stability [206], low damping of poloidal flows [207] and potential stabilization of drift/trapped particle instabilities [208]. The AE stability of QPS plasma heated by a NBI identical to LHD device is analyzed for QPS configurations with different number of magnetic field periods for vacuum and finite thermal β cases [209]. Figure 11 shows an example of the AE stability in the configuration with two magnetic field periods and finite thermal β. Panel a indicates a wide EAE gap covering all the plasma radius although the TAE gap is only observed between the middle-outer plasma region. The narrow width of the TAE gap is caused by the near quasi-poloidal symmetry of this device; i.e., the TAE gaps are produced by the

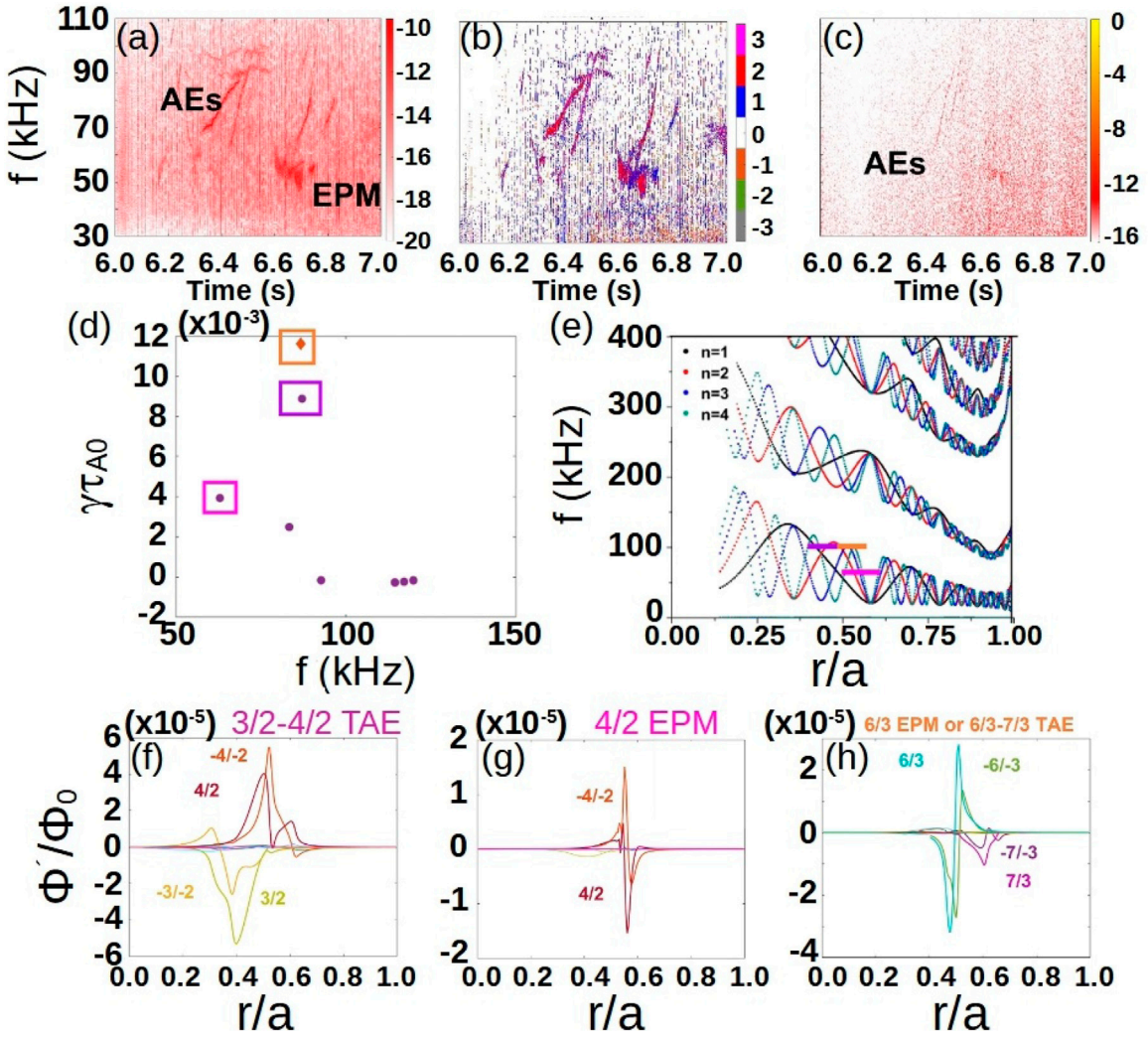

FIGURE 9
Analysis of AE/EPM destabilization in EAST after Tungsten plasma contamination. **(A)** Magnetic perturbations measured by Mirnov coils, **(B)** toroidal mode number of the instability and **(C)** ECE diagnostic data at r/a = 0.46. **(D)** Growth rate and frequency of the n = 2 dominant mode (purple box), n = 2 sub-dominant mode with the largest growth rate (pink box) and n = 3 dominant mode (orange box). **(E)** Continuum gaps including the radial location and frequency range of the modes highlighted in panel **(D)**. Black line for n = 1, red for n = 2, blue for n = 3 and cyan for n = 4 toroidal mode family. Eigenfuntions of the electrostatic potential perturbation of **(F)** dominant n = 2 mode, **(G)** sub-dominant n = 2 mode and **(H)** n = 3 dominant mode. Reproduced courtesy of IAEA, IOPScience, Nuclear Fusion journal. Figure adapted from [185]. Copyright (2024) IAEA.

poloidal variation of the magnetic field strength, and this variation is minimized in the QPS configuration. Panels b and c indicate the β_f threshold of n = 1 AE is 0.01, n = 2 and 3 AE is 0.015 and larger than 0.2 for n = 4 and 5 AEs. Panels d to f show some example of AEs destabilized in the middle-outer plasma region, identified as a 1/3 – 1/5 EAE with 245 kHz, 1/3 – 3/9 HAE with 98 kHz and 2/6 – 2/7 TAE with 113 kHz. The analysis also indicates the AE stability improves in the configuration with three magnetic field periods, showing a growth rate five times smaller compared with the two field period configuration. In addition, the finite β case shows a higher β_f threshold compared to the vacuum case.

Advanced tokamak operation scenarios can be attained by modifying the magnetic field configuration, for example generating wide reverse magnetic shear regions in the plasma [210, 211]. Nevertheless, AE stability in such configurations could be unfavorable for an efficient plasma heating. Reverse magnetic shear discharges are extensively studied in the DIII-D device [212–214] showing a large fraction of bootstrap current [215, 216] and improved MHD stability [217–219]. These configurations have been selected as a base line scenario for ITER and DEMO [220–222], although an enhancement of the energetic particle transport by unstable AEs was measured [42, 165, 223]. FAR3d is used to explore optimization pathways to improve thermal plasma and AE linear stability of DIII-D reverse magnetic shear discharges [224]. It has identified configurations that minimize the growth rate of AE/thermal plasma instabilities for DIII-D discharges with different magnetic configurations and NBI operation regimes. This approach can be useful for optimizing device performance. Figure 12, panel a, indicate AE activity throughout the discharge measured by CO2 interferometry: burst activity at M10, constant frequency AE at M1A, up-sweeping frequency AE at M1B and weaker steady frequency AEs at M1C. In addition, magnetic

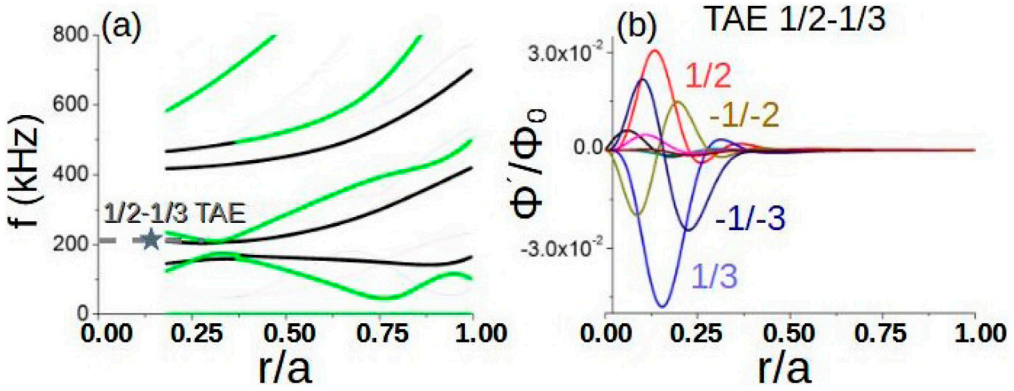

FIGURE 10
Analysis of the AE stability of CFQS plasma. **(A)** Alfvén continuum for the CFQS configurations if the thermal β is 0.01. **(B)** Eigenfunction of the electrostatic potential perturbation for the 1/2 – 1/3 TAE destabilized if EP β = 0.005 and T_f = 17 keV. Reproduced courtesy of IAEA, IOPScience, Nuclear Fusion journal. Figure adapted from [203]. Copyright (2021) IAEA.

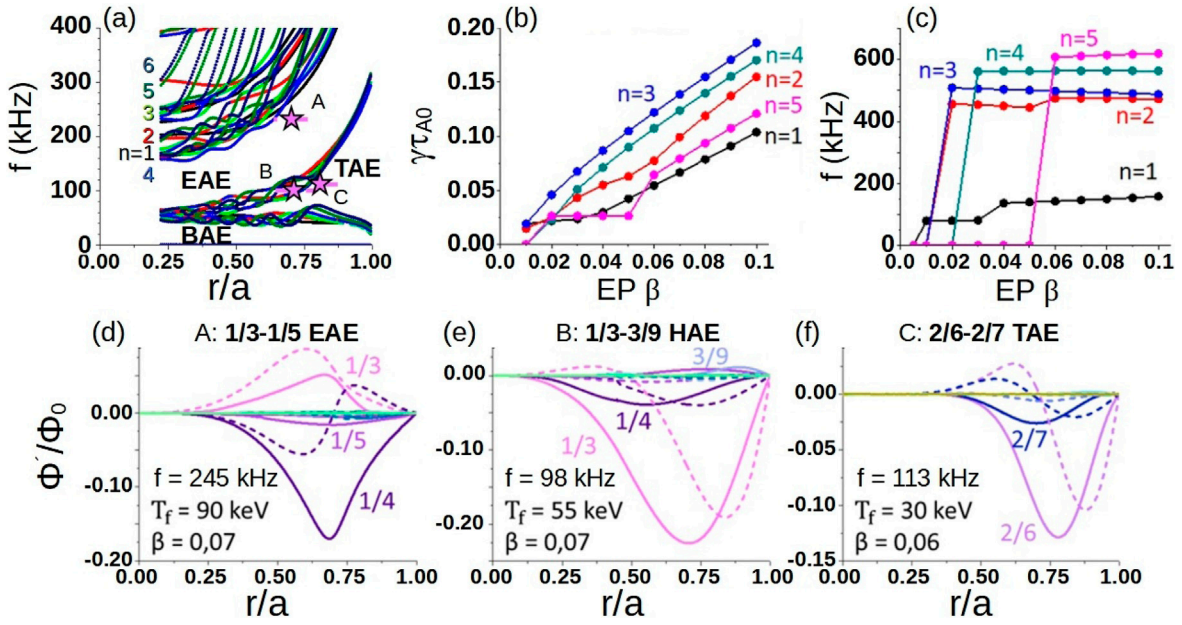

FIGURE 11
Analysis of the AE stability in QPS plasma. **(A)** Alfvén continuum of the configuration with two magnetic field periods and finite thermal β case for n = 1 to 6 toroidal families. The horizontal dashed lines indicate the radial location and frequency range of the AEs triggered by n = 1, 3, 5 and n = 2, 4, 6 helical families, the pink star represents the radial location of the AE amplitude maximum. **(B)** Growth rate and **(C)** frequency of the AEs triggered by the n = 1 to 5 toroidal mode families for different β_f values fixed the EP energy to 90 keV. Eigenfunction of the electrostatic perturbation of **(D)** 1/3 – 1/5 EAE, **(E)** 1/3 – 3/9 HAE and **(F)** 2/6 – 2/7 TAE. Reproduced courtesy of IAEA, IOPScience, Nuclear Fusion journal. Figure adapted from [209]. Copyright (2023) IAEA.

diagnostic data in panel b shows $n = 1$ to 4 low frequency instabilities in the range of 5–40 kHz. Panels c to f indicate the unstable MHD modes and AEs (BAE, TAE, EAE and RSAE) calculated by FAR3d in the different discharge phases analyzed, consistent with the frequency range, radial location and dominant modes measured in the experiment. Panels g and h show the eigenfunction of the 13/5 – 14/5 TAE unstable in the M10 phase and the 12/6 RSAE destabilized during M1B phase, respectively, both located in the inner-middle plasma region.

Another example of optimization in tokamak devices are operational scenarios using negative triangularity plasma shaping (NT). NT configurations can reach a rather large thermal β and improved energy confinement compared with positive triangularity (PT) configurations. NT configurations have been explored in the TCV device indicating a reduction of turbulence and transport [225, 226] as well as in the DIII-D device; DIII-D reached a reactor relevant thermal β and a confinement level similar to the H-mode in an L-mode plasma [227, 228]. Experiments in DIII-D were

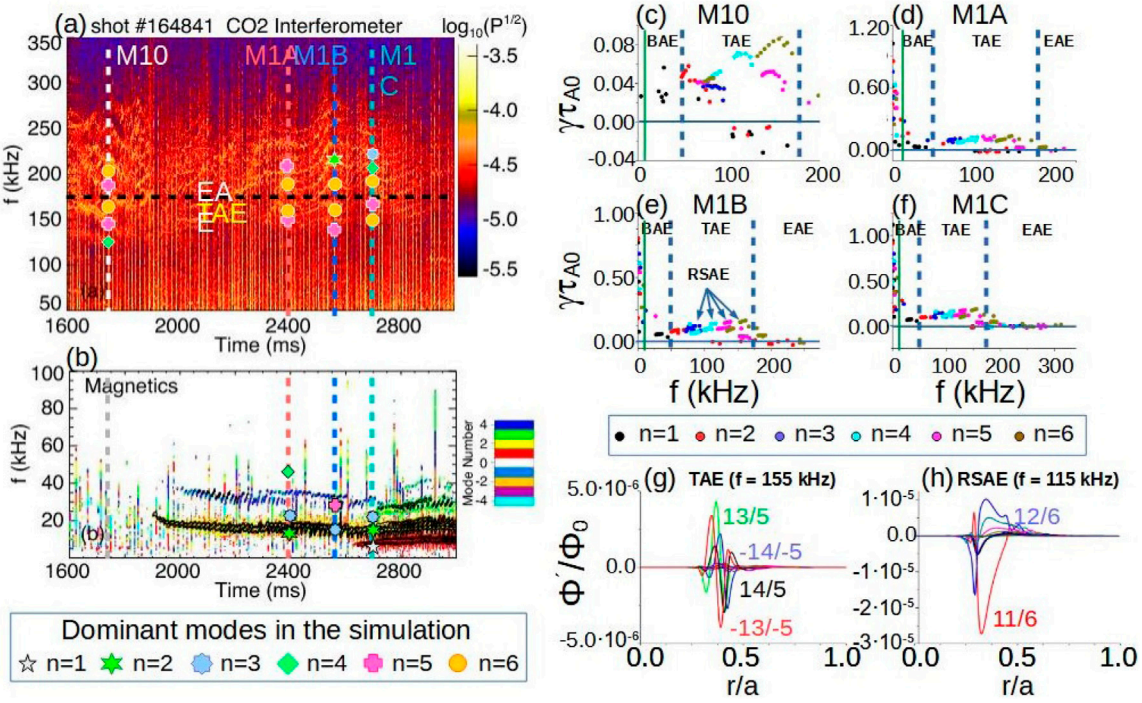

FIGURE 12
Stability of AEs in DIII-D reverse shear configurations. Instabilities measured along the shot 164,841 by **(A)** CO2 interferometer and **(B)** Mirnov coils: M10 (t = 1740 ms, white dotted line), M1A (t = 2400 ms, red dotted line), M1B (t = 1560 ms, blue dotted line) and M1C (t = 2700 ms, cyan dotted line). The colored stars indicate the dominant modes calculated in FAR3d simulations. The black dashed line indicates the transition between TAE and EAE families. Growth rate and frequency of the dominant and subdominant modes (n = 1 to 6) at **(C)** M10, **(D)** M1A, **(E)** M1B and **(F)** M1C discharge phases. The modes below the solid black line are stable damped modes. The solid green line separates MHD-like modes and Alfvén Eigenmodes. The dashed black lines separate different AE families (TAE/EAE/NAE). Eigenfunctions of the electrostatic potential perturbation of **(G)** n = 5 TAE and **(H)** n = 6 RSAE. Reproduced courtesy of IAEA, IOPScience, Nuclear Fusion journal. Figure adapted from [224]. Copyright (2019) IAEA.

performed to analyze the reduction of the microturbulence in NT shaped plasma resulting in a lower level of EP transport [229]. FAR3d is applied to study the AE stability in reference discharges with negative and positive triangularity [230]. Figure 13, panel a and b, indicate several AEs triggered in PT and NT discharges, respectively. The Alfvén continuum for the NT configuration, panels e and f, show a frequency up-shift around 10–20 kHz and wider gaps in the inner plasma compared to PT configurations, panels c and d. Panels g and h indicate the destabilization of n = 1 to 6 TAEs in the frequency range of 40–110 kHz for the PT case. n = 1 to 6 TAEs are also observed in the NT case at the same frequency range, although the growth rate is almost half compared to the PT, indicating the NT configuration is less unstable with respect to the AEs. The analysis also indicate TAEs in the NT case are destabilized radially outwards compared to the PT case, in a plasma region with lower EP density, possibly leading to better EP confinement and plasma heating efficiency.

5.3 Effect of external actuators

Neutral beam injectors or RF wave launchers required to heat the plasma can cause the destabilization of AEs. Nevertheless, the operational regime of any external actuators can be adapted to minimize such destabilizing effects. For example, AEs can be stabilized by modifying the actuator injected power to keep EP populations in the plasma below the AE destabilization threshold. Other options are weakening the EP resonance by modifying the EP energy or optimizing the NBI deposition to reduce the EP density gradients. In addition, the generation of non inductive currents can reduce the AE activity by locally modifying the magnetic field helicity, e.g., by increasing the magnetic shear and closing/narrowing the continuum gaps. Such mechanisms can be active with NBCD and ECCD. Additionally, actuators as ECW can locally modify the thermal plasma profiles leading to a reduction of the AE activity.

A set of experiments were performed in DIII-D investigating the NBI destabilizing effect by keeping the injected power fixed while changing the NBI voltage and current. This is equivalent to varying the EP energy and density, respectively [231–233]. This method provides a path to modify the EP distribution and reduce AE activity without requiring a change in the NBI injection geometry. FAR3d is used to calculate the AE stability as a function of the NBI voltage by analyzing the destabilizing effect of EP populations with different energies [87]. Figure 14, panels a and b, indicate a larger AE activity in the discharge 169,129 compared to the discharge 169,128 for the same total beam power. The NBI voltage increases in the discharge 169,128 from 60 to 80 keV although decreases in the discharge 169,129 from 80 to 60 keV. That implies that the higher NBI energy at the beginning of the discharge 169,129 causes a stronger EP resonance and larger AE activity. Panels c and d indicate n = 3 and 4 AEs are stable (black circles) below a given EP energy although

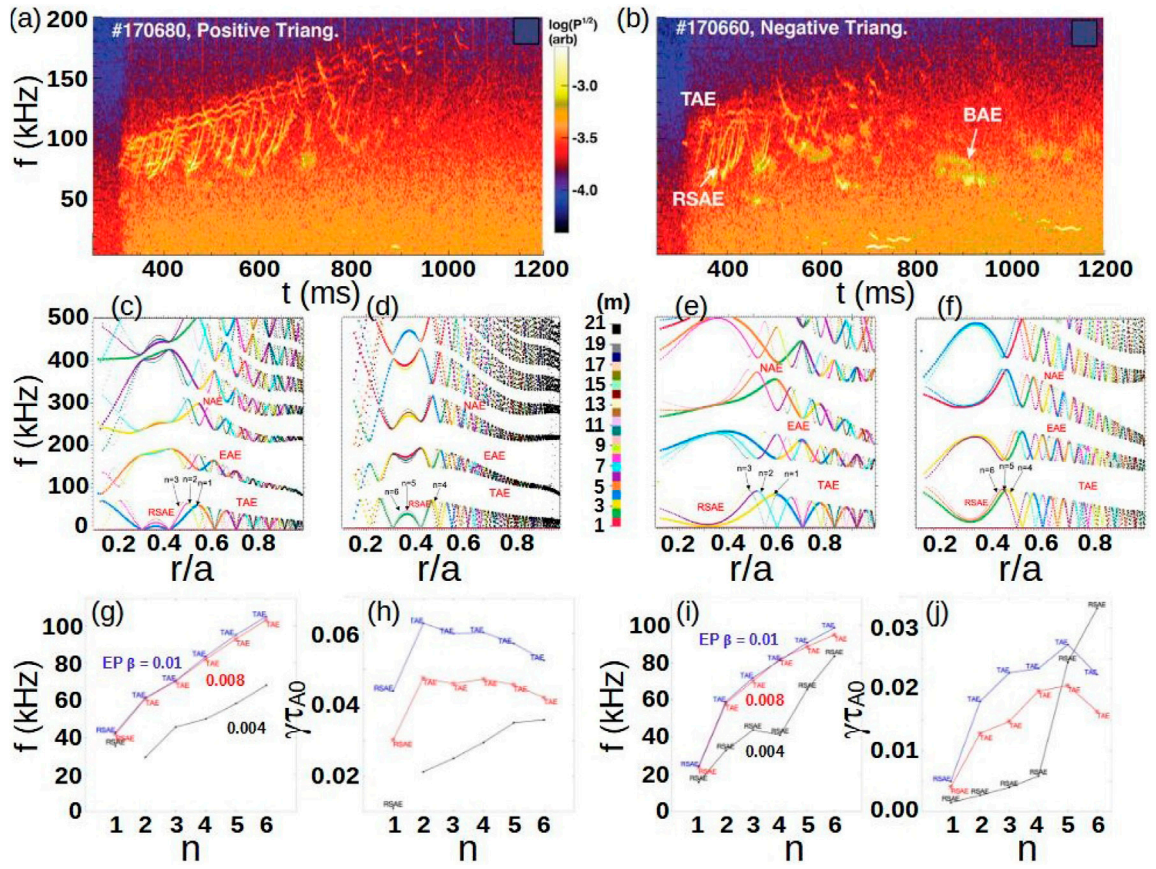

FIGURE 13
Stability of AEs in DIII-D negative triangularity discharges. ECE spectrogram of DIII-D **(A)** PT discharge 170,660 and **(B)** NT discharge 170,680. Alfvén continuum plots of PT discharge (no sound wave coupling) for **(C)** n = 1, 2, 3 and **(D)** n = 4, 5, 6 and NT discharge for **(E)** n = 1, 2, 3 and **(F)** n = 4, 5, 6. Legend indicates color coding corresponding to different poloidal mode numbers m in the Alfvén continuum. **(G)** Frequency and **(H)** growth rate of the n = 1 to 6 AEs calculated by FAR3d in the PT case for different EP β values. **(I)** Frequency and **(J)** growth rate of the n = 1 to 6 AEs calculated by FAR3d in the NT case for different EP β values. Black line for EP β = 0.004, red line for 0.008 and blue line for 0.01. The AE family destabilized is indicated in the figure. Reproduced courtesy of IAEA, IOPScience, Nuclear Fusion journal. Figure adapted from [230]. Copyright (2021) IAEA.

destabilized (red circles) above a given threshold. It should be noted that the EP energy is expressed in the graph with respect to the EP velocity, proportional to the square root of the EP energy. Thus, the simulations show the same trends compared to the experiments. Panels e and f indicate the AE perturbation is wider as the EP energy increases. Consequently, it is possible to improve the plasma heating by optimizing the operational regime of the NBI.

Non inductive current drive generated by ECCD and NBCD locally modifies the magnetic field configuration, affecting the stability of pressure gradient and current driven modes [72–75, 234] as well as AEs [63, 64]. There are several examples of ECCD injection in stellarators [69, 70, 235, 236] leading to an improved stability of pressure gradient driven modes and AE [78, 79, 237, 238]. In particular, the effect of the ECCD and the NBCD was analyzed in LHD and Heliotron J plasmas [239, 240] which attained a stabilization of TAE, GAE and EPM [71] as well as pressure gradient driven modes [241, 242]. The FAR3d code was used to study the stability of pressure gradient driven modes and AEs in LHD configurations for different locations of the vacuum magnetic axis (R_{ax}) with respect to the net plasma current generated by the tangential NBIs [243] as well as the deposition region of the NBI.

Figure 15, panels a to c, show a rather large variation of the toroidal current and AE activity along the discharge 147,288 caused by an non-balanced NBI injection. Two discharge phases with dominant counter-NBCD and co-NBCD are observed due to the injection of beams oriented in opposite directions. There is an increase of the frequency range of the AE families and a weaker magnetic probe signal during the co-NBCD phase with respect to the ctr-NBCD phase as well as the further destabilization of low (high) frequency AEs during the co-(ctr-) NBCD phase. During the ctr-NBCD phase, panels d, n/m = 1/2 mode with f < 80 kHz, 2/3 with f = 100 kHz, 3/4 with f = 140 kHz and 1/3 with f = 300 kHz are destabilized. In the co-NBCD phase, panel e, n/m = 1/2 mode with f = 30 − 90 kHz as well as 2/3 and 3/5 with f > 100 kHz are unstable. Panels f and g show the variation of the continuum gap structure as the NBCD increases for an inward shifted configuration with R_{ax} = 3.6 m and thermal β similar to 147,288 discharge, leading to an up-shift of the Alfvén gaps frequency range and wider TAE/EAE gaps between the magnetic axis and the middle plasma region, explaining the variation of the AE activity along the discharge. Panel h shows the growth rate and frequency of the modes calculated by FAR3d if I_p = 0 kA/T, identifying unstable n = 1 modes with

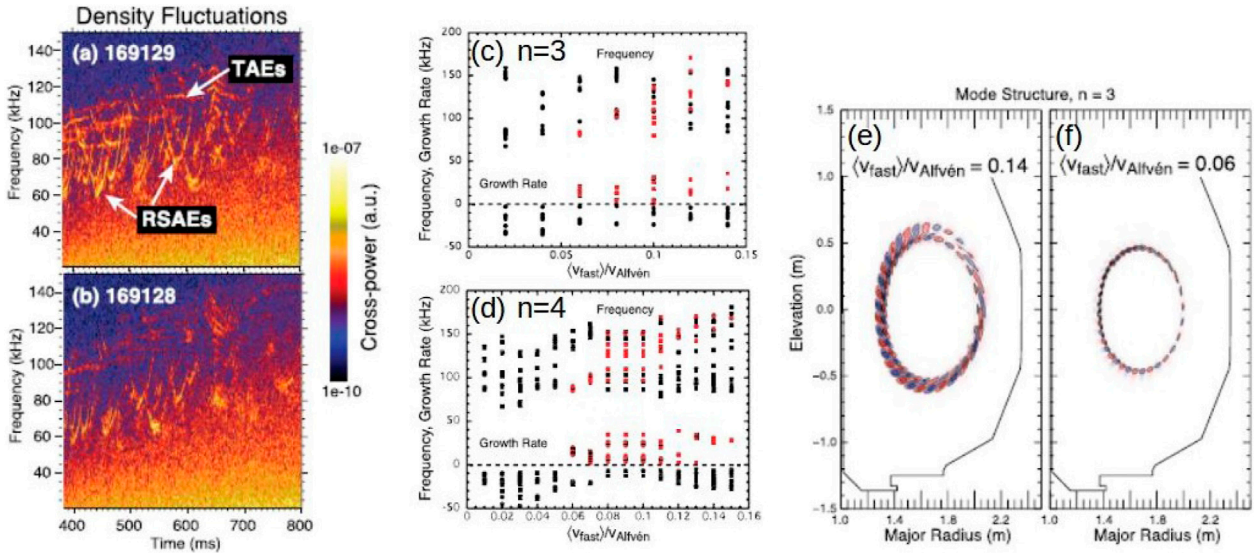

FIGURE 14
Stability of AEs in DIII-D plasma with respect to the NBI voltage and current. Cross-power of density fluctuations from two interferometer chords for the shots **(A)** 169,129 and **(B)** 169,128. Frequency and growth rates of **(C)** $n = 3$ and **(D)** $n = 4$ AEs calculated by FAR3d. Unstable modes are identified with red circles, and stable modes are represented by black circles. Poloidal contour of the electrostatic potential perturbation for the $n = 3$ AE if the velocity ration is **(E)** 0.14 and **(F)** 0.06. Reproduced courtesy of AIP Publishing, Physics of Plasma journal. Figure adapted from [87]. Copyright (2018) AIP Publishing.

$f = 100 - 120$ kHz and several marginally unstable $n = 1$ modes with $f < 100$ kHz. Also, $n = 2$ and $n = 3$ modes are marginally unstable in the range of 100 – 115 and 160 kHz, respectively. For the case with $I_p = 30$ kA/T, panel i, $n = 1$ modes with $f = 40$ and 125 kHz, $n = 2$ with $f = 60$ and 120 kHz, $n = 3$ with $f = 75 - -100$ kHz and $n = 4$ with 105 kHz are unstable. FAR3d simulation results show a reasonable agreement with the experimental data during co-NBCD phase. Figure 15J shows the large distortion of the iota profile caused by the co-NBCD for an inward shifted configuration with R_{ax}, leading to an up-shit of the profile and a modification of the magnetic shear, consistent with the strong variation of the continuum gaps and AE stability along the discharge. Consequently, NBCD can be used as a mechanism to improve the AE and pressure gradient driven mode stability by optimizing the NBI operation pattern.

Another example is the analysis of the ECCD effect on LHD and Heliotron J plasmas performed using FAR3d [192]. Figure 16, panels a and b, indicates a larger AE activity in the co-ECCD discharge compared to the counter-ECCD case even though other plasma parameters such as the thermal plasma density and NBI heating pattern are the same. Panels c and e show the ctr-ECCD case has slender gaps with respect to the co-ECCD case, leading to a stronger effect of the continuum damping and the stabilization of the modes observed in the co-ECCD case, particularly a 1/2 EPM with 82 kHz, 2/3 – 2/4 TAE with 116 kHz and 3/7 – 3/8 TAE with 144 kHz identified in the FAR3d simulations. Panels d and f indicate the ctr-ECCD injection leads to lower AE activity; the 1/2 EPM and the 2/3 – 2/4 TAE (red triangles) are unstable in the co-ECCD and no-ECCD cases although stable in the ctr-ECCD case. In addition, the growth rate of the sub-dominant modes in the ctr-ECCD case is lower compared to the co-ECCD and no-ECCD cases. Thus, ECCD is an useful tool to stabilize or reduce the AE activity by narrowing the Alfvén gaps and increasing the magnetic shear at a given radial location.

Another option to modify the AE activity in fusion devices is increasing the plasma temperature using ECH. This locally affects the EP slowing-down distribution function and the AE damping effects as the thermal β increases [80, 82, 92]. Heliotron J plasmas can be heated by second-harmonic X-mode 70 GHz ECH and NBI. ECH is applied with a 70 GHz 2nd X-mode configuration for a total injection power of 0.4 MW [244]. Two NBI tangential hydrogen beam lines, BL1 and BL2, have a maximum acceleration voltage of 30 keV and a maximum power of 0.8 MW [245]. The injected ECH power is 0.3 MW, and the NBI power 1.3 MW. The experiments show the application of ECH can lead to the stabilization or further destabilization of the AE/EPM triggered by energetic ions in NBI heated plasma depending on the ECH injection power and the Heliotron J magnetic configuration [63, 71]. FAR3d is used to calculate the AE stability in different Heliotron J configurations heated by ECH and NBI [246]. Figure 17, panels a and b, show AE/EPM are almost stabilized if the ECH power increases from 100 to 300 kW. Here, we consider the decrease of the magnetic field perturbation measured by the Minov coils is a good proxy to study the improvement of the AE/EPM stability because there is no evidence of a significant displacement of the mode radial location during the ECH injection. The radial position of the AE/EPM is mainly determined by the radial location of the EP density gradient and there is no evidence of a strong impact of the ECH injection, at least in the power range explored, on the EP distribution function. Nevertheless, exploring the AE/EPM stability with respect to variations of the radial location and stiffness of the EP density gradient may provide new insights about the ECH effect on the EPs distribution function, although such analysis was out of the scope of the study. The colored stars indicate the frequency range of the

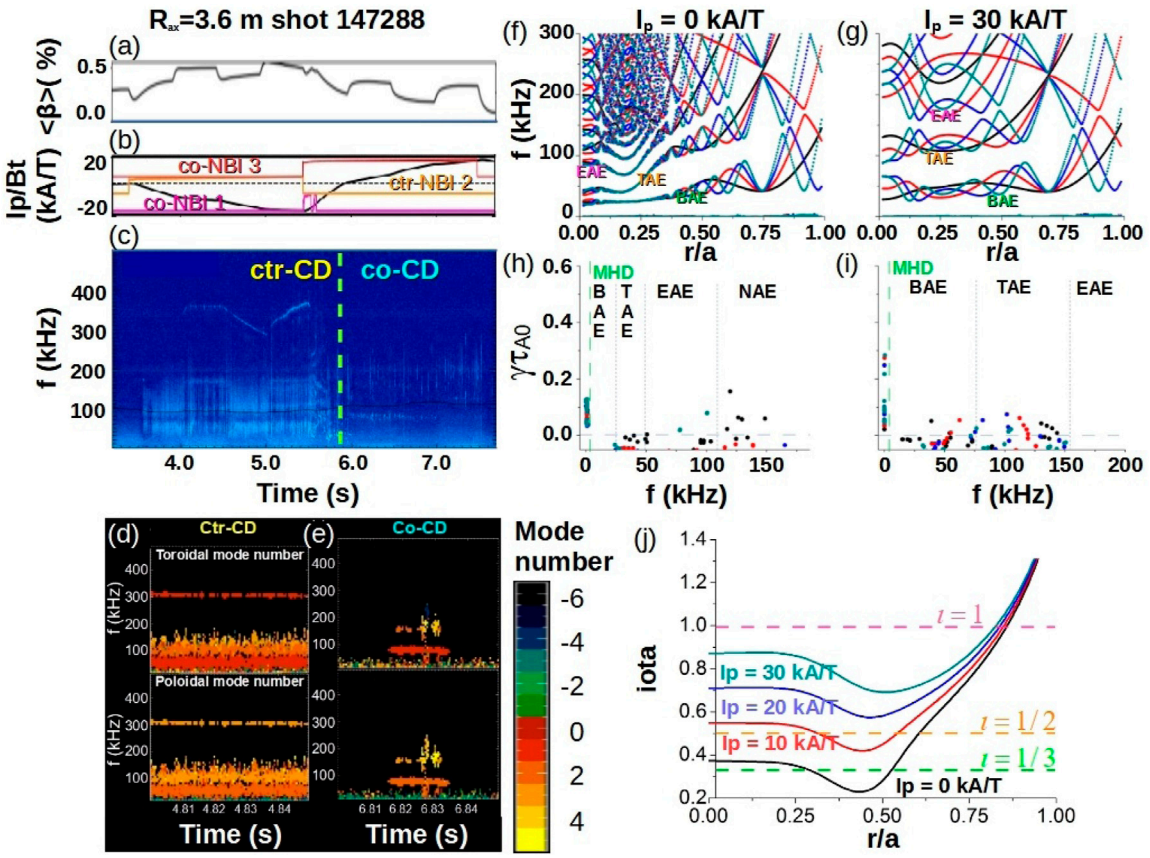

FIGURE 15
AE stability in LHD plasma with respect to the NBI current drive. Shot 147,288. **(A)** Averaged β, **(B)** toroidal current with the NBI injection pattern and **(C)** raw signal of the magnetic probe. Instability mode number measured by the magnetic probe arrays in the **(D)** ctr-NBCD and **(E)** co-NBCD phases. Continuum gaps in the configuration with **(F)** I_p = 0 kA/T and **(G)** 30 kA/T. **(H)** Growth rate and **(I)** frequency of the unstable modes calculated by FAR3d. **(J)** Iota profile for different I_p values. Reproduced courtesy of IAEA, IOPScience, Nuclear Fusion journal. Figure adapted from [243]. Copyright (2020) IAEA.

modes calculated by FAR3d. Panels c and d show the destabilization of an n/m = 1/2 EPM with f = 81 kHz and and 2/4 GAE with 132 kHz at the plasma periphery. These modes are consistent with the dominant modes, radial location and frequency range of the instabilities observed in the experiment. Panels e and f show a frequency up-shift of the Alfvén gaps as the electron temperature increases and an outward displacement of the frequency minima of the gaps. Panels g and h indicate the stabilization of the 1/2 EPM and 2/4 GAE as the electron temperature grows from 0.5 to 1 keV, consistent with the experimental observations. The ECH stabilizing effect is caused by the enhancement of the FLR and electron-ion Landau damping as well as the variation of the EP slowing down time, modifying the EP resonance features and EP β (please see Figure 4 and discussion in [246] for further information.) The analysis indicates that there is a complex interconnection between AE/EPM stability and ECH injection power, leading to the variety of experimental results obtained in Heliotron J and LHD.

5.4 Effect of multiple EP populations

The AE/EPM stability in reactor relevant plasmas must be analyzed considering all the EP species that are present, including fusion born alpha particles as well as the EPs generated for plasma heating from NBI and ICRH. The closest examples of a reactor relevant plasma to date are the experiments performed during the second Deuterium Tritium campaign in JET, in particular for the so called 3-ion radio-frequency (RF) heating scenario [247–250]. This has revealed that the AE/EPM stability and EP transport measured in these discharges can be only reproduced using numeric models if the contribution of all the EP populations is included in the analysis [99, 190].

There are several examples of multiple EP population effects that have been analyzed using FAR3d code. For example, predicting the consequences on the AE stability for ITER, DIII-D and CFETR plasma [101, 103, 104] require multiple EP species, as well as in reproducing experimental observations in LHD and JET plasmas [179, 190]. Figure 18, panels a and b, show the growth rate and frequency of the dominant modes calculated by FAR3d for the ITER reverse shear operation scenario considering only the destabilizing effect of the NBI EP (black line), only alpha particles (red line) and simulations with both NBI EP + alpha particles (blue line). The AE growth rate in the simulation with NBI EP + alpha particles is 10% lower compared to simulations with only NBI EP or only alpha particles for given range of EP β values, pointing out there is a cross-stabilizing effect between alpha particles and NBI EP driven AE/

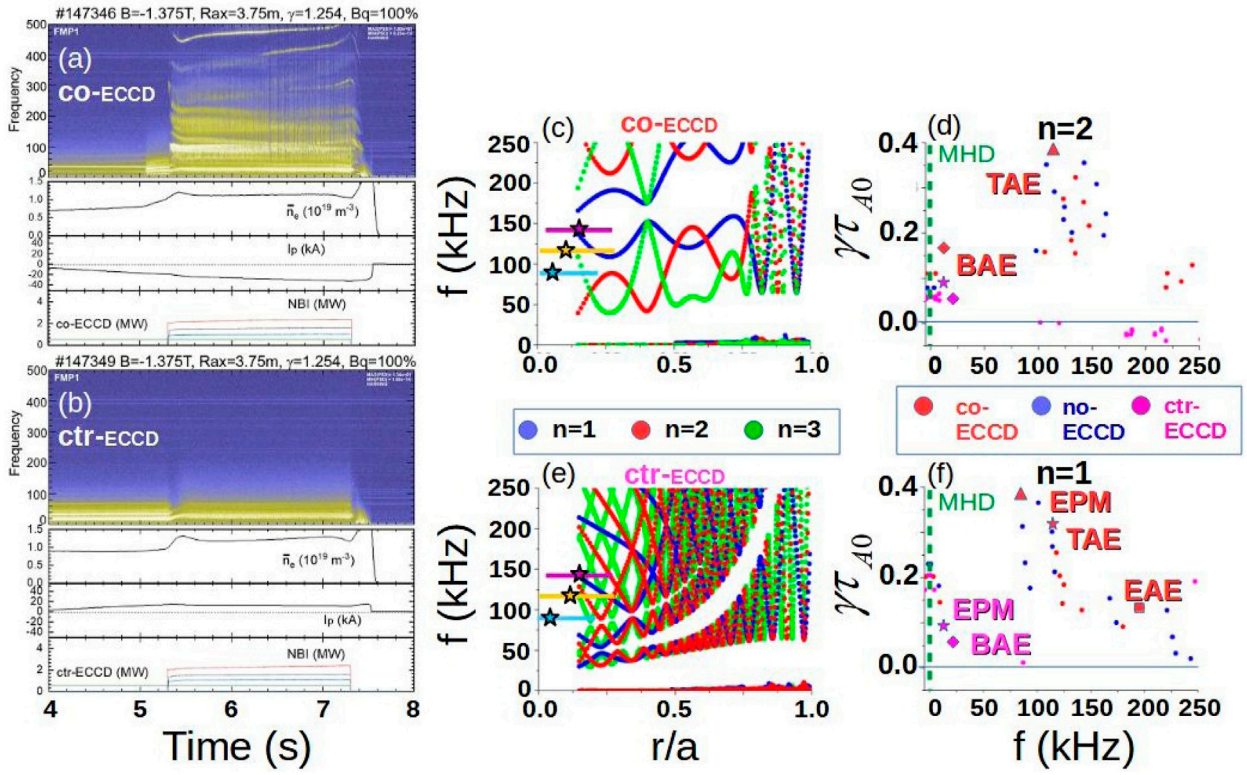

FIGURE 16
AE stability in LHD plasma with respect to the ECCD injection. Time evolution of magnetic spectrogram, electron density, plasma current and heating power in LHD discharged with **(A)** co-ECCD and **(B)** counter-ECCD. Alfvén gaps in the **(C)** co-ECCD and **(E)** ctr-ECCD cases. $n = 1$ (blue dots), $n = 2$ (red dots) and $n = 3$ (green dots) modes. The cyan star indicates the frequency range of the 1/2 EPM, the orange star the 2/3 – 2/4 TAE and the purple star the 3/7 – 3/8 TAE unstable in the co-ECCD case calculated using FAR3d. The solid color lines indicate the width of the modes eigen-function. Growth rate and frequency of the dominant and sub-dominant modes in the co-ECCD (red dots), no-ECCD (blue dots) and ctr-ECCD (pink dots) cases for **(D)** $n = 2$ and **(F)** $n = 1$ toroidal families. The solid line indicates the threshold between stable modes (negative growth rate) and unstable modes (positive growth rate). The red triangles show the modes with the largest growth rate. The red star, diamond and square indicate the most unstable sub-dominant modes in the co-ECCD case. The pink star and diamond show the most unstable sub-dominant modes in the ctr-ECCD case. Reproduced courtesy of IAEA, IOPScience, Nuclear Fusion journal. Figure adapted from [71, 192]. Copyright (2020) IAEA.

EPM. The simulations with only alphas show a destabilization of EPMs if the alpha $\beta \geq 0.02$ and EAEs if the alpha $\beta > 0.02$. The simulations with only NBI EPs show the destabilization of EPMs if the NBI EP $\beta \geq 0.01$ although low frequency modes similar to an EPM are unstable if the NBI EP $\beta > 0.02$. In the multiple EP case, the dominant modes are EPMs if the NBI EP and alpha $\beta \geq 0.01$, although triggering a low frequency EPM for $\beta > 0.01$. Panels c to e analyze the stabilizing effect of passing EPs injected by the tangential NBI on the EIC stability, triggered by the trapped EPs injected by the perpendicular NBI in LHD plasma. Consistent with that goal, the EIC growth rate and frequency, panels c and d, are calculated for a fixed β of the trapped EP while modifying the β of the passing EP. These simulations indicate that the EIC growth rate decreases as the β of the passing EP increases, i.e., increasing the tangential NBI power injection has a stabilizing effect on the EIC. Panel e shows the waiting time between EIC burst measured in LHD discharges performed using a different power injection of the tangential NBI for two perpendicular NBI configurations. The waiting time is larger as the tangential NBI power increases, that is to say the EIC are less unstable, consistent with the prediction of the simulation.

6 Saturation of AE/EPM

The analysis of the nonlinear saturation phase of AE/EPM provides information about the induced EP transport, energy transfer towards the thermal plasma and redistribution between different toroidal or helical mode families, generation of zonal structures as shear flows and zonal current, nonlinear interaction between the electromagnetic fields linked to different EP populations in addition to other effects. It is mandatory to study the saturation phase of AE/EPM to fully understand the effect of EP driven modes on the plasma heating performance and thermal plasma confinement. Nonlinear simulations performed using FAR3d can explore the saturation phase of AE/EPM potentially tracking the plasma evolution for dozens of milliseconds, providing information of the late AE/EPM saturation phase that is rarely analyzed by more sophisticated numerical models due to the large computational cost.

There are several examples in LHD and DIII-D experiments showing an important decrease of the devices performance measured during the saturation phase of AE/EPM. In particular, bursting events are linked to large EP losses and a deterioration of

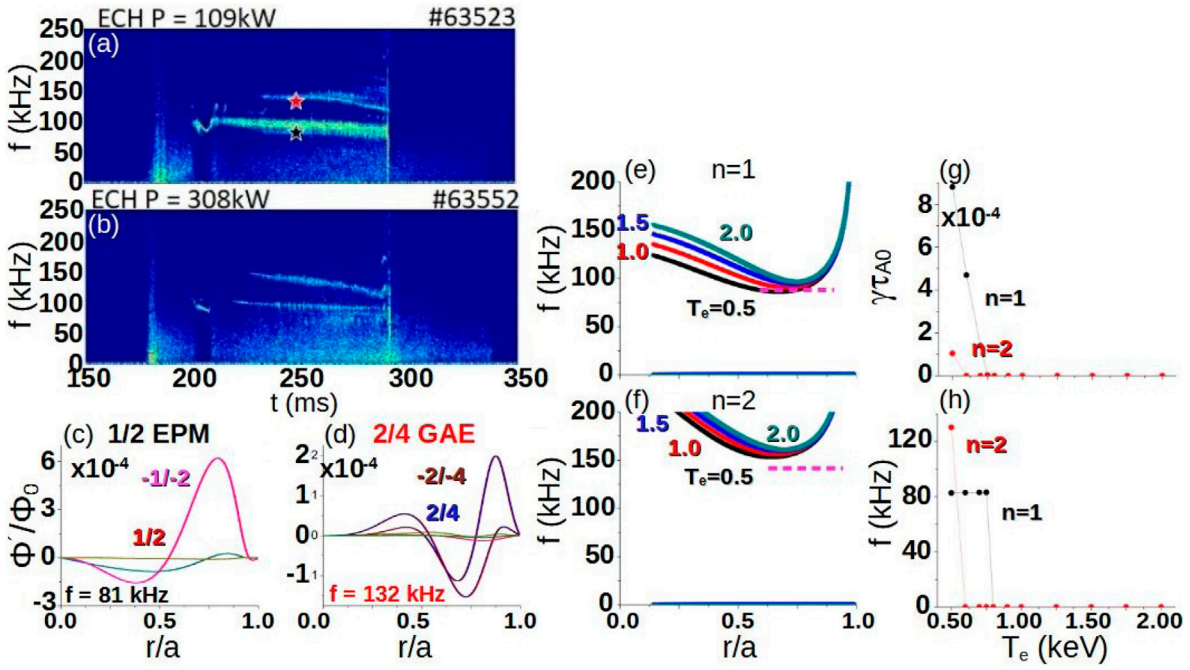

FIGURE 17
AE stability in Heliotron J plasma with respect to the ECH injection power. Magnetic spectrogram of discharges with an ECH injection power of **(A)** 100 kW and **(B)** 300 kW. The colored stars indicate the frequency range of the modes calculated by FAR3d (black $n = 1$ and red $n = 2$ modes). Mode eigenfunction calculated by FAR3d: **(C)** 1/2 EPM and **(D)** 2/4 GAE. Alfvén gap structure for different electron temperatures of **(E)** $n = 1$ and **(F)** $n = 2$ toroidal families. $T_e = 0.5$ keV (black line), $T_e = 1.0$ keV (red line), $T_e = 1.5$ keV (blue line) and $T_e = 2.0$ keV (cyan line). The dashed pink horizontal lines indicate the frequency range and eigenfunction width of the AE/EPM if EP $\beta = 0.01$. **(G)** Growth rate and **(H)** frequency of the 1/2 EPM and 2/4 GAE for different electron temperature values (EP $\beta = 0.003$). Reproduced courtesy of IAEA, IOPScience, Nuclear Fusion journal. Figure adapted from [246]. Copyright (2023) IAEA.

the plasma heating efficiency. In the following, several examples that have been analyzed using FAR3d are discussed.

The saturation of 1/1 EIC observed in LHD experiments has different phases [85]. First, a RIC is destabilized in the plasma periphery followed by the triggering of a 1/1 EIC once the perpendicular NBI power injection is large enough to exceed a given EP β threshold; this process is identified as Phase I, observed as a perturbation in the frequency range of 4 kHz. Phase II is characterized by a further destabilization of the EIC leading to an increase of the perturbation radial width. In the phase III the EIC has a bursting behavior and the perturbation frequency increases from 4 to 9 kHz, propagating inwards and showing a complex perturbation structure. Finally, in phase IV, a 1/1 magnetic island appears, the EIC stabilizes and the RIC is unstable again. FAR3d nonlinear simulations are performed to reproduce the saturation of the EIC [251]. Figure 19, panels a and b, show the perturbation of the pressure and poloidal magnetic field component calculated in the simulation, reproducing the phases I to III of the EIC observed in the experiment, in particular the bursting EIC behavior, the inward propagation of the perturbation and frequency range measured during the phase III (please see Figure 3, panels a and b, in the Ref. [84]). It should be noted that the aim of the study is to analyze why the EIC bursting phase is triggered; for this reason the simulation is terminated after the burst is observed. This is identified in the simulation as the large magnetic field oscillation in the panel b (highlighted by the vertical dashed yellow line). Panel c to f show reasonable similarities between the eigenfunction of the electrostatic potential perturbation with the electron temperature perturbation measured in the experiment during the different EIC phases (please see Figure 3, panels c to e, in the Ref. [84]). The simulations suggest the decrease of the EP population observed during the EIC burst event could be caused by the partial overlapping between t1/1 EIC, 3/4 EPM and 2/3 EPM resonances, leading to an enhancement of the outward transport of the helically trapped EP population [252]. It should be noted that The simulations show predominant horizontal contours and some vertical mixing, although the experimental contours of the electron temperature are predominatly vertical, i.e., the radial transport in the experiment is stronger.

Another example is the MHD burst observed in the LHD plasma [140]. The linear study discussed in previous sections is extended to analyze the TAEs saturation phase and the mechanism leading to the MHD burst destabilization [253]. Figure 20, panels a, indicates FAR3d nonlinear simulation reproduces the frequency range of the TAE activity observed in the experiment during the MHD burst (see Figure 10 of Ref. [140]), between 40 – −80 kHz. A pressure gradient driven mode and zonal flow activity below 20 kHz as well as an EAE in the frequency range of 110 – 150 kHz are destabilized by the nonlinear energy transfer between modes at the end of the bursting phase in the middle-outer plasma region. In addition, the simulation shows how perturbations in the frequency range of 50 – 55 kHz later extend to the frequency range between 45 and 80 kHz, consistent with the experimental observations. Panel b indicates the evolution of the poloidal magnetic field perturbation,

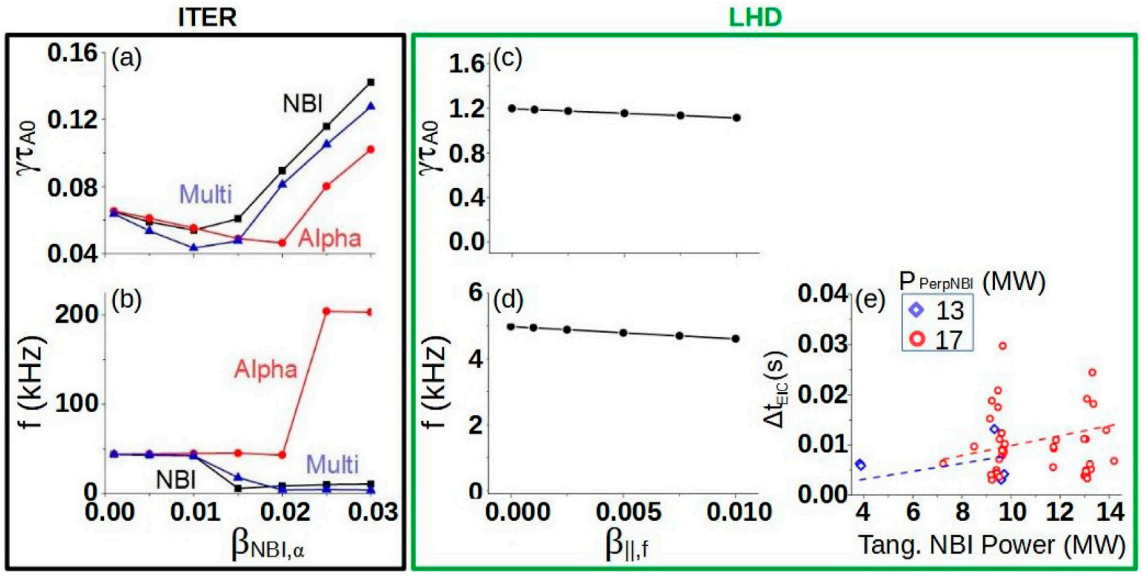

FIGURE 18
AE stability in ITER and LHD plasmas with multiple EP populations. Growth rate **(A)** and frequency **(B)** of the dominant $n = 15$ AE in ITER revere shear operation scenario for different β values of alpha particles and NBI EP in simulations with only NBI EP (black line), only alpha particles (red line) and NBI EP + alpha particles (blue line). Growth rate **(C)** and frequency **(D)** of the EIC triggered in LHD for different β values of passing EPs fixed the β of trapped EPs. **(E)** Time interval between EIC events for different tangential NBI injection intensities at a fixed perpendicular NBI injection power: blue diamonds show the discharges with a $P_{P,NBI} = 13.5 \pm 0.5$ MW and the red circles $P_{P,NBI} = 17.5 \pm 0.5$ MW. The plot includes the linear fit $\Delta t = bP_{T,NBI}$ for a perpendicular NBI injection of 13.5 ± 0.5 MW (dashed blue line) and 17.5 ± 0.5 MW (dashed red line). Reproduced courtesy of IAEA, IOPScience, Nuclear Fusion journal. Figure adapted from [101, 131, 179]. Copyright (2019 and 2020).

showing a local maximum once the MHD burst is triggered around $t = 320\mu s$, comparable with the experimental trends. Panel c indicates the perturbation eigenfunction once the MHD burst is triggered, revealing an overlapping between $n = 1$ to 3 TAEs that may explain the destabilization of the MHD burst. Panel d shows the EP density perturbation caused by the combined effect of $n = 1$ to 3 TAEs, inducing a redistribution and EP population losses. Panel e indicates the perturbation of the electrostatic potential linked to the $n = 1$ to 3 TAEs that induce the radial electric field and the generation of shear flows. Again, the simulation analysis indicate the bursting activity could be caused by the overlapping between $n = 1$ to 3 TAEs during the saturation phase of the modes.

FAR3d has also been used to study the saturation phase of AEs in tokamak devices, for example, pulsed beam discharges in DIII-D [254]. The DIII-D plasma in the discharge 176,523 is heated using a pulsed tangential NBI leading to the periodic destabilization of AEs [255]. The analysis of an isolated pulse has several advantages from the point of view of modeling because the simulations do not require source/sinks and the decay of the instability amplitude can be directly compared with the experimental data. Figure 21, panels a, shows the instability measured in the experiment at the frequency range of 105 kHz. Panel b indicates the saturation of an AE with $f \approx 100$ kHz reproduced in the simulation. Panel c shows a toroidal slice contour plot of the potential during the late saturation phase of a TAE-like perturbation. Panel d indicates a decrease of the EP density due to the EP transport induced by the TAE. The simulation indicates that the AE saturation is connected to the flattening of the EP density profile and gradient decay. A smooth relaxation of the profile is not observed due to the effect of zonal structures, which drive intermittent EP fluxes.

Optimization studies with respect to the AE saturation phase for different NBI operational regimes were performed for the DIII-D plasma using the FAR3d code, emphasizing the analysis of bursting events [256]. External actuators are used in DIII-D plasma to improve the AE stability, for example ECH [64, 257, 258], and ECCD [63, 259], or by optimizing the NBI operational regime [87, 260–262]. Nevertheless, bursting activity is detected in DIII-D EP diagnostics above a given threshold of the NBI injection power linked to avalanche-like events [263]. Figure 22, panels a, shows a chain of burst events triggered during the saturation phase of the simulation observed as a local maximum of the poloidal magnetic field perturbation. Panels b to g indicate that the burst events are correlated with a maximum of 9/3-10/3 TAE and 18/6-20/6 EAEs amplitude and the radial overlapping between the modes ($t = 1750\tau_{A0}$), that is to say, the bursts may be caused by the radial overlapping of resonances induced by different toroidal families. Panel h shows the excursion of the q profile in the plasma region where the AEs are triggered, generated by zonal currents during the mode saturation. Panel i shows a decrease of the EP density linked to an enhanced EP transport induced by the AEs. Panel j indicates that the pressure profile is also modified along the simulation because the shear flows generated by the AEs during the saturation modifies the plasma flux surfaces. The different parametric studies performed analyzing the effect of the NBI injection power, voltage and deposition region on the AE saturation phase with FAR3d reproduce similar trends compared to DIII-D experiments [60, 161, 263], in particular the critical gradient behavior [264]. The spectrum of the poloidal magnetic field perturbation (Figure 15, panels a and b in the Ref. [256]), indicate a complex interplay between n = 3 and 6 AEs as well as with

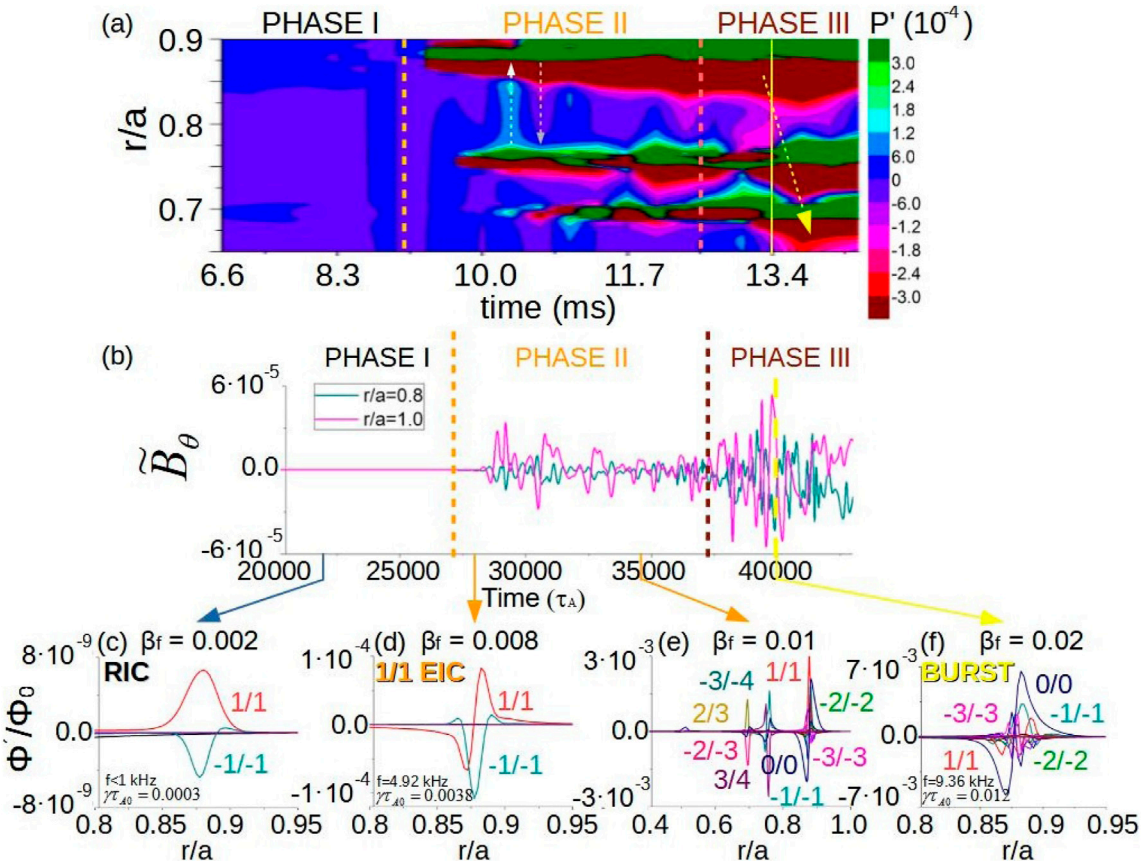

FIGURE 19
Analysis of the saturation phase of EIC in LHD plasma. **(A)** Evolution of the pressure perturbation between r/a = 0.65 – 0.9. The orange dashed lines indicate the transition between 1/1 EIC phases. The dotted white/gray lines indicate the counter-propagating perturbations during Phase II. The solid yellow arrow indicates the burst event and the dotted yellow line the inward propagation of the 1/1 EIC perturbation during Phase III. **(B)** Time evolution of the poloidal component of the magnetic field perturbation at r/a = 1.0 (pink line) and 0.8 (cyan line). Eigenfunctions of the electrostatic potential perturbation at **(C)** $t = 22000\tau_{A0}$, **(D)** $28000\tau_{A0}$, **(E)** $34000\tau_{A0}$ and **(F)** $40000\tau_{A0}$. Reproduced courtesy of IAEA, IOPScience, Nuclear Fusion journal. Figure adapted from [251]. Copyright (2021) IAEA.

the thermal plasma, leading to a large spreading of the AE activity in frequency and the destabilization of multiple overtones, particularly after the system enters in the bursting phase. The strongest activity is observed in the frequency range of 150–400 kHz around r/a = 0.4.

The analysis of shear flows induced by AE/EPM is also performed in LHD and JET plasmas; in particular such shear flows can have consequences on the thermal plasma confinement and plasma turbulence level. Numerical studies may indicate that the plasma turbulence could be modified during the AEs saturation phase although there are only indirect experimental evidences of the shear flows generated by AEs [265–271]. For example, shear flows induced by RSAEs in EAST experiments may help in the generation of electron-internal transport barriers, reducing the requirements for the L-H transition [272]. In the JET experiment, shear flows induced by AE/EPMs may improve the thermal plasma confinement [190]. FAR3d is applied to investigate the generation of shear flows and the effect on the plasma turbulence and confinement in LHD, JET and DIII-D devices [254, 273, 274]. Regarding LHD plasmas, the analysis shows reasonable similarities between simulations and experiments, reproducing at the same radial location shear flows measured during EIC and MHD bursts by the charge exchange spectroscopy diagnostic. Simulations dedicated to JET DT discharges indicate shear flows linked to the saturation of TAEs and fishbones may improve the thermal plasma confinement.

7 Predictions

Another contribution of FAR3d is in the forecasting of AE/EPM stability for future nuclear fusion devices, particularly ITER, CFETR or reactor relevant experiments in JT60SA. Predicting the AE/EPM stability may help to improve the plasma heating performance by identifying unfavorable configurations or regimes that should be avoided, as well as anticipating efficient methods for reducing AE/EPM destabilization.

The ITER plasma will be heated by two NBIs providing 33 MW of power, injecting a Deuterium beam with an energy of 1 MeV or a Hydrogen beam of 0.85 MeV [275]. Extrapolations from present experiments and numerical simulations predict the destabilization

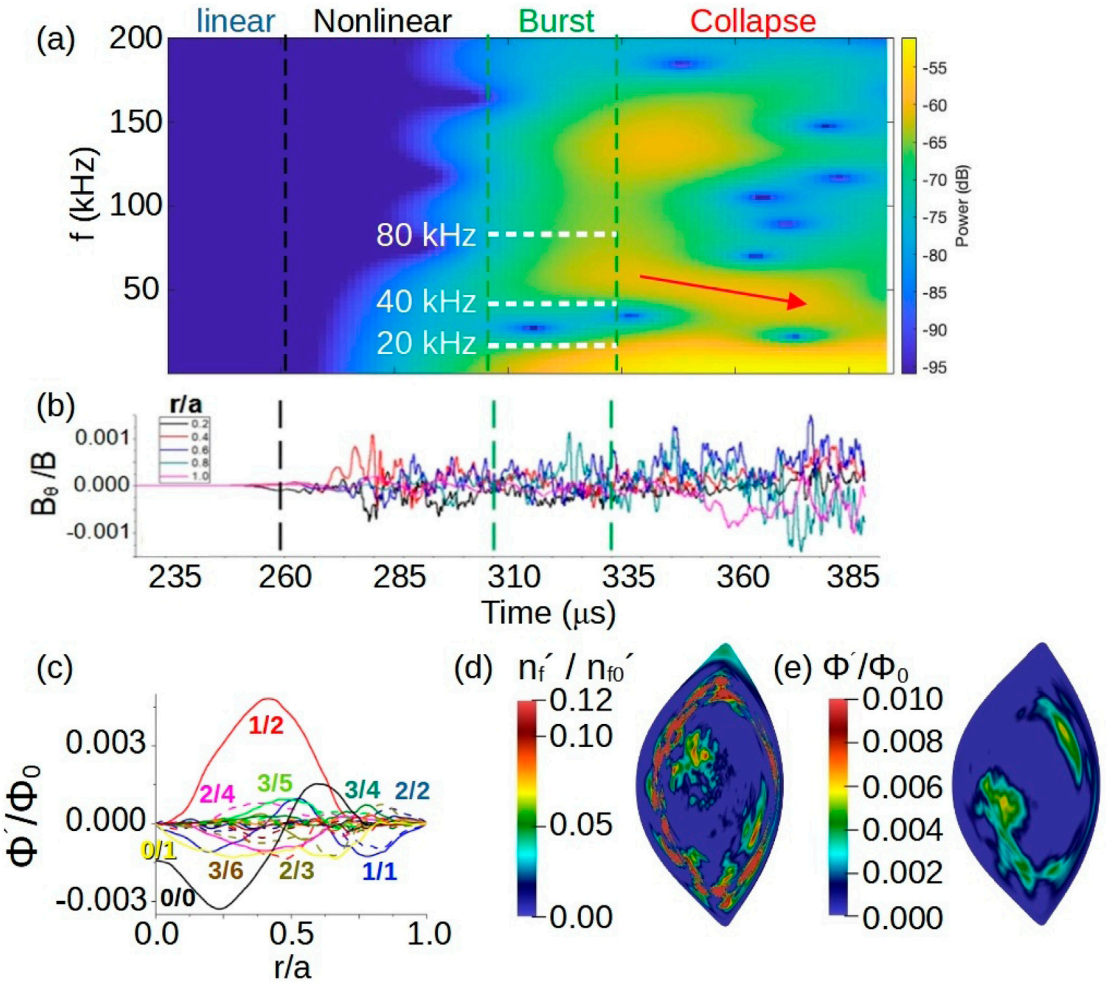

FIGURE 20
Analysis of the MHD burst in LHD plasma. **(A)** Spectrogram of the poloidal component of the magnetic field perturbation during the nonlinear simulation. **(B)** Evolution of the poloidal component of the magnetic field perturbation **(C)** Eigenfunction of the electrostatic potential perturbation during the MHD burst. Poloidal contour of the perturbations of the **(D)** EP density and **(E)** electrostatic potential during the MHD burst. Reproduced courtesy of IAEA, IOPScience, Nuclear Fusion journal. Figure adapted from [253]. Copyright (2021) IAEA.

of AE/EPM by the NBI as well as fusion born alpha particles [276–284]. FAR3d is used to calculate the linear stability of the ITER plasma with respect to the NBI and alpha particle destabilizing effects on reverse shear, hybrid and steady state configurations [101]. Figure 23 shows an example of the analysis dedicated to the reverse shear scenario. Panel a indicates the Alfvén continuum of the $n = 15$ toroidal mode family, showing a BAE gap below 25 kHz, a TAE gap at 40–100 kHz covering the middle-outer plasma region, and an wide EAE gap from 100–230 kHz along all the plasma radius. Panels b and c show the destabilization of $n = 11$ to 20 EPMs by alpha particles in the frequency range of 40 − 50 kHz. Increasing the alpha β leads to a transition from the EPMs to EAEs with 170 − 230 kHz. Panels d and e indicate NBI EPs can destabilize $n = 11$ to 20 RSAEs or BAEs, as well as EPMs with frequencies between 5 − 20 kHz as the NBI EP β increases.

CFETR high poloidal β configurations are projected to be a possible steady state operation scenario for future nuclear fusion reactors [285–287]; although it is mandatory to achieve an efficient plasma heating by the avoidance or minimization of AE/EPM activity. The CFETR plasma will be heated by NBI, ECW and lower hybrid waves (LHW). The tangential negative-ion-based NBI will inject a power of 5 MW in a Deuterium beam with an energy of 350 keV, leading to the possible destabilization of AE/EPM in conjunction with the fusion born alpha particles. FAR3d has been used to analyze the AE/EPM stability in two CFETR high poloidal β configurations with respect to the radial location of the ITB, at $r/a = 0.45$ (case A) and 0.6 (case B) [103]. Figure 24, panels a and b, indicate for both configurations the presence of a BAE gap in the frequency range of 80 kHz in the inner plasma decreasing below 50 kHz at the plasma periphery. There is also a TAE gap in the middle-outer plasma region between 50 and 120 kHz for case A, only observed at the outer plasma in case B. Both cases show a wide EAE gap at frequencies above 70 kHz, particularly in the inner plasma region. Panels c and d indicate that the AEs growth rate in case A is 3 times smaller compared to case B because the modes are triggered in the inner plasma region where the magnetic shear is stronger. On top of that, AEs triggered in case A are separated with respect to the EP loss cone in phase space calculated using the code

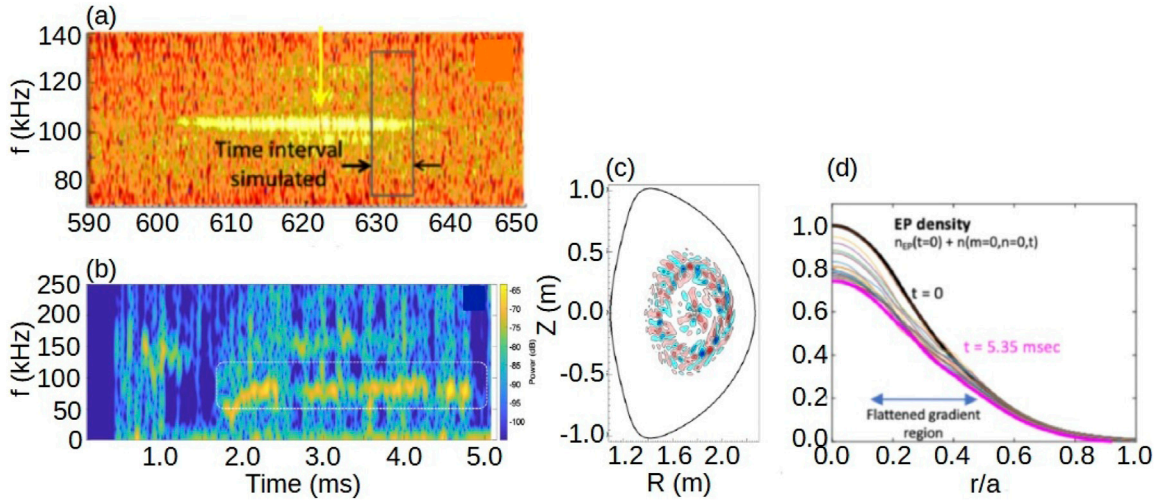

FIGURE 21
Analysis of the AEs saturation phase in DIII-D plasma heated using a pulsed tangential NBI. **(A)** Frequency vs. time spectrogram of magnetic probe *dB*/*dt* data for DIII-D discharge 176,523 highlighting the simulation interval (black box). **(B)** Spectrogram of the poloidal component of the magnetic field perturbation at $r/a = 0.2$ calculated by FAR3d. Dominant perturbation highlighted by a dashed white rectangle. **(C)** Poloidal contour of the electrostatic potential perturbation at $t = 2.24$ ms in FAR3d simulation. **(D)** Initial and final EP density profiles in FAR3d simulation. Reproduced courtesy of IAEA, IOPScience, Nuclear Fusion journal. Figure adapted from [254]. Copyright (2021) IAEA.

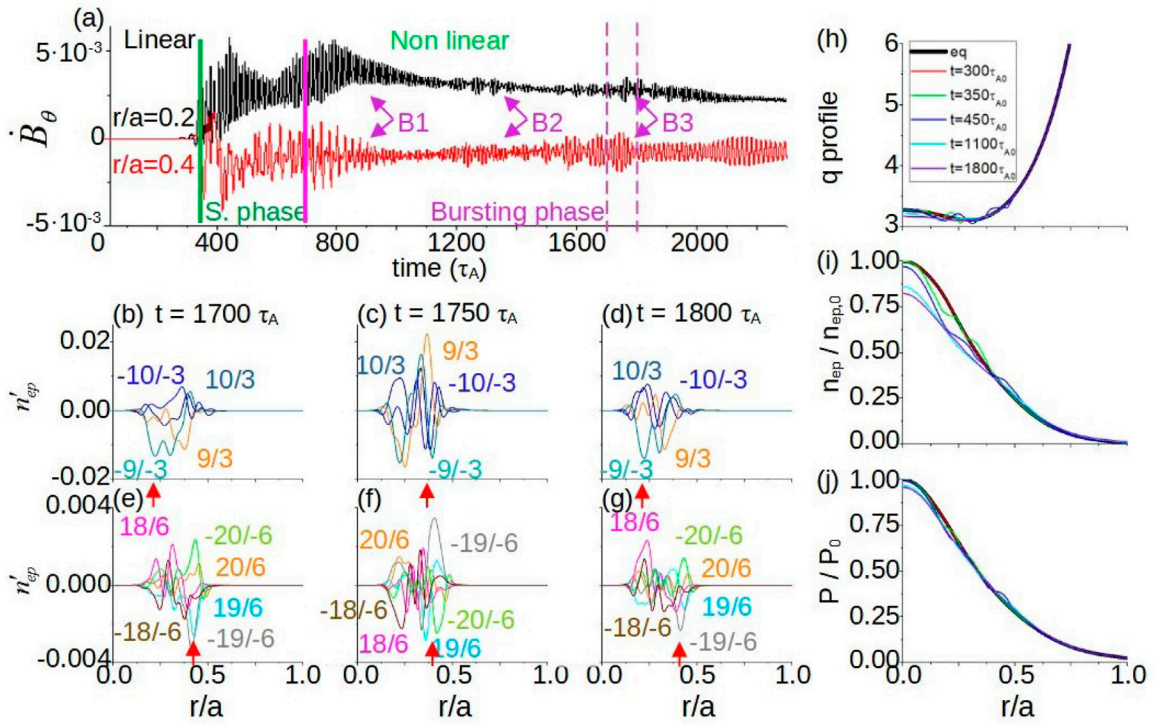

FIGURE 22
Analysis of the bursting activity in DIII-D plasma. **(A)** Perturbation of the poloidal component of the magnetic field in the nonlinear simulations with an EP β of 0.02. The vertical bold green lines indicate the transition from the linear to the saturation phases. The vertical bold pink line indicates the beginning of the bursting phase (the bursts are indexed as B + number). The vertical dashed pink line shows the bursting event analyzed. Eigenfunctions of the density perturbation for $n = 3$ AE at **(B)** $t = 1700\tau_{A0}$, **(C)** $t = 1750\tau_{A0}$ and **(D)** $t = 1800\tau_{A0}$. Eigenfunctions of the density perturbation for $n = 6$ AE at **(E)** $t = 1700\tau_{A0}$, **(F)** $t = 1750\tau_{A0}$ and **(G)** $t = 1800\tau_{A0}$. Evolution of the equilibrium profiles: **(H)** safety factor, **(I)** EP density and **(J)** pressure profiles. Reproduced courtesy of IAEA, IOPScience, Plasma Phys. Control. Fusion journal. Figure adapted from [256]. Copyright (2023) IAEA.

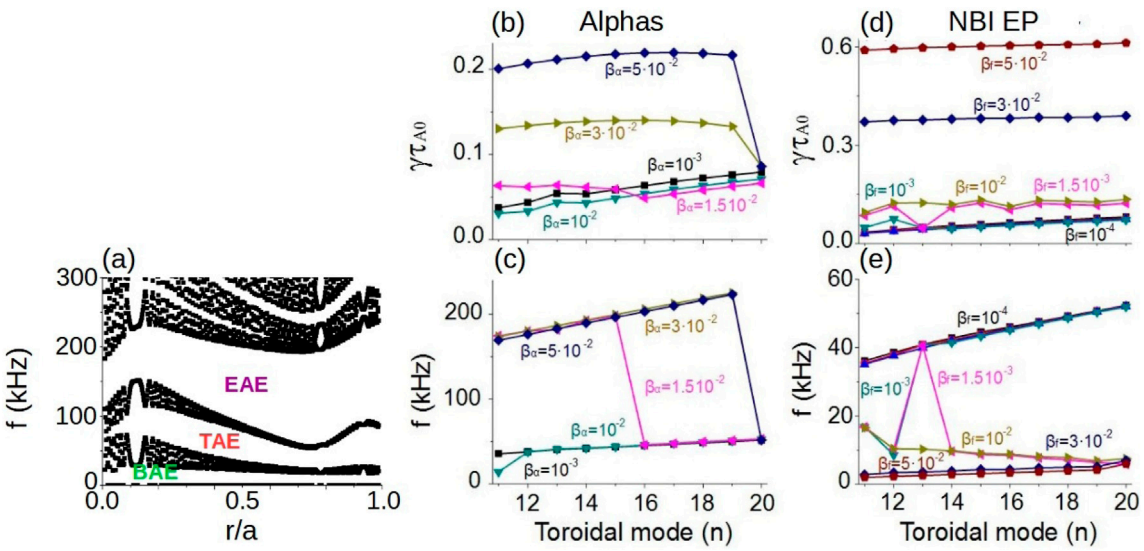

FIGURE 23
AE stability in ITER plasma including the effect of multiple EP populations (NBI EP + alpha particles). **(A)** Alfvén gaps of $n = 15$ toroidal mode family for ITER reverse shear case. Growth rate **(B)** and frequency **(C)** of the dominant mode destabilized by the alphas particles for different EP β values and mode numbers. Growth rate **(D)** and frequency **(E)** of the dominant mode destabilized by the NBI EP for different EP β values and mode numbers. Reproduced courtesy of IAEA, IOPScience, Nuclear Fusion journal. Figure adapted from [101]. Copyright (2019) IAEA.

ORBIT [284], located at $r/a = 0.7$, although closer to the radial locations of the AEs destabilized in case B [288]. The simulations show the AEs are induced by the alpha particles drive, triggering BAEs and EAEs at the inner-middle plasma region. On the other hand, the destabilizing effect of the NBI EP is rather small. Low n toroidal mode families show the fastest growing instabilities because EP FLR effects cause a strong stabilizing effect on high n perturbations. It should be noted that the simulations do not identify EPMs as dominant modes. In summary, low n alpha particle driven modes can reduce the operational performance of CFETR high poloidal β configurations, particularly if the ITB is located further away from the middle plasma region.

JT-60SA is a critical milestone in nuclear fusion research, designed to test ITER and DEMO operational scenarios [289–292], for example the ITER-like inductive scenario [293]. The JT-60SA plasma will be heated using 34 MW of NBI power, including 12 positive-ion-based and 2 negative-ion-based NBIs (N-NBI). The N-NBI will inject a power of 10 MW using Deuterium with an energy of 500 keV; injectors will be aimed at the magnetic axis and middle plasma region [294, 295]. The destabilizing effect of the N-NBI EP may cause a triggering of AEs in the JT-60SA plasma [296–298]. FAR3d is used to forecast the AE activity in the JT-60SA ITER-like inductive scenario [299]. Figure 25, panel a, shows rather wide TAE and EAE gaps covering main part of the plasma radius. Panels b to g show $n = 4$ BAE and TAE can be triggered by low energy EP at the end of the thermalization process if the EP population is large enough. On the other hand, an $n = 2$ TAE is destabilized by weakly thermalized EP, even though the EP population is not large. Panels h to j indicate that TAEs are triggered in the middle of the plasma although the BAE is unstable near the magnetic axis. Consequently, JT-60SA performance may be reduced by the destabilization of AEs in the ITER-like inductive scenario.

8 Discussion

In this section the main findings of FAR3d are discussed and contextualized. In addition, the main advantages and drawbacks of the model are commented on. Next, FAR3d bench-marking studies with other codes are summarized.

8.1 Summary of main findings

One of the early applications of FAR3d code was to reproduce the AE activity measured in different devices, for example TAEs and EIC in LHD, HAEs in TJ-II or GAE and EPM in Heliotron J plasma. Some of these instabilities were reproduced for the first time. These analyses also introduced parametric studies as a new tool to analyze the AE/EPM stability with respect to the EP resonance features (as determined by variations in the input EP profiles/parameters used in the model).

Follow up studies were then dedicated to reproduce the AE activity in high poloidal β and reverse shear configurations of DIII-D, as well as the EIC activity in different LHD operational scenarios. FAR3d was also used to perform optimization studies with respect to the magnetic field configuration, NBI operational regime and thermal plasma parameters. Consequently, FAR3d code is the first tool used to identify configurations with optimized plasma heating performance with respect to the linear and nonlinear stability of AEs/EPMs.

It is important to mention FAR3d simulations were also used to calibrate the EP profiles obtained from other codes. This technique was applied to reproduce the AE activity measured in EAST discharges after Tungsten plasma contamination and AE/EPM observed in Heliotron J discharges. This implies that FAR3d can be also used to calibrate the EP input profiles of more sophisticated

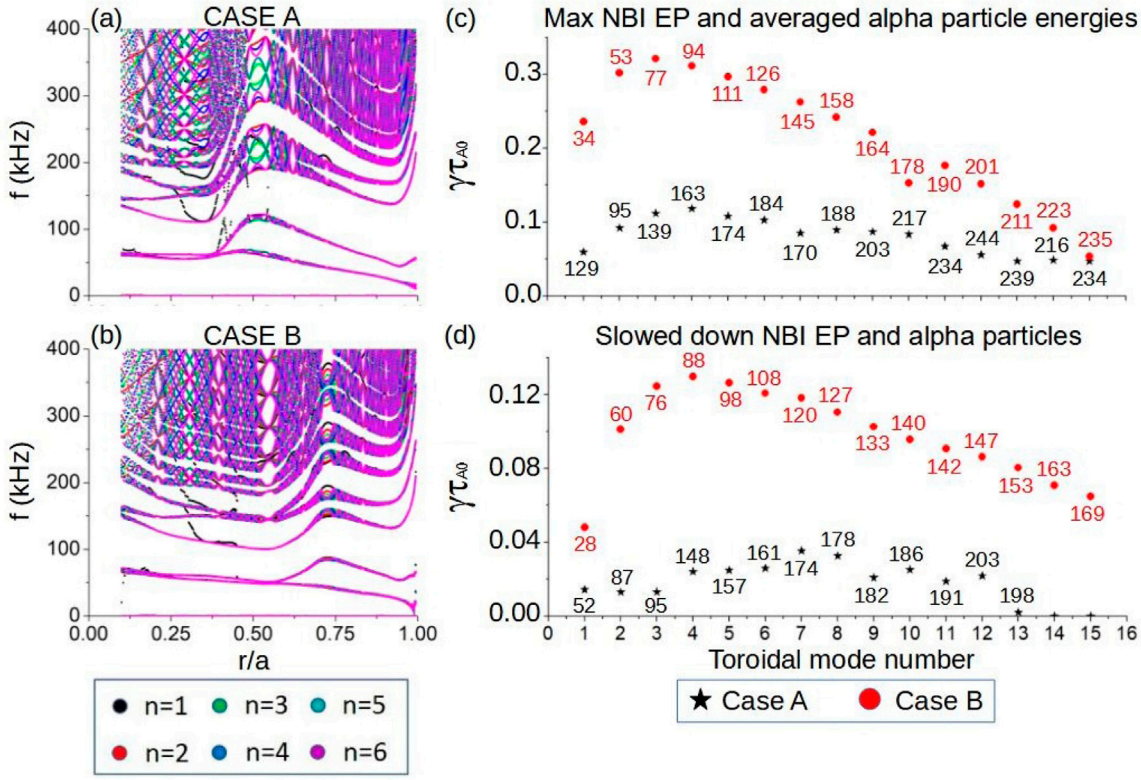

FIGURE 24
AE stability in CFETR plasma considering multiple EP populations (NBI EP + alpha particles). Continuum gaps of cases **(A)** A and **(B)** B for $n = 1$ to 6 toroidal mode families. Growth rate of $n = 1$ to 15 dominant modes in the case A (black stars) and Case B (red circles) for **(C)** non thermalized NBI EP with 350 keV and alpha particles with the an averaged energy of 1,090 keV, **(D)** thermalized NBI EP (below 250 keV) and alpha particles (below 800 keV). The frequency of the mode is added in the graphs. The simulations are performed including both NBI EP and alpha particles populations. Reproduced courtesy of IAEA, IOPScience, Nuclear Fusion journal. Figure adapted from [103]. Copyright (2022) IAEA.

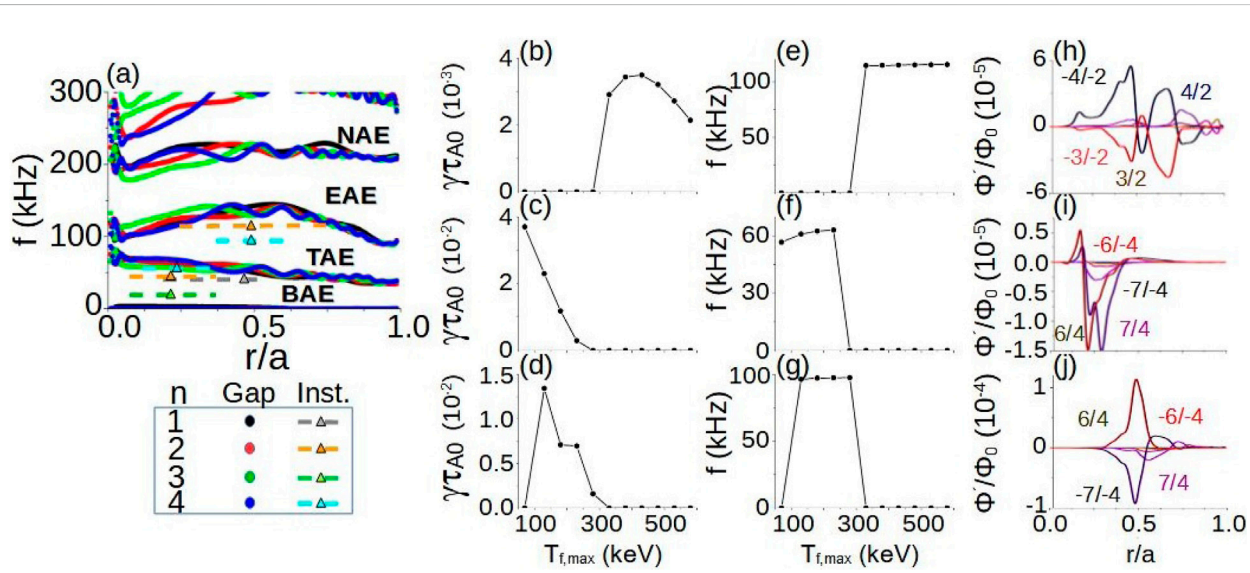

FIGURE 25
AE stability in JT60SA ITER-like inductive scenario. **(A)** Alfvén gaps of JT60SA ITER-like inductive scenario. The dashed lines indicate the width of the unstable AEs and the triangles the eigenfunction maxima. **(B)** Growth rate and **(E)** frequency of $n = 2$ TAE, **(C)** growth rate and **(F)** frequency of $n = 4$ BAE, **(D)** Growth rate and **(G)** frequency of $n = 4$ TAE for different NBI EP energies. Eigenfunctions of the electrostatic potential of **(H)** $n = 2$ TAE, **(I)** $n = 4$ BAE and **(J)** $n = 4$ TAE. Reproduced courtesy of IAEA, IOPScience, Nuclear Fusion journal. Figure adapted from [299]. Copyright (2020) IAEA.

models, providing a first guess of the EP characteristics that are consistent with the AE/EPM activity observed in the experiment. Through this approach, FAR3d can reduce the parametric range and the computational cost of studies performed by gyro-kinetic and hybrid codes.

Another topic covered by FAR3d simulations was reproducing the AE/EPM/interchange mode stability trends observed in LHD, Heliotron J and TJ-II discharges if external actuators as ECCD, ECH or NBCD are applied. The reasonable success in reproducing such trends opens the possibility of using the FAR3d code to predict operational scenarios for future devices as JT60SA, ITER and DEMO with optimized AE/EPM stability with assistance from the application of external actuators.

Bursting activity in LHD and DIII-D plasmas was analyzed by performing long term nonlinear simulation with the FAR3d code, analyzing the AE/EPM saturation phase. The simulations show that the destabilization of bursts may have common features in both devices; these events could be triggered due to the overlapping of resonances induced by different toroidal mode families. Moreover, the analysis may indicate the bursting activity is a universal feature of plasma systems undergoing a transition from the soft MHD limit, with local relaxations, to the hard MHD limit, with global relaxations. Another important conclusion comes from the EP transport enhancement in the simulation bursting phase, reproducing the critical gradient behaviour proposed to explain the EP loss measurements in DIII-D bursting plasma. Furthermore, nonlinear simulations dedicated to analyze the saturation phase of interchange modes in LHD plasma may indicate, internal collapse and sawtooth-like events are also caused by a transition from the soft to the hard MHD limit, leading to a partial stochastization of the magnetic field due to overlapping magnetic islands [300–302]. In summary, operational scenarios with plasma in the hard MHD limit must be avoided in future fusion reactors, leading to an important reduction of the heating performance by massive EP losses and damage to plasma facing components.

A crucial topic for fusion reactors explored by FAR3d linear and nonlinear simulations is the AE/EPM stability in plasma with multiple EP species. The analysis indicates the experimental observation in the second JET DT campaign can only be explained if multiple EP effects are included in the simulations, in particular the alpha particle losses measured once fish-bones are destabilized. Efficient plasma heating in future fusion reactors requires the minimizing alpha particle losses, thus the nonlinear destabilization of the alpha particle population by NBI and ICRH EPs below the β threshold of alpha particle driven AEs is an important issue that must be studied in detail. Other linear studies were dedicated to analyze the AE stability in plasmas with multiple EP populations in CFETR and ITER devices, as well as multiple NBI driven EP plasmas in DIII-D and LHD theoretical configurations.

FAR3d analysis dedicated to study shear flows generated during the AE/EPM saturation phase may indicate important consequences for thermal plasma confinement. The trends identified in simulations comparing the intensity of the shear flows for different JET DT discharges may support this possibility, reproducing the improved thermal plasma confinement measured in the experiments. This result may indicate that the thermal plasma confinement in ITER and DEMO could be better than expected.

Another contribution of the FAR3d studies is to forecast the AE/EPM stability in ITER, JT60SA and CFETR for different operational scenarios. In addition, the AE/EPM stability has been studied in stellarator devices exploring different magnetic configurational symmetries. Operational scenarios and magnetic configurations with strong AE/EPM activity could lead to fusion reactors with poor plasma heating efficiency and must be avoided.

The analysis of the linear and nonlinear interaction between EPs and and interchange, ballooning, kink and tearing modes may indicate, EPs have a stabilizing effect below the β required to destabilize AE/EPM. This result opens the possibility of using EPs beneficial effects to improve the MHD stability of fusion devices, reproducing experimental observations already reported in LHD, TJ-II and DIII-D discharges.

8.2 Advantages and drawbacks of the FAR3d gyro-fluid model

The main motivation of developing gyro-fluid models is the computational efficiency. Thus, FAR3d allows the rapid characterization of the AE/EPM activity measured experimental studies. Examples of a reasonable agreement between simulations and experimental observations has been obtained in studies dedicated to JET, DIII-D, EAST, LHD, TJ-II and Heliotron J discharges.

Developing reduced models while retaining the key elements for a first order characterization of the AE/EPM linear and nonlinear stability, opens the possibility of performing massive parametric studies, providing useful information for optimization studies. Such improved scenarios can be tested in experiments dedicated to confirm theoretical optimization trends. These kind of experiments were performed in LHD, leading to promising results. Additionally, the model simplifications enable analysis of the AE/EPM late nonlinear saturation phase including multiple EP species and toroidal families, approaching the stability of reactor relevant plasma. These studies may provide relevant information about the induced EP transport, zonal structure generation and nonlinear interactions between EP populations, thermal plasma and different toroidal mode families in ITER and DEMO plasmas.

Besides these advantages of the FAR3d model, the limitations on the model can be explicitly stated. The FAR3d two moment version can only explore parallel and velocity-specific trapped resonances induced by Maxwellian EP distribution functions. Introducing a slowing down EP distribution function requires, at least a three moment version of the code, including an evolution equation for the EP energy moment perturbation. The three moment Landau closure, that requires five parameters, is able to fit the gyro-kinetic response function for an EP slowing down distribution function, although benchmarking of the three moments version of FAR3d against the two moments version is still underway. Further development and testing of both the three and a four moment version of FAR3d (adds the parallel EP heat flux moment) is ongoing. Additionally, versions of FAR3d are under development based on perpendicular and parallel perturbed EP pressure moments. This moment hierarchy should be especially appropriate for anisotropic EP populations. It also allows a more accurate treatment of the resonance contributions of the drift (also

know as toroiddal) resonances. In the meanwhile, the resonance induced by a slowing down EP distribution function can be approximated performing parametric studies using multiple Maxwellian distributions, fitted to the EP populations and encompassing the key resonances in the experiment. It should be noted that the results of the parametric studies must be analyzed with care because not all the resonances identified reproduce the real resonances in the experiment. On top of that, the Maxwellian is a symmetric distribution function, thus FAR3d simulations cannot at this time distinguish between co- and ctr-passing EPs.

The trapped EP approximation should be considered a first order step in the analysis of resonances induced by toroidal and helically trapped EP, thus the code predictions may deviate from the parametric ranges of the experiment. An improved approximation requires introducing the parallel and perpendicular components of the pressure tensor, an active research topic in the FAR3d project. However, the present trapped EP module provides a reasonable approximation of the resonance induced by trapped helical particles that can destabilize the EIC in the LHD device. The resonance induced by particles with different pitch angles can be also approximated by adapting the bounce distance and frequency of the trapped EP in the model.

EP resonance effects and destabilization are approximated by the parallel Landau closure coupled with the average drift velocity and diamagnetic drift frequency operators. In addition, the fitted Maxwellian EP distribution function used in the simulations is allowed to deviate with respect to the real EP distribution in the experiment. This is motivated by the hypothesis that the drive for AE instabilities from configuration space gradients may dominate over that from velocity space gradients (which may be resolved by higher frequency activity). For this reason the analysis of the AE/EPM stability trends can deviate from the experimental observations if the parametric range of the resonance is not correctly identified. As a consequence, the EP β threshold to trigger AE/EPM may be different in the simulations and the experiment. Performing parametric studies may help to reduce discrepancies, by exploring a wide parametric range to identify the model setup that better approximates the real resonance. Consequently, the best FAR3d performance is obtained in the identification of AE/EPM stability trends, not in the accurate predictions of the AE/EPM stability thresholds.

FAR3d results shows a large sensitivity to the EP configuration introduced in the model. In general, EP profiles obtained from other codes as TRANSP, ASCOT, ONETWO/NUBEAM or MORH have to be calibrated by performing parametric studies to identify the optimal configuration that better reproduces the EP resonance and AE/EPM stability in the experiments.

The present version of the model does not include the parallel magnetic field perturbation, leading to an artificial stabilizing effect on ideal current driven modes and low frequency AEs [303–305]. This limitation causes the inability of the model to study ideal internal kinks. Thus, an improved description of the fish-bone stability requires introducing the parallel magnetic field perturbation. The analysis of fish-bones is possible using FAR3d code by including the effect of the resistivity in the simulations, leading to the destabilization of resistive internal kink modes. The growth rate of the mode is not as large as the ideal internal kink calculated by full MHD codes as MISHKA [306] for the case of JET discharges, although the simulation provides a first approach of the phenomena. The consequence is, the EP β required to destabilize fish-bones is higher compared to the experiment. For the case of the EIC, the seed instability of the EPM is a resistivity interchange mode, thus the lack of the parallel magnetic field perturbation is less restrictive, reason why FAR3d code show reasonable similarities between the EP β required to destabilize the EIC in the simulations and in the experiment [327].

Neoclassical effects are not included in the model, consequently the stability of neoclassical tearing mode cannot be analyzed. Introducing the highly anisotropic thermal plasma heat transport required for a correct description of the current depletion in the island regions is a numerically challenging problem. A future FAR3d module will explore possible implementations.

The numerical stability of nonlinear FAR3d simulations can pose a limitation in configurations with strong drive, particularly if rather large perturbations induced by multiple EP resonances and pressure gradient/currents develop at the same time. Such simulations show a strong overshot in the transition from the linear to the saturation phase, leading to a large decrease of the time step of the simulation, required by the code to channel the energy/information flows in the system, leading eventually to ending the run. In such circumstances, diffusive and damping terms must be enhanced to reduce the free energy of the model and force a smoother transition to the saturation phase. The other possible strategy consists in including a larger number of stable toroidal mode families that provides an energy sink at short wavelengths.

FAR3d simulations exploring the late saturation phase of AE/EPM may show the destabilization of modes not observed in the experiment or an overestimation of marginal unstable modes. This is caused by an inaccurate nonlinear energy redistribution from the dominant perturbation towards different toroidal mode families, other EP populations and the thermal plasma. This is explained by the role of the high n modes in the simulations, stabilized by the FLR effects, that should participate as energy sinks. If the high n modes are not included, the fraction of the free energy that should be dissipated by the non linearly energy cascade to high n modes is still available to trigger instabilities. This issue is minimized by including a larger number of toroidal modes families, equilibrium poloidal modes and EP species with a non negligible population in the plasma.

The FAR3d model is based on perfect conducting fixed boundary conditions at the plasma edge. Consequently, the calculation of ballooning modes and AE/EPM at the pedestal of tokamak plasma is problematical; free boundary conditions are mandatory to avoid an overestimation of the growth rates for such modes.

Single fluid models can only reproduce the stability of plasma in the slow reconnection regime, that is to say, plasma with a non negligible effect of the resistivity. Consequently, FAR3d simulations do not make accurate descriptions of plasma relaxations induced in the fast reconnection regime. For example, the plasmoid instability cannot be reproduced, or events that significantly reduce the free energy available to trigger other instabilities. Consequently, single fluid simulations overestimate the growth rate of perturbations triggered in high temperature plasma with low resistivity, that is to say, instabilities triggered in the core of fusion devices. This limitation particularly affects pressure gradient and current driven modes, although the impact is smaller for AE/EPM. Two fluid

modes are required for an improved description of the system stability.

FAR3d studies performed for tokamaks including the pedestal can show artificial modes with rather large growth rates at the plasma edge. This is caused by spurious currents that can appear in equilibria generated by the VMEC code nearby the outer model boundary. This issue can be avoided in linear simulation using the eigen-solver version of the code by excluding spurious modes and retaining only the physically relevant modes. In addition, it is also well known that the VMEC code provides a poor description of the magnetic surfaces near the magnetic axis. This issue can be partially resolved by the interpolations used nearby the magnetic axis. That may cause an incorrect identification of the perturbation mode number in the inner plasma region.

Non linear simulations performed using a large number of toroidal modes families including multiple EP populations and FLR damping effects require a large amount of RAM memory due to the size of the matrix generated by the numerical model. Thus, the range of poloidal modes must be limited by removing fluid and wave-EP resonances that may not have an important impact on the instability analyzed, for example, ignoring peripheral resonances if the target modes are located in the inner plasma region.

The MPI parallelization of the nonlinear FAR3d version is performed with respect to the number of toroidal/helical mode families included in the simulation. Consequently, inputs keeping the same range of resonances for low n and high n toroidal mode families, that require extending the number of poloidal modes as the toroidal mode number increases, lead to load inbalances and limit the gains from parallelization. The code stepping speed is limited by the number of poloidal modes of the highest toroidal mode family. In addition, the eigen-solver version of the code is not yet parallelized and can be rather slow compared to the initial value solver, particularly for the analysis of high n toroidal mode families.

Thermal and EP FLR effects must be used with care because activating these modules can lead to the destabilization of artificial AEs if the Larmor radius is too large and the target mode is marginally unstable. This issue is linked to the mathematical expression used to implement the FLR effects, a power series expansion for the thermal ion FLR terms and a Pade approximation for EP FLR. If the effective $k_{\perp}\rho$ is outside the range of validity of these approximations, it can lead to artificial solutions that can result in mode destabilization instead of stabilization. To avoid this issue, the simulations must be first performed without FLR effects, identifying the frequency range and growth rate of the target mode. Next, once the FLR effects are included, the Larmor radius must be increased in several steps until reaching a realistic value while tracking the growth rate of the mode.

It must be noted the correct use of FAR3d code requires a training period, particularly if the user wants to perform nonlinear simulations. The FAR3d distribution includes a user guide and several basic examples to speed up the learning process.

8.3 Bench-marking FAR3d with other codes

Bench-marking reduced models with more sophisticated codes is mandatory to demonstrate the reliability of the approximations. Towards that aim, the FAR3d code has been compared with five initial value gyrokinetic codes (EUTERPE, GEM, GTC, GYRO, ORB5), the initial value gyrokinetic-MHD code MEGA, and the perturbative eigenvalue code NOVA-K [307] for a reference DIII-D discharge 159,243 [123].

Figure 26, panels a and b, shows the destabilization of multiple RSAEs with up-sweeping frequency from $t = 770$ ms, as well as constant frequency TAEs. The instability with the largest amplitude is the TAE. Panels c indicate the simulations performed using different codes showing a reasonably good agreement with respect to the frequency of the RSAE. On the other hand, panel d indicates some deviations between the growth rate calculated by FAR3d and gyro-kinetic simulations, particularly for $n = 5$ and 6 RSAEs, that could be explained by a weaker FLR damping effect in the FAR3d simulations. Panels e to m show the good agreement of the RSAE poloidal contour calculated by FAR3d with the other models. The analysis of the TAE instability and eigenfunctions also show similar results for FAR3d and the other codes (data not shown). In summary, the output of FAR3d simulations are comparable with the analysis performed by more sophisticated models.

The analysis of MHD bursts in LHD plasma was also performed using the MEGA code [143]. Both models show important EP losses induced during the bursting phase of the instability. MEGA analysis can track the evolution of the EP slowing down distribution function along the simulation, providing useful information about the resonance evolution that cannot be obtained by gyro-fluid simulations, providing a more accurate description of the EP losses during the bursting event.

The destabilization of EPM/GAE in Heliotron J discharges was also explored using MEGA code in the linear and saturation phases [64, 308]. MEGA and FAR3d simulations show a good agreement with the experimental measurements, reproducing the same mode structure, dominant mode number and frequency range. In addition, MEGA simulations also reported the importance of performing free boundary simulations to avoid the underestimation of the linear growth rate by fixed boundary condition. This issue is partially compensated in FAR3d simulations by adapting the EP profiles in the plasma periphery, particularly the gradient of the EP density profile. The MEGA code was also applied to analyze the effect of ECCD injection on the AE stability of Heliotron J plasma, leading to qualitatively similar results compared to the FAR3d linear simulations and the experimental observations [309].

The study of AE/EPMs triggered in the EAST discharge 93,910 after Tungsten plasma contamination was first explored using the M3D-K/GTAW codes [184]. Both FAR3d and M3D-K/GTAW codes simulations obtain consistent results, reproducing the measure AE activity. The main discrepancy is the identification of the 2/3 EPM by M3D-K/GTAW simulations as the fastest growing mode, although FAR3d simulations identify the 6/3 EPM or 6/3 – 7/3 TAE as the fastest growing modes and the 2/3 – 2/4 TAE as the second fastest growing mode. Such disagreement could be caused by the lack of EP and thermal ion FLR damping effects in the simulations. Introducing FLR effects leads to a stronger reduction of the $n = 3$ growth rate as compared to $n = 2$ mode.

Simulations performed for JT60SA using the codes MEGA [296, 298] and MISHKA/CASTOR-K [297, 310–312] indicate the

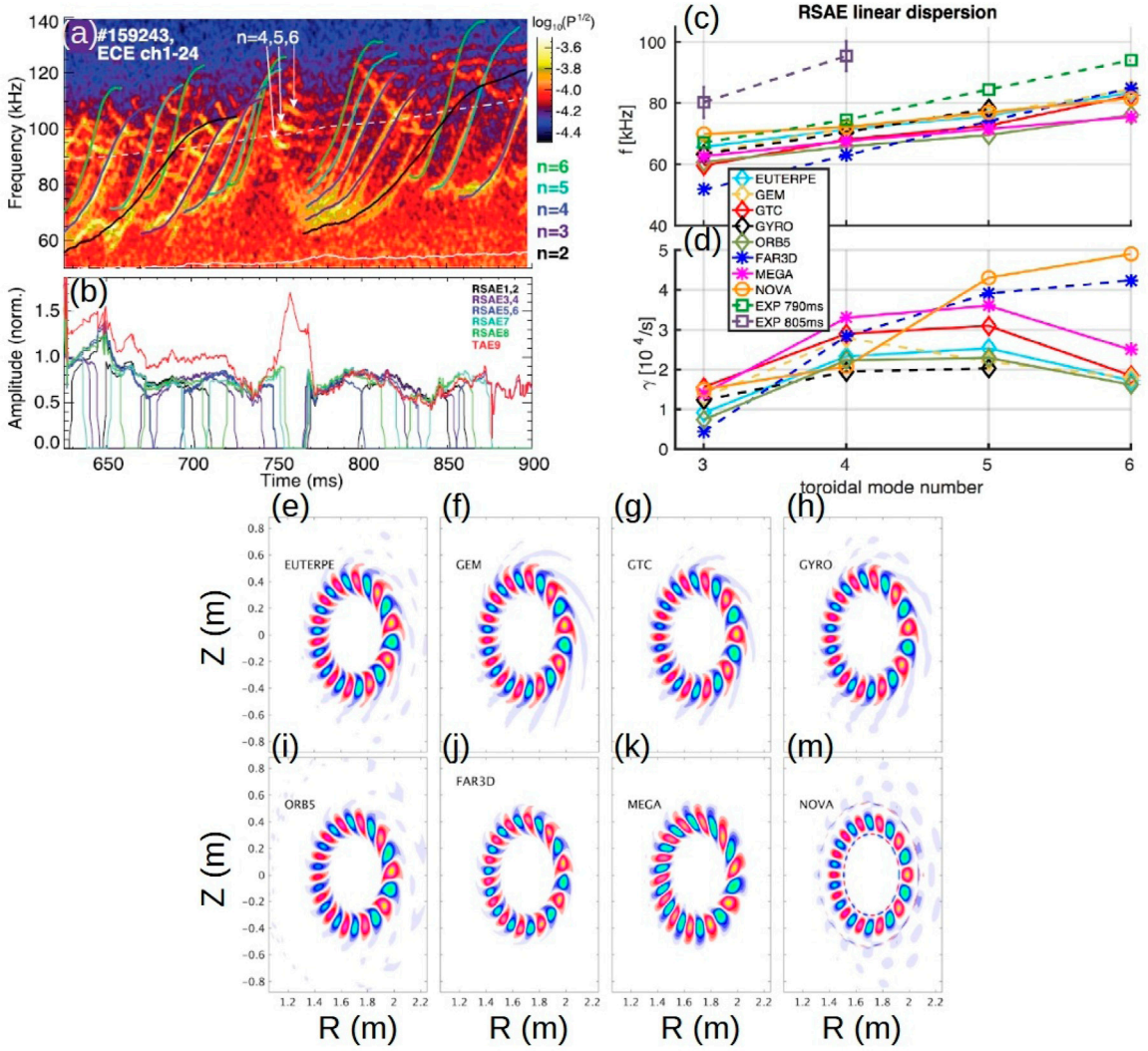

FIGURE 26
(A) ECE power spectrum with RSAE time evolution fits from an *ad hoc* model [40] and calculated GAM (solid white line) and TAE frequencies (dashed white line, in plasma frame). **(B)** Time evolution of amplitudes determined from the kick model for DIII-D shot 159,243. Figures adapted from [88]. Copyright (2017) IAEA. Linear dispersion relation calculation for RSAE in DIII-D shot 158243 at 805 m. **(C)** Real frequencies. **(D)** Growth rates. The plot markers are diamond, star, and circle for the gyrokinetic, kinetic-MHD hybrid, and perturbative eigenvalue codes, respectively. **(E–M)** $n = 4$ poloidal cross section RSAE structures. Reproduced courtesy of IAEA, IOPScience, Nuclear Fusion journal. Figures adapted from [123]. Copyright (2019) IAEA.

destabilization of AE/EPM in different operational scenarios. FAR3d simulations also identified unstable AEs in JT60SA ITER-like inductive scenario.

Simulations dedicated to forecast the AE stability in ITER operation scenarios indicate TAEs of toroidal mode families between $n = 10$ to 20 can be unstable [313–317]. FAR3d simulations also indicate the destabilization of $n = 10$ to 20 AEs in hybrid, reverse shear and steady state ITER configurations.

9 Conclusions

The gyro-fluid code FAR3d is a computationally efficient tool to analyze the AE/EPM stability in nuclear fusion devices, filling the gap between the short term analysis required during experimental campaigns and long term studies complementing more sophisticated gyrokinetic and kinetic-MHD hybrid codes.

FAR3d has been applied to reproduce the AE/EPM activity in tokamaks such as JET, DIII-D and EAST as well as stellarators such as LHD, TJ-II and Heliotron J, showing reasonable similarities between simulations and experimental observations by identifying the same radial location, dominant mode numbers, frequency range and eigenfunction structure. In particular, the stability of TAEs and EICs in LHD, HAEs and GAEs in TJ-II, TAEs and RSAEs in DIII-D, TAEs and EPMs in EAST, GAEs and EPMs in Heliotron J and TAEs and fish-bones in JET has been analyzed.

The rapid turn-around time of FAR3d simulations allow one to perform parametric studies dedicated to the analysis of the linear and non-linear stability of AE/EPM for different device configurations. This opens up the possibility optimization studies

that can identify configurations with reduced AE/EPM activity. Towards that goal, FAR3d analysis can explore optimal configurations with respect to the thermal plasma properties, magnetic field geometry, the effect of external actuators and the impact of multiple EP populations. Such improved operational scenarios were validated in dedicated experiments in devices as LHD, TJ-II, Heliotron J, DIII-D and EAST.

The combination of experimental observations and FAR3d optimization studies provided valuable information in the search for optimal operational conditions to stabilize EICs in LHD with respect to the thermal plasma configuration, the effect of AEs on ITB for EAST discharges, as well as the impact of the magnetic field topology on the AE stability for reverse shear and negative triangularity discharges in DIII-D. In addition, the AE stability in quasi-poloidal and quasi-axysymmetric stellarators has been explored.

The effect of external actuators on the AE/EPM activity in LHD, Heliotron J and DIII-D plasmas has also been analyzed. FAR3d can reproduce and account for the effects of the application of ECCD, the induction of currents by the NBI or the injection of ECH leading to the stabilization or further destabilization of AE/EPMs in different device configurations, providing useful information to develop reliable techniques dedicated to improve the performance of future nuclear fusion reactors.

The analysis of multiple EP population effects in LHD and JET discharges provides a first approach to the AE/EPM stability issues in reactor relevant plasmas, indicating its essential role in the analysis of the EP transport. Linear and nonlinear feedback between different EP population must be included in the studies for a correct analysis of experimental observations. In addition, multiple EP effects in future devices such as ITER and CFETR are explored.

The analysis of the AE/EPM nonlinear saturation phase is required to reproduce the experimental observation, in particular the induced EP transport, profile flattening, generation of zonal structures and the energy cascades between different toroidal or helical families. In addition, nonlinear simulations can be used to analyze the bursting phenomena observed in multiple fusion devices, linked to an important deterioration of the operational performance and large EP losses. FAR3d analysis suggests EIC and MHD bursting activity in LHD as well as burst events in DIII-D could be caused by resonance overlapping effects, leading to a transition from the soft MHD limit (local plasma relaxation) to the hard MHD limit (global plasma relaxation), inducing large EP losses due to an abrupt increase of the EP transport. On top of that, the shear flows caused by AE/EPM instabilities may have an important role on the thermal plasma confinement and plasma turbulent level as it is observed in LHD, JET, DIII-D and EAST discharges and FAR3d simulations.

FAR3d can also provide a first approach of the AE/EPM linear and nonlinear stability for future devices as ITER, CFETR and JT60SA. Forecasting resonances that may induce the destabilization of AE/EPM will be helpful to constrain the parametric space leading to operational scenarios with an efficient plasma heating and optimal performance. In addition, future analysis will be dedicated to explore how external actuators may improve the AE/EPM stability in unfavorable configurations, for example, by the injection of ECCD, ECH or due to the generation of NBCD. Also, optimization trends with respect to the thermal plasma parameters and external actuators operational regime will be explored. On top of that, the saturation phase of AE/EPM will be analyzed to predict the EP transport induced and the generation of zonal structures.

10 Prospects and future plans

This section is dedicated to show ongoing and future research topics of the FAR3d project. Also, future upgrades of the code are discussed.

10.1 Ongoing research lines

The main topics of present FAR3d research lines are dedicated to studies of the EP transport and the generation of zonal structures during the AE/EPM nonlinear saturation phase. A set of dedicated experiments were performed in LHD device to measure shear flows using charge exchange spectroscopy, comparing the radial electric field and thermal plasma poloidal rotation with the output of nonlinear FAR3d simulations [274]. The generation of shear flows by TAE and fish-bones is also explored in the DT JET discharge 99,896. Demonstrating the generation of shear flows during the saturation phase of AE/EPM and their potential effect on the thermal plasma confinement is a key topic for ITER and future fusion reactors [318]. The instability-driven EP transport rates are also an important consideration for future fusion reactors, and can be inferred directly from profile flattening effects.

The study of the JET DT plasma is extended to analyze the EP populations leading to the destabilization of TAEs and fish-bones in the discharge 99,896. In addition, multiple EP nonlinear simulations including ICRH EP + alpha particles are performed to investigate the alpha particle losses induced by fish-bone. Understanding multiple EP effects and the nonlinear destabilization of the alpha particle population by NBI and ICRH EP populations is essential to forecast correctly the alpha particle confinement in ITER and future fusion reactors [273].

Another research line is dedicated to analyze the effect of the EPs on the linear and nonlinear stability of kink, interchange and tearing modes. In particular, such stability trends are analyzed in multiple EP plasma including NBI EP and alpha particles. The analysis of cross stabilizing/destabilizing effects between thermal plasma instabilities and AE/EPM are important to predict the confinement of both, thermal plasma and alpha particles, in ITER and fusion reactors [319].

The saturation phase and extinction of EPMs in tokamak and stellarator can be explored doing FAR3d nonlinear simulations. In particular, the fish-bones and EIC frequency down-sweeping observed in JET and LHD plasma have been analyzed, as well as the destabilization of kink and interchange modes, respectively, after fish-bones and EIC stabilize. This analysis is important to evaluate how the EP losses affect the stability of EPMs and thermal plasma instabilities in fusion devices.

A set of experiments in the LHD device were performed during 2021 and 2022 campaigns dedicated to identify operational scenarios with improved performance by minimizing, at the same time, the

activity of AEs and interchange modes. On that aim, discharges with different heating patterns, magnetic field configurations and thermal plasma parameters are tested, measuring the AE and interchange mode activity with respect to the NBCD, thermal plasma density and NBI operational regime. The optimization trends obtained in the experiments were analyzed and reproduced by linear simulations performed using the FAR3d code. Exploring operational scenarios with reduced AE/interchange mode activity is important to optimize the LHD device performance, improving the thermal plasma confinement and the plasma heating efficiency [320].

The tracer code TAPAS has been coupled with FAR3d to study the EP transport generated in DIII-D, JET and ITER plasmas using self-consistent AE/EPM perturbations calculated by FAR3d non linear simulations. The TAPAS/FAR3d model will be validated by comparing simulation results and EP losses measured in DIII-D and JET discharges. The next step is applying the model to forecast the alpha particle transport in different operational scenarios of ITER [321].

10.2 Future research lines

The analysis of the linear and nonlinear stability of AEs measured in TJ-II plasma using HIBP will be one of the next research lines for the FAR3d project. HIBP is a diagnostic that provides unique information of the electrostatic potential perturbation induced by AEs. Such data can be directly compared with the FAR3d output, providing an excellent framework to test the accuracy of the simulations and analyze in detail the saturation phase of AEs [82, 322–324].

The analysis of zonal structures generation during the AE/EPM saturation phase will be extended to TJ-II, Heliotron J and DIII-D devices by performing dedicated experiments that will be compared to nonlinear FAR3d simulations.

A set of experiments were performed in 2024 LHD campaign dedicated to analyze the bursting activity induced in discharges combining tangential and perpendicular NBI injection with ICRH. Multiple EP linear simulations will be performed to analyze the AEs observed in the discharges, and how multiple EP effects can modify the AE stability in LHD plasma.

Parametric studies will be performed to analyze the EP transport in the DIII-D plasma using the nonlinear version of FAR3d. The aim of the study is reproducing the EP losses measured in DIII-D discharges as the NBI power increases. In particular, the abrupt increase of the EP transport during bursting events will be main target of the study, providing support to the soft to hard transition caused by the overlapping of multiple resonances.

The linear stability of AEs in ITER plasma configuration including RMPs will be analyzed. Forecasting the AE stability in ITER configurations with and without RMPs is an essential topic to understand the effect of the RMPs on plasma heating efficiency of ITER plasma.

A set of linear and nonlinear studies will be dedicated to study the AE stability in different KSTAR configurations. The methods developed by KSTAR team to improve the AE stability and the plasma heating efficiency are important to improve the performance of ITER operation scenarios.

The linear and nonlinear stability of AE/EPM in different configurations of JT60SA, ITER and DEMO will be explored, emphasizing the analysis of the alpha particle transport and zonal structure generation in multiple EP plasma. In addition, the possibility of soft to hard transitions in reactor relevant plasma and the consequences on the device performance will be studied. Another part of the analysis will be dedicated to predict the effects of external actuators to reduce or avoid the AE/EPM activity.

The linear stability of AEs and thermal plasma instabilities with respect to the EP population at the plasma periphery of tokamak plasma will be explored. Keeping aware of the FAR3d model limitations for providing a correct description of modes destabilized at the pedestal, the analysis will be limited to identify stability trends. That means, FAR3d cannot provide the stability threshold of peripheral modes but it is possible to explore configurations showing reduced mode growth rates for optimization studies.

Another research line consists in analyzing the linear and nonlinear AE/EPM stability in new designs of optimized stellarators. This information may be useful to select the magnetic configurations with optimal plasma heating efficiency with respect to an improved AE/EPM stability.

FAR3d will be added to integrated modelling frameworks dedicated to the design of fusion reactors. FAR3d may provide information of the NBI EP, ICRH EP and alpha particle destabilizing effects on reactor relevant plasma configurations, EP density transport fluxes, identifying the parametric range with optimal plasma heating. Integrated modeling workflows such as IMAS (proposed) [312] and FREDA (ongoing) [325] are examples of FAR3d implementations dedicated to explore AE/EPM stability and EP transport [328, 329].

Future studies will be dedicated to compare the FAR3d and GENE code simulations, analyzing the AE/EPM stability of different devices.

Finally, AI applications based on FAR3d nonlinear simulations will be developed to predict the EP transport in different fusion devices.

10.3 Next code updates

A major updated version of the FAR3d distribution, the open source version of the code, will be released during 2024. The FAR3d 2.0 distribution will include the linear and nonlinear versions of the code allowing simulations with up to 3 EP populations at the same time. This distribution will also include a new add-on dedicated module to transform EFIT data to the FAR3d equilibrium input.

The implementation of GPU parallelization is ongoing. An early version including GPU parallelization is being tested.

Different methods to introduce neoclassical effects into the model are under review. Updating the code to analyze NTMs is one of the priorities of the core development team.

Introduce the perturbation of the magnetic field along the magnetic field line is another of the developing team priorities, required to model ideal internal kinks, EPMs and low frequency AEs in tokamak plasmas.

The development of the four moments version of the code continues, with the goal of resolving issues identified in the version with moments of the EP energy and EP parallel heat flux, as well as the version with parallel ad perpendicular components of the pressure tensor.

A new equation describing the evolution of the thermal plasma density perturbation will be included in the nonlinear version of the code. This upgrade will enable the analysis of ion temperature gradient

instabilities (ITGs) during the saturation phase of AE/EPM, providing further information of the thermal plasma turbulence and anomalous transport and their coupling with the AE turbulence. ITGs are connected to the grad *B* drift, proportional to the thermal ion's kinetic energy, thus thermal ions with larger energy show a larger drift. If the thermal ion temperature gradient is aligned with a magnetic field gradient, thermal ions with higher energy will drift faster. If there is a perturbation in the temperature gradient, drift velocitie differences create charge separation and, consequently, an electric field. The electric field induces a drift that increases the perturbation's amplitude. Including an equation for the thermal ion density evolution allows tracking the stability of ITGs because the model will include both, thermal plasma pressure and the thermal ion density, that is to say, the evolution of the thermal ion temperature. Reproducing the effect of the charge separation will require adding some new terms in the vorticity equation. The implementation will follow the theory developed in the Ref. [326]. It should be noted that combining the very large number of modes needed to do ITG turbulence + AE turbulence may be computationally challenging.

Author contributions

JV: Conceptualization, Data curation, Formal Analysis, Funding acquisition, Investigation, Methodology, Project administration, Resources, Software, Supervision, Validation, Visualization, Writing–original draft, Writing–review and editing. DS: Conceptualization, Data curation, Formal Analysis, Funding acquisition, Investigation, Methodology, Project administration, Resources, Software, Supervision, Validation, Visualization, Writing–original draft, Writing–review and editing. LG: Conceptualization, Data curation, Formal Analysis, Funding acquisition, Investigation, Methodology, Project administration, Resources, Software, Supervision, Validation, Visualization, Writing–original draft, Writing–review and editing. YG: Conceptualization, Data curation, Formal Analysis, Funding acquisition, Investigation, Methodology, Project administration, Resources, Software, Supervision, Validation, Visualization, Writing–original draft, Writing–review and editing. JO: Conceptualization, Data curation, Formal Analysis, Funding acquisition, Investigation, Methodology, Project administration, Resources, Software, Supervision, Validation, Visualization, Writing–original draft, Writing–review and editing.

FAR3d contributors

D. C. Pace, M. Murakami, M. A. Van Zeeland, X. Du (General Atomics, P.O. Box 85608, San Diego, California 92186-5608, United States), J. Huang, C. Jiale, X. H. Wang, Y. Sun (Institute of Plasma Physics, Chinese Academy of Science, Hefei, China), S. Ohdachi, K. Y. Watanabe, Y. Todo, K. Nagaoka, A. Azegami, K. Ida, K. Tanaka, K. Ogawa, M. Osakabe, P. Adulsiriswad, Y. Takemura, M. Yoshinuma, T. Tokuzawa, M. Idouakass (National Institute for Fusion Science, National Institute of Natural Science, Toki, 509-5292, Japan), R. Seki (SOKENDAI, Department of Fusion Science, Toki/Gifu and National Institute for Fusion Science, National Institute of Natural Science), S. Taimourzadeh (University of California, Irvine, CA, 92697, United States of America), W. A. Cooper (Ecole Polytechnique de Lausanne (EPFL), Centre de Recherches en Physique des Plasma (CRPP), CH-1015 Lausanne, Switzerland), A. Cappa, E. Ascasíbar, J. M. García-Regaña, M. Ochando, C. Hidalgo, P. Pons-Villalonga, F. Papousek, B. Ph. Van Milligen, U. Losada (Laboratorio Nacional de Fusion CIEMAT, Madrid, Spain), S. Yamamoto, K. Shinohara, H. Yang, J. Shiraishi, M. Honda, Y. Kamada, N. Aiba (National Institutes for Quantum and Radiological Science and Technology, Naka, Ibaraki 311-0193, Japan), K. Nagasaki, S. Kobayashi, (Institute of Advanced Energy, Kyoto University, Uji, Japan), A. Melnikov, L. G. Eliseev (National Research Centre "Kurchatov Institute", Moscow, Russian Federation), Y. Suzuki (Graduate School of Advanced Science and Engineering, Hiroshima University, 1-4-1 Kagamiyama, Higashi-Hiroshima 739-8527, Japan), B. Breizman, F. L. Waelbroeck (Institute for Fusion Studies, Department of Physics, University of Texas at Austin, Austin, Texas 78712, United States), Y. Zou, (University of Science and Technology of China, Hefei, China), Y. Zou, (Southwestern Institute of Physics, Chengdu 610041, China), A. Wingen, D. del-Castillo-Negrete (Oak Ridge National Laboratory, Oak Ridge, Tennessee 37831-8071, US), D. Zarzoso, H. Betar (Aix-Marseille Université, CNRS, Centrale Marseille, M2P2 UMR 7340 Marseille, France), R. Sanchez, V. Tribaldos, J. M. Reynolds-Barredo, L. Herrera (Universidad Carlos III de Madrid, 28911 Leganes, Madrid, Spain), A. Bader (Type One Energy, 40 New York Ave. 200, Oak Ridge, TN 37830), D. Monseev (Max-Planck-Institut für Plasmaphysik, Wendelsteinstr. 1, Greifswald 17,491, Germany), J. Garcia, S. Mazzi (CEA, IRFM, F-13108 Saint Paul-lez-Durance, France), Y. Kazakov (Laboratory for Plasma Physics, LPP-ERM/KMS, TEC Partner, 1000 Brussels, Belgium), S. Sharapov (CCFE, Culham Science Centre, Oxfordshire OX14 3DB, United Kingdom), Z. Stancar (United Kingdom Atomic Energy Authority, Culham Science Centre, Abingdon, United Kingdom), M. Baruzzo (Consorzio RFX, Corso Stati Uniti 4, Padova, Italy), J. Ongena (Plasma Physics Laboratory – Royal Military Academy, Renaissancelaan 30, 1000 Brussels, Belgium), M. Poradzinski (Institute of Plasma Physics and Laser Microfusion, Hery str. 23, 01-497, Warsaw, Poland), N. Gorelenkov, F. Poli, J. Breslau, M. Podesta (Princeton Plasma Physics Laboratory, Princeton University, Princeton, NJ, 08543, United States), A. Di Siena, F. Jenko (Max-Planck-Institut für Plasmaphysik, D-85748 Garching, Germany), I. Holod (Lawrence Livermore National Laboratory, Livermore, CA 94550, United States), A. Melnikov (National Research Nuclear University MEPhI, Moscow, Russia 115409), A. Melnikov (Moscow Institute of Physics and Technology, Moscow Region, Dolgoprudny, Russia 141700), H. Betar (Renaissance Fusion, 38600 Fontaine, France).

Funding

The author(s) declare that financial support was received for the research, authorship, and/or publication of this article. This work was supported by the Comunidad de Madrid under the project 2019-T1/AMB-13648, US DOE under grant DE-FG02-04ER54742, U.S. Department of Energy Office Contract DE-AC05-00OR22725 with UT-Battelle LLC and NIFS07KLPH004.

Acknowledgments

The authors would like to thanks LHD, Heliotron J, TJ-II, CFQS, DIII-D, JET and EAST technical staff for their contributions in the operation and maintenance of devices. The authors want to thanks the collaboration with S. A. Lazerson, A. Bierwage, V. Chan, W. W. Heidbrink, R. Fitzpatrick, S. M. Mahajan, D. Hatch.

Conflict of interest

FAR3d contributor XD was employed by the company General Atomics. FAR3d contributor AB was employed by the company Type One Energy. FAR3d contributor HB was employed by the company Renaissance Fusion.

The remaining authors declare that the research was conducted in the absence of any commercial or financial relationships that could be construed as a potential conflict of interest.

Publisher's note

Supplementary material

The Supplementary Material for this article can be found online at: https://www.frontiersin.org/articles/10.3389/fphy.2024.1422411/full#supplementary-material

References

1. Toi K, Ohdachi S, Yamamoto S, Nakajima N, Sakakibara S, Watanabe K, et al. MHD instabilities and their effects on plasma confinement in Large Helical Device plasmas. *Nucl Fusion* (2004) 44:217–25. doi:10.1088/0029-5515/44/2/001

2. Yamamoto S, Toi K, Ohdachi S, Nakajima N, Sakakibara S, Nührenberg C, et al. Experimental studies of energetic-ion-driven MHD instabilities in Large Helical Device plasmas. *Nucl Fusion* (2005) 45:326–36. doi:10.1088/0029-5515/45/5/003

3. Phillips CK, Fredrickson E, Hammett G, Hosea J, McGuire K, Stevens J, et al. ICRF Heating on TFTR. *AIP Conf Proc* (1992) 244:89–95. doi:10.1063/1.41652

4. Wong KL, Fonck R, Paul S, Roberts D, Fredrickson E, Nazikian R, et al. Excitation of toroidal Alfvén eigenmodes in TFTR. *Phys Rev Lett* (1991) 66:1874–7. doi:10.1103/PhysRevLett.66.1874

5. Sharapov SE, Borba D, Fasoli A, Kerner W, Eriksson LG, Heeter R, et al. Stability of alpha particle driven Alfvén eigenmodes in high performance JET DT plasmas. *Nucl Fusion* (1999) 39:373–88. doi:10.1088/0029-5515/39/3/307

6. Heidbrink WW, Strait E, Doyle E, Sager G, Snider R. An investigation of beam driven Alfvén instabilities in the DIII-D tokamak. *Nucl Fusion* (1992) 31:1635–48. doi:10.1088/0029-5515/31/9/002

7. Duong HH, Heidbrink W, Strait E, Petrie T, Lee R, Moyer R, et al. Loss of energetic beam ions during TAE instabilities. *Nucl Fusion* (1993) 33:749–65. doi:10.1088/0029-5515/33/5/i06

8. Kusama Y, Kramer G, Kimura H, Saigusa M, Ozeki T, Tobita K, et al. Characteristics of Alfvén eigenmodes, burst modes and chirping modes in the Alfvén frequency range driven by negative ion based neutral beam injection in JT-60U. *Nucl Fusion* (1999) 39:1837–43. doi:10.1088/0029-5515/39/11y/324

9. Shinohara K, Takechi M, Ishikawa M, Kusama Y, Morioka A, Oyama N, et al. Recent progress of Alfvén eigenmode experiments using N-NB in JT-60U tokamak. *Nucl Fusion* (2002) 42:942–8. doi:10.1088/0029-5515/42/8/302

10. Ross DW, Chen GL, Mahajan SM. Kinetic description of Alfvén wave heating. *Phys Fluids* (1982) 25:652–67. doi:10.1063/1.863789

11. Mahajan SM, Ross DW, Chen GL. Discrete Alfvén eigenmode spectrum in magnetohydrodynamics. *Phys Fluids* (1983) 26:2195–9. doi:10.1063/1.864404

12. Mahajan SM. Kinetic theory of shear Alfvén waves. *Phys Fluids* (1984) 27:2238–47. doi:10.1063/1.864878

13. Evans TE, Valanju PM, Benesch JF, Bengtson RD, Li YM, Mahajan SM, et al. Direct observation of the structure of global Alfvén eigenmodes in a tokamak plasma. *Phys Rev Lett* (1984) 53:1743–6. doi:10.1103/physrevlett.53.1743

14. Li YM, Mahajan SM, Ross DW. Destabilization of global Alfvén eigenmodes and kinetic Alfvén waves by alpha particles in a tokamak plasma. *Phys Fluids* (1987) 30:1466–84. doi:10.1063/1.866260

15. Coppi B, Migliuolo S, Pegoraro F, Porcelli F. Global modes and high-energy particles in ignited plasmas. *Fluids B* (1990) 2:927–43. doi:10.1063/1.859240

16. Rosenbluth MN, Tsai ST, Van Dam JW, Engquist MG. Energetic particle stabilization of ballooning modes in tokamaks. *Phys Rev Lett* (1983) 51:1967–70. doi:10.1103/physrevlett.51.1967

17. White RB, Bussac M, Romanelli F. High-beta, sawtooth-free tokamak operation using energetic trapped particles. *Phys Rev Lett* (1989) 62:539–42. doi:10.1103/PhysRevLett.62.539

18. Porcelli F. Fast particle stabilisation. *Plasma Phys Control Fusion* (1991) 33:1601–20. doi:10.1088/0741-3335/33/13/009

19. Chen L, White RB, Rosenbluth MN. Excitation of internal kink modes by trapped energetic beam ions. *Phys Rev Lett* (1984) 52:1122–5. doi:10.1103/physrevlett.52.1122

20. Coppi B, Porcelli F. Theoretical model of fishbone oscillations in magnetically confined plasmas. *Phys Rev Lett* (1986) 57:2272–5. doi:10.1103/physrevlett.57.2272

21. Biglari H, Chen L. Unified theory of resonant excitation of kinetic ballooning modes by energetic ions and alpha particles in tokamaks. *Phys Rev Lett* (1991) 67:3681–4. doi:10.1103/physrevlett.67.3681

22. Garcia-Munoz M, Classen I, Geiger B, Heidbrink W, Van Zeeland M, Äkäslompolo S, et al. Fast-ion transport induced by Alfvén eigenmodes in the ASDEX Upgrade tokamak. *Nucl Fusion* (2011) 51:103013. doi:10.1088/0029-5515/51/10/103013

23. Darrow DS, Zweben S, Chang Z, Cheng C, Diesso M, Fredrickson E, et al. Observations of neutral beam and ICRF tail ion losses due to Alfven modes in TFTR. *Nucl Fusion* (1997) 37:939–54. doi:10.1088/0029-5515/37/7/i03

24. Marashek M, Günter S, Kass T, Scott B, Zohm H, ASDEX Upgrade Team. Observation of toroidicity-induced alfvén eigenmodes in ohmically heated plasmas by drift wave excitation. *Phys Rev Lett* (1997) 79:4186–9. doi:10.1103/physrevlett.79.4186

25. Melnikov AV, Markovic T, Eliseev LG, Adámek J, Aftanas M, Bilkova P, et al. Quasicoherent modes on the COMPASS tokamak. *Plasma Phys Control Fusion* (2015) 57:065006. doi:10.1088/0741-3335/57/6/065006

26. Markovic T, Markovic´ A, Melnikov J, Seidl L, Eliseev J, Havlicek A, et al. *44th European Physical Society Conference on Plasma Physics*. Queen's University: Belfast, North. Ireland (2017) 41:P5.140.

27. Valovič M, Lloyd B, McClements K, Warrick C, Fielding S, Morris A, et al. Quasi-stationary high plasmas and fast particle instabilities in the COMPASS-D tokamak with ECRH and LHCD. *Nucl Fusion* (2000) 40:1569–73. doi:10.1088/0029-5515/40/9/101

28. Wong KL, Chu M, Luce T, Petty C, Politzer P, Prater R, et al. Internal kink instability during off-axis electron cyclotron current drive in the DIII-D tokamak. *Phys Rev Lett* (2000) 85:996–9. doi:10.1103/PhysRevLett.85.996

29. Deng CB, Brower DL, Breizman BN, Spong DA, Almagri AF, Anderson DT, et al. Energetic-electron-driven instability in the helically symmetric experiment. *Phys Rev Lett* (2009) 103:025003. doi:10.1103/PhysRevLett.103.025003

30. Isobe M, Toi K, Yoshimura Y, Shimizu A, Akiyama T, Ida K, et al. Energetic-particle modes driven by suprathermal electrons produced by off-axis second harmonic ECRH in compact helical system (CHS). *Nucl Fusion* (2010) 50:084007. doi:10.1088/0029-5515/50/8/084007

31. Melnikov AV, Eliseev LG, Ochando MA, Nagaoka K, Ascasibar E, Cappa A, et al. A quasi-coherent electrostatic mode in ECRH plasmas on TJ-II. *Plasma Fusion Res* (2011) 6:2402030. doi:10.1585/pfr.6.2402030

32. Heidbrink WW. Basic physics of Alfvén instabilities driven by energetic particles in toroidally confined plasmas. *Plasma Phys* (2008) 15:055501. doi:10.1063/1.2838239

33. Todo Y. Introduction to the interaction between energetic particles and Alfven eigenmodes in toroidal plasmas. *Rev Mod Plasma Phys* (2019) 3:1. doi:10.1007/s41614-018-0022-9

34. Weller A, Spong DA, Jaenicke R, Lazaros A, Penningsfeld FP, Sattler S. Neutral beam driven global Alfvén eigenmodes in the Wendelstein W7-AS stellarator. *Phys Rev Lett* (1994) 72:1220–3. doi:10.1103/physrevlett.72.1220

35. Van Zeeland MA, Kramer GJ, Austin ME, Boivin RL, Heidbrink WW, Makowski MA, et al. Radial structure of Alfvén eigenmodes in the DIII-D tokamak through electron-cyclotron-emission measurements. *Phys Rev Lett* (2006) 97:135001. doi:10.1103/PhysRevLett.97.135001

36. Nazikian R, Gorelenkov NN, Alper B, Berk HL, Borba D, Budny RV, et al. Excitation of Alfvén eigenmodes by low energy beam ions in the DIII-D and JET tokamaks. *Phys Plasmas* (2008) 15:056107. doi:10.1063/1.2839286

37. Van Zeeland MA, Heidbrink W, Nazikian R, Austin M, Cheng C, Chu M, et al. Measurements, modelling and electron cyclotron heating modification of Alfvén eigenmode activity in DIII-D. *Nucl Fusion* (2009) 49:065003. doi:10.1088/0029-5515/49/6/065003

38. Kieras CE, Tataronis JA. The shear Alfvén continuous spectrum of axisymmetric toroidal equilibria in the large aspect ratio limit. *J Plasma Phys* (1982) 28:395–414. doi:10.1017/s0022377800000386

39. Wang Z, Lin Z, Deng W, Holod I, Heidbrink WW, Xiao Y, et al. Properties of toroidal Alfvén eigenmode in DIII-D plasma. *Phys Plasmas* (2015) 22:022509. doi:10.1063/1.4908274

40. Van Zeeland M, Heidbrink W, Sharapov S, Spong D, Cappa A, Chen X, et al. Electron cyclotron heating can drastically alter reversed shear Alfvén eigenmode activity in DIII-D through finite pressure effects. *Nucl Fusion* (2016) 56:112007. doi:10.1088/0029-5515/56/11/112007

41. Turnbull AD, Strait EJ, Heidbrink WW, Chu MS, Duong HH, Greene JM, et al. Global alfvén modes: theory and experiment*. *Phys Fluids B* (1993) 5:2546–53. doi:10.1063/1.860742

42. Deng W, Lin Z, Holod I, Wang Z, Xiao Y, Zhang H. Linear properties of reversed shear Alfvén eigenmodes in the DIII-D tokamak. *Nucl Fusion* (2012) 52:043006. doi:10.1088/0029-5515/52/4/043006

43. Kimura H, Kusama Y, Saigusa M, Kramer G, Tobita K, Nemoto M, et al. Alfvén eigenmode and energetic particle research in JT-60U. *Nucl Fusion* (1998) 38:1303–14. doi:10.1088/0029-5515/38/9/304

44. Betti R, Freidberg JP. Stability of Alfvén gap modes in burning plasmas. *Phys Fluids B* (1992) 4:1465–74. doi:10.1063/1.860057

45. Kramer GJ, Saigusa M, Ozeki T, Kusama Y, Kimura H, Oikawa T, et al. Noncircular triangularity and ellipticity-induced alfvén eigenmodes observed in jt-60u. *Phys Rev Lett* (1998) 80:2594–7. doi:10.1103/physrevlett.80.2594

46. Betti R, Freidberg JP. Ellipticity induced Alfvén eigenmodes. *Phys Fluids B* (1991) 3:1865–70. doi:10.1063/1.859655

47. Bass EM, Waltz RE. Gyrokinetic simulation of global and local Alfvén eigenmodes driven by energetic particles in a DIII-D discharge. *Phys Plasmas* (2013) 20:012508. doi:10.1063/1.4773177

48. Yamamoto S, Toi K, Nakajima N, Ohdachi S, Sakakibara S, Watanabe KY, et al. Observation of helicity-induced Alfvén eigenmodes in large-helical-device plasmas heated by neutral-beam injection. *Phys Rev Lett* (2003) 91:245001. doi:10.1103/PhysRevLett.91.245001

49. Chen L. Theory of magnetohydrodynamic instabilities excited by energetic particles in tokamaks*. *Phys Plasmas* (1994) 1:1519–1522. doi:10.1063/1.870702

50. Ido T, Osakabe M, Shimizu A, Watari T, Nishiura M, Toi K, et al. Identification of the energetic-particle driven GAM in the LHD. *Nucl Fusion* (2015) 55:083024. doi:10.1088/0029-5515/55/8/083024

51. Wang H, Todo Y, Ido T, Osakabe M. Simulation study of high-frequency energetic particle driven geodesic acoustic mode. *Phys Plasmas* (2015) 22:092507. doi:10.1063/1.4930130

52. Wang H, Todo Y, Ido T, Suzuki Y. Chirping and sudden excitation of energetic-particle-driven geodesic acoustic modes in a large helical device experiment. *Phys Rev Lett* (2018) 120:175001. doi:10.1103/PhysRevLett.120.175001

53. Ogawa K, Isobe M, Toi K, Shimizu A, Spong D, Osakabe M, et al. A study on the TAE-induced fast-ion loss process in LHD. *Nucl Fusion* (2013) 53:053012. doi:10.1088/0029-5515/53/5/053012

54. Murakami M, Park J, Giruzzi G, Garcia J, Bonoli P, Budny R, et al. Integrated modelling of steady-state scenarios and heating and current drive mixes for ITER. *Nucl Fusion* (2011) 51:103006. doi:10.1088/0029-5515/51/10/103006

55. Pengxiang C, Wu B, Wang J, Li Y, Wang X, Xu H, et al. The influence of neutral beam injection on the heating and current drive with electron cyclotron wave on EAST. *Plasma Sci Technol* (2016) 18:1064–8. doi:10.1088/1009-0630/18/11/02

56. Murakami M, Greenfield C, Wade M, Luce T, Ferron J, John HS, et al. 100% noninductive operation at high beta using off-axis ECCD in DIII-D. *Nucl Fusion* (2005) 45:1419–26. doi:10.1088/0029-5515/45/11/024

57. Takenaga H, JT-60 Team. Overview of JT-60U results for the development of a steady-state advanced tokamak scenario. *Nucl Fusion* (2007) 47:S563–78. doi:10.1088/0029-5515/47/10/s06

58. Voitsekhovitch I, Alper B, Brix M, Budny R, Buratti P, Challis C, et al. Non-inductive current drive and transport in high β_N plasmas in JET. *Nucl Fusion* (2009) 49:055026. doi:10.1088/0029-5515/49/5/055026

59. Chapman IT, La Haye R, Buttery R, Heidbrink W, Jackson G, Muscatello C, et al. Sawtooth control using electron cyclotron current drive in ITER demonstration plasmas in DIII-D. *Nucl Fusion* (2012) 52:063006. doi:10.1088/0029-5515/52/6/063006

60. Murakami M, Park J, Petty C, Luce T, Heidbrink W, Osborne T, et al. Off-axis neutral beam current drive for advanced scenario development in DIII-D. *Nucl Fusion* (2009) 49:065031. doi:10.1088/0029-5515/49/6/065031

61. Isayama A, Matsunaga G, Kobayashi T, Moriyama S, Oyama N, Sakamoto Y, et al. Neoclassical tearing mode control using electron cyclotron current drive and magnetic island evolution in JT-60U. *Nucl Fusion* (2009) 49:055006. doi:10.1088/0029-5515/49/5/055006

62. Oikawa T, Ushigusa K, Forest C, Nemoto M, Naito O, Kusama Y, et al. Heating and non-inductive current drive by negative ion based NBI in JT-60U. *Nucl Fusion* (2000) 40:435–43. doi:10.1088/0029-5515/40/3y/301

63. Sharapov SE, Garcia-Munoz M, Van Zeeland MA, Bobkov B, Classen IGJ, Ferreira J, et al. The effects of electron cyclotron heating and current drive on toroidal Alfvén eigenmodes in tokamak plasmas. *Plasma Phys Control Fusion* (2018) 60:014026. doi:10.1088/1361-6587/aa90ee

64. Adulsiriswad P, Todo Y, Yamamoto S, Kado S, Kobayashi S, Ohshima S, et al. Magnetohydrodynamic hybrid simulation of Alfvén eigenmodes in Heliotron J, a low shear helical axis stellarator/heliotron. *Nucl Fusion* (2020) 60:096005. doi:10.1088/1741-4326/ab9c4b

65. Silva Rosa PR, Giruzzi G. RF current drive by electron cyclotron waves in the presence of magnetic islands. *Plasma Phys Control Fusion* (2000) 42:755–69. doi:10.1088/0741-3335/42/7/302

66. Prater R. Heating and current drive by electron cyclotron waves. *Phys Plasma* (2004) 11:2349–76. doi:10.1063/1.1690762

67. Sauter O, Henderson MA, Hofmann F, Goodman T, Alberti S, Angioni C, et al. Steady-state fully noninductive current driven by electron cyclotron waves in a magnetically confined plasma. *Phys Rev Lett* (2000) 84:3322–5. doi:10.1103/PhysRevLett.84.3322

68. Suzuki T, Ide S, Hamamatsu K, Isayama A, Fujita T, Petty CC, et al. Heating and current drive by electron cyclotron waves in JT-60U. *Nucl Fusion* (2004) 44:699–708. doi:10.1088/0029-5515/44/7/002

69. Motojima G, Nagasaki K, Nosaku M, Okada H, Watanabe K, Mizuuchi T, et al. Control of non-inductive current in Heliotron J*. *Nucl Fusion* (2007) 47:1045–52. doi:10.1088/0029-5515/47/8/039

70. Fernandez A, Cappa A, Castejón F, Fontdecaba JM, Nagasaki K. ECCD experiments in the TJ-II stellarator. *Fusion Sci Technol* (2008) 53:254–60. doi:10.13182/fst08-a1670

71. Yamamoto S, Nagasaki K, Nagaoka K, Varela J, Cappa Á, Ascasíbar E, et al. Effect of ECH/ECCD on energetic-particle-driven MHD modes in helical plasmas. *Nucl Fusion* (2020) 60:066018. doi:10.1088/1741-4326/ab7f13

72. Nagasaki K, Isayama A, Hayashi N, Ozeki T, Takechi M, Oyama N, et al. Stabilization of neoclassical tearing mode by ECCD and its evolution simulation on JT-60U tokamak. *Nucl Fusion* (2005) 45:1608–17. doi:10.1088/0029-5515/45/12/016

73. Prater R, Haye RL, Luce T, Petty C, Strait E, Ferron J, et al. Stabilization and prevention of the 2/1 neoclassical tearing mode for improved performance in DIII-D. *Nucl Fusion* (2007) 47:371–7. doi:10.1088/0029-5515/47/5/001

74. Fasoli A, Borba D, Gormezano C, Heeter R, Jaun A, Jacquinot J, et al. Alfvén eigenmode experiments in tokamaks and stellarators *Plasma Phys. Control. Fusion* (1997) 39:B287. doi:10.1088/0741-3335/39/12B/022

75. Felici F, Goodman T, Sauter O, Canal G, Coda S, Duval B, et al. Integrated real-time control of MHD instabilities using multi-beam ECRH/ECCD systems on TCV. *Nucl Fusion* (2015) 52:074001. doi:10.1088/0029-5515/52/7/074001

76. Petty CC, Nazikian R, Park J, Turco F, Chen X, Cui L, et al. Advances in the steady-state hybrid regime in DIII-D—a fully non-inductive, ELM-suppressed scenario for ITER. *Nucl Fusion* (2017) 57:116057. doi:10.1088/1741-4326/aa80ab

77. Kim J, Kang J, Rhee T, Jo J, Han H, Podestà M, et al. Suppression of toroidal Alfvén eigenmodes by the electron cyclotron current drive in KSTAR plasmas. *Nucl Fusion* (2022) 62:026029. doi:10.1088/1741-4326/ac3e39

78. Sallander E, Weller A, Team WA. Effects of non-vanishing toroidal current densities on stability in the Wendelstein 7-AS stellarator. *Nucl Fusion* (2000) 40:1499–509. doi:10.1088/0029-5515/40/8/308

79. Castejon F, Fujisawa A, Ida K, Talmadge JN, Estrada T, López-Bruna D, et al. Influence of magnetic topology on transport and stability in stellarators. *Plasma Phys Control Fusion* (2005) 47:B53–69. doi:10.1088/0741-3335/47/12b/s05

80. Nagaoka K, Ido T, Ascasíbar E, Estrada T, Yamamoto S, Melnikov A, et al. Mitigation of NBI-driven Alfvén eigenmodes by electron cyclotron heating in the TJ-II stellarator. *Nucl Fusion* (2013) 53:072004. doi:10.1088/0029-5515/53/7/072004

81. Garcia L, Ochando MA, Carreras BA, Carralero D, Hidalgo C, van Milligen BP. Effect of fast electrons on the stability of resistive interchange modes in the TJ-II stellarator. *Phys Plasma* (2016) 23:062319. doi:10.1063/1.4954826

82. Melnikov AV, Krupnik L, Eliseev L, Barcala J, Bravo A, Chmyga A, et al. Heavy ion beam probing—diagnostics to study potential and turbulence in toroidal plasmas. *Nucl Fusion* (2017) 57:072004. doi:10.1088/1741-4326/aa5382

83. Stix TH. Generation and thermalization of plasma waves. *Phys Fluids* (1958) 1(4): 308–17. doi:10.1063/1.1705889

84. Du XD, Toi K, Osakabe M, Ohdachi S, Ido T, Tanaka K, et al. Resistive interchange modes destabilized by helically trapped energetic ions in a helical plasma. *Phys Rev Lett* (2015) 114:155003. doi:10.1103/PhysRevLett.114.155003

85. Du XD, Toi K, Ohdachi S, Osakabe M, Ido T, Tanaka K, et al. Resistive interchange mode destabilized by helically trapped energetic ions and its effects on energetic ions and bulk plasma in a helical plasma. *Nucl Fusion* (2016) 56:016002. doi:10.1088/0029-5515/56/1/016002

86. Du XD, Toi K, Ohdachi S, Watanabe KY, Takahashi H, Yoshimura Y, et al. Suppression of trapped energetic ions driven resistive interchange modes with electron cyclotron heating in a helical plasma. *Phys Rev Lett* (2017) 118:125001. doi:10.1103/PhysRevLett.118.125001

87. Pace DC, Austin ME, Bardoczi L, Collins CS, Crowley B, Davis E, et al. Dynamic neutral beam current and voltage control to improve beam efficacy in tokamaks. *Phys Plasmas* (2018) 25:056109. doi:10.1063/1.5016160

88. Collins C, Heidbrink W, Podestà M, White R, Kramer G, Pace D, et al. Phase-space dependent critical gradient behavior of fast-ion transport due to Alfvén eigenmodes. *Nucl Fusion* (2017) 57:086005. doi:10.1088/1741-4326/aa720c

89. Van Zeeland MA, Heidbrink WW, Fisher RK, García Muñoz M, Kramer GJ, Pace DC, et al. Measurements and modeling of Alfvén eigenmode induced fast ion transport and loss in DIII-D and ASDEX Upgrade. *Phys Plasmas* (2011) 18:056114. doi:10.1063/1.3574663

90. Fenstermacher ME, Abbate J, Abe S, Abrams T, Adams M, Adamson B, et al. DIII-D research advancing the physics basis for optimizing the tokamak approach to fusion energy. *Nucl Fusion* (2022) 62:042024. doi:10.1088/1741-4326/ac2ff2

91. Kramer GJ, Bortolon A, Ferraro NM, Spong DA, Crocker NA, Darrow DS, et al. Mitigation of Alfvénic activity by 3D magnetic perturbations on NSTX. *Plasma Phys Control Fusion* (2016) 58:085003. doi:10.1088/0741-3335/58/8/085003

92. Ida K, Yoshinuma M, Kobayashi M, Kobayashi T, Kenmochi N, Nespoli F, et al. Overview of Large Helical Device experiments of basic plasma physics for solving crucial issues in reaching burning plasma conditions. *Nucl Fusion* (2024) 64:112009. doi:10.1088/1741-4326/ad3a7a

93. Fu GY, Cheng C, Budny R, Chang Z, Darrow D, Fredrickson E, et al. Stability analysis of toroidicity-induced Alfvén eigenmodes in TFTR deuterium-tritium experiments. *Phys Rev Lett* (1995) 75:2336–9. doi:10.1103/PhysRevLett.75.2336

94. Fu GY, Cheng CZ, Budny R, Chang Z, Darrow DS, Fredrickson E, et al. Analysis of alpha particle-driven toroidal Alfvén eigenmodes in Tokamak Fusion Test Reactor deuterium–tritium experiments. *Plasma Phys* (1996) 3:4036–4045. doi:10.1063/1.871537

95. Nazikian R, Fu GY, Batha SH, Bell MG, Bell RE, Budny RV, et al. Alpha-particle-driven toroidal Alfvén eigenmodes in the tokamak fusion test reactor. *Phys Rev Lett* (1997) 78:2976–9. doi:10.1103/physrevlett.78.2976

96. Spong DA, Carreras BA, Hedrick CL. Linearized gyrofluid model of the alpha-destabilized toroidal Alfvén eigenmode with continuum damping effects. *Phys.Fluids B* (1992) 4:3316–28. doi:10.1063/1.860386

97. Spong DA, Hedrick C, Carreras B. Strategies for modifying alpha driven TAE thresholds through q profile and ion temperature control. *Nucl Fusion* (1995) 35: 1687–96. doi:10.1088/0029-5515/35/12/i33

98. Fitzgerald M, Sharapov S, Siren P, Tholerus E, Dreval M, Szepesi G, et al. Toroidal Alfvén eigenmode stability in JET internal transport barrier afterglow experiments. *Nucl Fusion* (2022) 62:106001. doi:10.1088/1741-4326/ac84ee

99. Fitzgerald M, Dumont R, Keeling D, Mailloux J, Sharapov S, Dreval M, et al. Stability analysis of alpha driven toroidal Alfvén eigenmodes observed in JET deuterium-tritium internal transport barrier plasmas. *Nucl Fusion* (2023) 63:112006. doi:10.1088/1741-4326/acee14

100. Porcelli F, Stankiewicz R, Kerner W, Berk HL. Solution of the drift-kinetic equation for global plasma modes and finite particle orbit widths. *Plasmas* (1994) 1: 470–80. doi:10.1063/1.870792

101. Varela J, Spong D, Garcia L. Analysis of Alfven eigenmode destabilization in ITER using a Landau closure model. *Nucl Fusion* (2019) 59:076036. doi:10.1088/1741-4326/ab1ebe

102. Huang J, Garofalo A, Qian J, Gong X, Ding S, Varela J, et al. Progress in extending high poloidal beta scenarios on DIII-D towards a steady-state fusion reactor and impact of energetic particles. *Nucl Fusion* (2020) 60:126007. doi:10.1088/1741-4326/abaf33

103. Varela J, Huang J, Spong D, Chen J, Chan V, Garcia L, et al. Theoretical study of the Alfven eigenmode stability in CFETR steady state discharges. *Nucl Fusion* (2022) 62: 036005. doi:10.1088/1741-4326/ac4778

104. Varela J, Spong DA, Garcia L, Todo Y, Huang J, Murakami M. Study of Alfven eigenmodes stability in plasma with multiple NBI driven energetic particle species. *Phys.Plasmas* (2019) 26:062502. doi:10.1063/1.5098347

105. Garcia L. *Proceedings of the 25th EPS international conference, 22A*. Prague (1998). p. 1757.

106. Charlton LA, Holmes J, Hicks H, Lynch V, Carreras B. Numerical calculations using the full MHD equations in toroidal geometry. *J Comp. Phys* (1986) 63:107–29. doi:10.1016/0021-9991(86)90086-0

107. Charlton LA, Holmes J, Lynch V, Carreras B, Hender T. Compressible linear and nonlinear resistive MHD calculations in toroidal geometry. *J Comp. Phys* (1990) 86: 270–93. doi:10.1016/0021-9991(90)90102-7

108. Hedrick CL, Leboeuf JN, Spong DA. Alpha-Alfvén local dispersion relation and solutions. *Phys.Fluids B* (1992) 4:3869–82. doi:10.1063/1.860344

109. Varela J, Spong D, Garcia L. Analysis of Alfvén eigenmode destabilization by energetic particles in Large Helical Device using a Landau-closure model. *Nucl Fusion* (2017) 57:046018. doi:10.1088/1741-4326/aa5d04

110. Spong DA. Simulation of Alfvén frequency cascade modes in reversed shear-discharges using a Landau-closure model. *Nucl Fusion* (2013) 53:053008. doi:10.1088/0029-5515/53/5/053008

111. Hirshman SP, Whitson JC. Steepest-descent moment method for three-dimensional magnetohydrodynamic equilibria. *Phys Fluids* (1983) 26:3553–3568. doi:10.1063/1.864116

112. Brix M, Hawkes NC, Boboc A, Drozdov V, Sharapov SE, JET-EFDA Contributors. Accuracy of EFIT equilibrium reconstruction with internal diagnostic information at JET. *Rev Sci Instrum* (2008) 79:10F325. doi:10.1063/1.2964180

113. Mishchenko A, Cole M, Kleiber R, Könies A. New variables for gyrokinetic electromagnetic simulations. *Plasmas* (2014) 21:092110. doi:10.1063/1.4880560

114. Chen Y, Parker SE. A δf particle method for gyrokinetic simulations with kinetic electrons and electromagnetic perturbations. *J Comp. Phys* (2003) 189:463–75. doi:10.1016/s0021-9991(03)00228-6

115. Candy J, Waltz R. An Eulerian gyrokinetic-Maxwell solver. *J Comp. Phys* (2003) 186:545–81. doi:10.1016/s0021-9991(03)00079-2

116. Lin Z, Hahm TS, Lee WW, Tang WM, White RB. Turbulent transport reduction by zonal flows: massively parallel simulations. *Science* (1998) 281:1835–7. doi:10.1126/science.281.5384.1835

117. Bottino A, Peeters AG, Hatzky R, Jolliet S, McMillan BF, Tran TM, et al. Nonlinear low noise particle-in-cell simulations of electron temperature gradient driven turbulence. *Phys Plasmas* (2007) 14:010701. doi:10.1063/1.2428280

118. Citrin J, Garcia J, Görler T, Jenko F, Mantica P, Told D, et al. Electromagnetic stabilization of tokamak microturbulence in a high-βregime. *Plasma Phys Control Fusion* (2015) 57:014032. doi:10.1088/0741-3335/57/1/014032

119. Todo Y, Shinohara K, Takechi M, Ishikawa M. Nonlocal energetic particle mode in a JT-60U plasma. *Plasmas* (2005) 12:012503. doi:10.1063/1.1828084

120. Breslau J, Ferraro N, Jardin S. Some properties of the M3D-C1 form of the three-dimensional magnetohydrodynamics equations. *Plasmas* (2009) 16:092503. doi:10.1063/1.3224035

121. Lauber P, Günter S, Könies A, Pinches S. LIGKA: a linear gyrokinetic code for the description of background kinetic and fast particle effects on the MHD stability in tokamaks. *J Comput Phys* (2007) 226:447–65. doi:10.1016/j.jcp.2007.04.019

122. Liu Y, Chu MS, Chapman IT, Hender TC. Publisher's Note: "Third harmonic generation of a short pulse laser in a plasma density ripple created by a machining beam" [Phys. Plasmas 15, 023106 (2008)]. *Plasmas* (2008) 15:112503. doi:10.1063/1.3008045

123. Taimourzadeh S, Bass E, Chen Y, Collins C, Gorelenkov N, Könies A, et al. Verification and validation of integrated simulation of energetic particles in fusion plasmas. *Nucl Fusion* (2019) 59:066006. doi:10.1088/1741-4326/ab0c38

124. Chen L, Zonca F. Physics of Alfvén waves and energetic particles in burning plasmas. *Rev Mod Phys* (2016) 88:015008. doi:10.1103/revmodphys.88.015008

125. Boozer AH. Establishment of magnetic coordinates for a given magnetic field. *Phys Fluids* (1982) 25:520–1. doi:10.1063/1.863765

126. Lambers JV, Sumner AC. *Explorations in numerical analysis*. Singapore: World Scientific (2018).

127. Wakatani M. *Stellarator and Heliotron devices. 0195078314*. Oxford University Press (1998).

128. Stix TH. Fast-wave heating of a two-component plasma. *Nucl Fusion* (1975) 15: 737–54. doi:10.1088/0029-5515/15/5/003

129. Wilkie GJ. Analytic slowing-down distributions as modified by turbulent transport. *J Plasma Phys* (2018) 84:745840601. doi:10.1017/s0022377818001058

130. Hedrick CL, Leboeuf JN. Landau fluid equations for electromagnetic and electrostatic fluctuations. *Phys.Fluids B* (1992) 4:3915–34. doi:10.1063/1.860348

131. Varela J, Spong D, Garcia L, Ohdachi S, Watanabe K, Seki R. Analysis of the MHD stability and energetic particles effects on EIC events in LHD plasma using a Landau-closure model. *Nucl Fusion* (2019) 59:046008. doi:10.1088/1741-4326/aaff80

132. Suzuki Y, Yamada H, Nakajima N, Watanabe K, Nakamura Y, Hayashi T. Theoretical considerations of doublet-like configuration in LHD. *Nucl Fusion* (2006) 46: 123–32. doi:10.1088/0029-5515/46/1/014

133. Nagaoka K, Ida K, Yoshinuma M, Takeiri Y, Yokoyama M, Morita S, et al. Heat and momentum transport of ion internal transport barrier plasmas on the Large Helical Device. *Nucl Fusion* (2011) 51:083022. doi:10.1088/0029-5515/51/8/083022

134. Ascasíbar E, Alba D, Alegre D, Alonso A, Alonso J, de Aragón F, et al. Overview of recent TJ-II stellarator results. *Nucl Fusion* (2019) 59:112019. doi:10.1088/1741-4326/ab205e

135. Ido T, Shimizu A, Nishiura M, Nakamura S, Kato S, Nakano H, et al. Potential fluctuation associated with the energetic-particle-induced geodesic acoustic mode in the Large Helical Device. *Nucl Fusion* (2011) 51:073046. doi:10.1088/0029-5515/51/7/073046

136. Toi K, Watanabe F, Tokuzawa T, Ida K, Morita S, Ido T, et al. Observation of reversed-shear Alfvén eigenmodes excited by energetic ions in a helical plasma. *Phys Rev Lett* (2010) 105:145003. doi:10.1103/PhysRevLett.105.145003

137. Toi K, Yamamoto S, Nakajima N, Ohdachi S, Sakakibara S, Osakabe M, et al. Energetic ion driven Alfvén eigenmodes in Large Helical Device plasmas with three-dimensional magnetic structure and their impact on energetic ion transport. *Plasma Phys Control Fusion* (2004) 46:S1–S13. doi:10.1088/0741-3335/46/7/s01

138. Melnikov AV, Eliseev L, Ascasibar E, Chmyga A, Hidalgo C, Ido T, et al. Alfvén eigenmode properties and dynamics in the TJ-II stellarator. *Nucl Fusion* (2012) 52: 123004. doi:10.1088/0029-5515/52/12/123004

139. Melnikov AV, Ochando M, Ascasibar E, Castejon F, Cappa A, Eliseev L, et al. Effect of magnetic configuration on frequency of NBI-driven Alfvén modes in TJ-II. *Nucl Fusion* (2014) 54:123002. doi:10.1088/0029-5515/54/12/123002

140. Osakabe M, Yamamoto S, Toi K, Takeiri Y, Sakakibara S, Nagaoka K, et al. Experimental observations of enhanced radial transport of energetic particles with Alfvén eigenmode on the LHD. *Nucl Fusion* (2006) 46:S911–7. doi:10.1088/0029-5515/46/10/s07

141. Kamio S, Fujiwara Y, Nagaoka K, Ogawa K, Seki R, Yamaguchi H, et al. Observation of clump structure in transported particle orbit using an upgraded neutral particle analyzer during TAE burst in LHD. *Nucl Fusion* (2020) 60:112002. doi:10.1088/1741-4326/ab7890

142. Todo Y, Seki R, Spong DA, Wang H, Suzuki Y, Yamamoto S, et al. Comprehensive magnetohydrodynamic hybrid simulations of fast ion driven instabilities in a Large Helical Device experiment. *Plasma Phys* (2017) 24:081203. doi:10.1063/1.4997529

143. Seki R, Todo Y, Suzuki Y, Spong D, Ogawa K, Isobe M, et al. Comprehensive magnetohydrodynamic hybrid simulations of Alfvén eigenmode bursts and fast-ion losses in the Large Helical Device. *Nucl Fusion* (2019) 59:096018. doi:10.1088/1741-4326/ab266e

144. Spong DA, Sanchez R, Weller A. Shear Alfvén continua in stellarators. *Plasma Phys* (2003) 10:3217–24. doi:10.1063/1.1590316

145. Nave MFF, Campbell D, Joffrin E, Marcus F, Sadler G, Smeulders P, et al. Fishbone activity in JET. *Nucl Fusion* (1991) 31:697–710. doi:10.1088/0029-5515/31/4/007

146. Toi K, Ohdachi S, Yamamoto S, Sakakibara S, Narihara K, Tanaka K, et al. Observation of the low to high confinement transition in the large helical device. *Phys Plasmas* (2005) 12:020701. doi:10.1063/1.1843122

147. Watanabe KY, Masamune S, Takemura Y, Funaba H, Sakakibara S, Watanabe F, et al. Effect of pressure-driven MHD instabilities on confinement in reactor-relevant high-beta helical plasmas. *Phys Plasmas* (2011) 18:056119. doi:10.1063/1.3592675

148. Ueda R, Watanabe KY, Matsumoto Y, Itagaki M, Sato M, Oikawa S. Characteristics of magnetic island formation due to resistive interchange instability in helical plasma. *Phys Plasmas* (2014) 21:052502. doi:10.1063/1.4875340

149. Sakakibara S, Watanabe KY, Suzuki Y, Narushima Y, Ohdachi S, Nakajima N, et al. MHD study of the reactor-relevant high-beta regime in the Large Helical Device. *Plasmas Phys Control Fusion* (2008) 50:124014. doi:10.1088/0741-3335/50/12/124014

150. Ogawa K, Isobe M, Kawase H, Nishitani T, Seki R, Osakabe M. Observation of enhanced radial transport of energetic ion due to energetic particle mode destabilized by helically-trapped energetic ion in the Large Helical Device. *Nucl Fusion* (2018) 58: 044001. doi:10.1088/1741-4326/aaab18

151. Ogawa K, Isobe M, Kawase H, Nishitani T, Seki R, Osakabe M, et al. Effect of the helically-trapped energetic-ion-driven resistive interchange modes on energetic ion confinement in the Large Helical Device. *Plasma Phys Control Fusion* (2018) 60:044005. doi:10.1088/1361-6587/aaab1f

152. Varela J, Spong D, Garcia L. Analysis of Alfven eigenmodes destabilization by energetic particles in TJ-II using a Landau-closure model. *Nucl Fusion* (2017) 57: 126019. doi:10.1088/1741-4326/aa83c4

153. Cappa A, Varela J, López Bruna D, Ascasíbar E, Liniers M, Eliseev L, et al. Stability analysis of TJ-II stellarator NBI driven Alfvén eigenmodes in ECRH and ECCD experiments. *Nucl Fusion* (2021) 61:066019. doi:10.1088/1741-4326/abf74b

154. Eliseev LG, Melnikov AV, Ascasibar E, Cappa A, Drabinskiy M, Hidalgo C, et al. Experimental observation of the geodesic acoustic frequency limit for the NBI-driven Alfvén eigenmodes in TJ-II. *Phys Plasmas* (2021) 28:072510. doi:10.1063/5.0049225

155. Eliseev LG, Melnikov AV, Lysenko SE. Study of Alfvén eigenmodes with heavy ion beam probing in the TJ-II stellarator. *Rev Mod Plasma Phys* (2022) 6:25. doi:10.1007/s41614-022-00088-y

156. Melnikov AV, Hidalgo C, Chmyga AA, Dreval NB, Eliseev LG, Khrebtov SM, et al. Plasma Potential Measurements by the Heavy Ion Beam Probe Diagnostic in Fusion Plasmas: Biasing Experiments in the TJ-II Stellarator and T-10 Tokamak. *Fusion Sci Technol* (2004) 46:299–311. doi:10.13182/FST04-A568

157. Melnikov AV, Alonso A, Ascasíbar E, Balbin R, Chmyga AA, Dnestrovskij YN, et al. Plasma potential evolution study by HIBP diagnostic during NBI experiments in the TJ-II stellarator. *Fusion Sci.Technol.* (2007) 51:31–7. doi:10.13182/fst07-a1284

158. Melnikov AV. *Electric potential in toroidal plasmas*. Switzerland: Springer Nature (2019).

159. Turnbull AD, Chu MS, Strait EJ, Lao LL, Greene JM, Taylor TS, et al. *Global Alfven eigenmodes in DIII-D*. San Diego, CA: General Atomics (1992).

160. Strait EJ, Heidbrink W, Turnbull A, Chu M, Duong H. Stability of neutral beam driven TAE modes in DIII-D. *Nucl Fusion* (1993) 33:1849–70. doi:10.1088/0029-5515/33/12/i07

161. Heidbrink W, Van Zeeland M, Austin M, Bass E, Ghantous K, Gorelenkov N, et al. The effect of the fast-ion profile on Alfvén eigenmode stability. *Nucl Fusion* (2013) 53:093006. doi:10.1088/0029-5515/53/9/093006

162. Heidbrink W, Strait EJ, Chu MS, Turnbull AD. Observation of beta-induced Alfvén eigenmodes in the DIII-D tokamak. *Phys Rev Lett* (1993) 71:855–8. doi:10.1103/physrevlett.71.855

163. Van Zeeland MA, Austin M, Carlstrom T, Deterly T, Finkenthal D, Holcomb C, et al. Internal Alfvén eigenmode observations on DIII-D. *Nucl Fusion* (2006) 46:S880–7. doi:10.1088/0029-5515/46/10/s03

164. Pace DC, Fisher RK, García-Muñoz M, Heidbrink WW, Van Zeeland MA. Convective beam ion losses due to Alfvén eigenmodes in DIII-D reversed-shear plasmas. *Plasma Phys Control Fusion* (2011) 53:062001. doi:10.1088/0741-3335/53/6/062001

165. Van Zeeland MA, Gorelenkov N, Heidbrink W, Kramer G, Spong D, Austin M, et al. Alfvén eigenmode stability and fast ion loss in DIII-D and ITER reversed magnetic shear plasmas. *Nucl Fusion* (2012) 52:094023. doi:10.1088/0029-5515/52/9/094023

166. Heidbrink W. Energetic ion experiments in DIII-D. *Fusion Sci Technol* (2017) 48: 945–53. doi:10.13182/fst05-a1050

167. Varela J, Spong D, Garcia L, Huang J, Murakami M, Garofalo A, et al. Analysis of Alfven eigenmode destabilization in DIII-D high poloidal β discharges using a Landau closure model. *Nucl Fusion* (2018) 58:076017. doi:10.1088/1741-4326/aac33f

168. Ding S, Garofalo AM, Qian J, Cui L, McClenaghan JT, Pan C, et al. Confinement improvement in the high poloidal beta regime on DIII-D and application to steady-state H-mode on EAST. *Phys Plasmas* (2017) 24:056114. doi:10.1063/1.4982058

169. Garofalo AM, Gong X, Qian J, Chen J, Li G, Li K, et al. Development of high poloidal beta, steady-state scenario with ITER-like tungsten divertor on EAST. *Nucl Fusion* (2017) 57:076037. doi:10.1088/1741-4326/aa7186

170. Ding S, Xu G, Wang Q, Solomon W, Zhao Y, Gong X, et al. Scenario development for high β_p low torque plasma with q_{min} above 2 and large-radius internal transport barrier in DIII-D. *Nucl Fusion* (2017) 57:022016. doi:10.1088/0029-5515/57/2/022016

171. Litaudon X, B coulet A, Crisanti F, Wolf R, Baranov Y, Barbato E, et al. Progress towards steady-state operation and real-time control of internal transport barriers in JET. *Nucl Fusion* (2003) 43:565–72. doi:10.1088/0029-5515/43/7/309

172. Qian JP, Garofalo A, Gong X, Ren Q, Ding S, Solomon W, et al. Advances in the high bootstrap fraction regime on DIII-D towards the$Q$ = 5 mission of ITER steady state. *Nucl Fusion* (2017) 57:056008. doi:10.1088/1741-4326/aa626a

173. Huang J, et al. Collaborative research: the evolution of magnetic skeletons during 3D reconnection. *APS division Plasma Phys Meet San Jose* (2016).

174. Huang J, Qian J, Garofalo A, Gong X, Wu C, Chang J, et al. Improved high-performance fully non-inductive discharge by optimizing the fast-ion confinement on EAST. *Nucl Fusion* (2020) 60:016002. doi:10.1088/1741-4326/ab443a

175. McClenaghan J, Garofalo A, Lao L, Weisberg D, Meneghini O, Smith S, et al. Transport at high βp and development of candidate steady state scenarios for ITER. *Nucl Fusion* (2020) 60:046025. doi:10.1088/1741-4326/ab74a0

176. Wan YX, Li J, Liu Y, Wang X, Chan V, Chen C, et al. Overview of the present progress and activities on the CFETR. *Nucl Fusion* (2017) 57:102009. doi:10.1088/1741-4326/aa686a

177. Zhuang G, Li G, Li J, Wan Y, Liu Y, Wang X, et al. Progress of the CFETR design. *Nucl Fusion* (2019) 59:112010. doi:10.1088/1741-4326/ab0e27

178. Huang J., Garofalo AM, Qian JP, Gong XZ, Ding SY, Varela J, et al. Progress in extending high poloidal beta scenarios on DIII-D towards a steady-state fusion reactor and impact of energetic particles. *Nucl Fusion* (2020) 60:126007. doi:10.1088/1741-4326/abaf33

179. Varela J, Ohdachi S, Watanabe K, Spong D, Garcia L, Seki R. Theoretical analysis of energetic-ion-driven resistive interchange mode stabilization strategies using a Landau closure model. *Nucl Fusion* (2020) 60:046013. doi:10.1088/1741-4326/ab7213

180. Li J, Guo HY, Wan BN, Gong XZ, Liang YF, Xu GS, et al. A long-pulse high-confinement plasma regime in the Experimental Advanced Superconducting Tokamak. *Nat Phys* (2013) 9:817–821. doi:10.1038/nphys2795

181. Hu C, Xie Y, Xie Y, Liu S, Xu Y, Liang L, et al. Overview of development status for EAST-NBI system. *Plasma Sci Technol* (2015) 17:817–25.

182. Hu Y, Todo Y, Pei Y, Li G, Qian J, Xiang N, et al. Simulation of fast-ion-driven alfvén eigenmodes on the experimental advanced superconducting tokamak. *Phys Plasmas* (2016) 23:022505. doi:10.1063/1.4941970

183. Pei Y, Xiang N, Shen W, Hu Y, Todo Y, Zhou D, et al. Simulations of toroidal alfvén eigenmode excited by fast ions on the experimental advanced superconducting tokamak. *Phys Plasmas* (2018) 25:052503. doi:10.1063/1.5023538

184. Liqing X, Wei S, Zhenzhen R, Tianfu Z, Yifeng W, Lian H, et al. Investigation of Alfvén eigenmodes and energetic particle modes in EAST with neutral beam injection *Nucl Fusion* (2021) 61:076005. doi:10.1088/1741-4326/abf2e2

185. Wang XH, Huang J, Varela J, Zhao H, Spong D, Xu L, et al. Analysis of beam ion driven Alfvén eigenmode stability induced by Tungsten contamination in EAST. *Nucl Fusion* (2024) 64:016028. doi:10.1088/1741-4326/ad0f5e

186. Chu N, Sun Y, Gu S, Wang H, Hu Y, Shi T, et al. Observation of toroidal Alfvén eigenmode excited by energetic electrons induced by static magnetic perturbations in the EAST tokamak. *Nucl Fusion* (2018) 58:104004. doi:10.1088/1741-4326/aad70c

187. Osakabe M, Takahashi H, Yamada H, Tanaka K, Kobayashi T, Ida K, et al. Recent results from deuterium experiments on the large helical device and their contribution to fusion reactor development. *Nucl Fusion* (2022) 62:042019. doi:10.1088/1741-4326/ac3cda

188. Hidalgo C, et al. *Nucl Fusion* (2022) 62:042025.

189. Ortiz J, Varela J, Spong D, Garcia L, Ghai Y. Study of Alfvén eigenmode stability in Quasi-Poloidal Stellarator (QPS) plasma using a Landau closure model. *Nucl Fusion* (2024) 63:056010. under review, Analysis of the HAE activity in the TJII using Landau closure model. doi:10.1088/1741-4326/acc25f

190. Garcia J, Kazakov Y, Coelho R, Dreval M, de la Luna E, Solano ER, et al. Stable Deuterium-Tritium burning plasmas with improved confinement in the presence of energetic ions instabilities. *Sci Adv* (2024). under review.

191. Sun Y, Benmhammed H, Al Abdullatif S, Habara A, Fu E, Brady J, et al. PGC-1α agonism induces fetal hemoglobin and exerts antisickling effects in sickle cell disease. *Sci Adv* (2024) 10:eadn8750. under review, Fast ion studies in the extended high-performance high βp plasma on EAST. doi:10.1126/sciadv.adn8750

192. Varela J, Nagasaki K, Nagaoka K, Yamamoto S, Watanabe KY, Spong DA, et al. Modeling of the ECCD injection effect on the Heliotron J and LHD plasma stability. *Nucl Fusion* (2020) 60:112015. doi:10.1088/1741-4326/abad84

193. Garcia-Munoz M, Sharapov SE, Van Zeeland MA, Ascasibar E, Cappa A, Chen L, et al. Active control of Alfvén eigenmodes in magnetically confined toroidal plasmas. *Plasma Phys Control Fusion* (2019) 61:054007. doi:10.1088/1361-6587/aaef08

194. Ohdachi S, Takahashi Y, Suzuki M, Osakabe T, Morisaki T, Bando K, et al. *27 th IAEA fusion energy conference* (2018). EX/1-3Rb. Available at: https://www.iaea.org/sites/default/files/18/10/cn-258-abstracts.pdf

195. Liu H, Shimizu A, Isobe M, Okamura S, Nishimura S, Suzuki C, et al. Magnetic configuration and modular coil design for the Chinese first quasi-axisymmetric stellarator. *Plasma Fusion Res* (2018) 13:3405067. doi:10.1585/pfr.13.3405067

196. Shimizu A, Liu H, Kinoshita S, Isobe M, Okamura S, Ogawa K, et al. Consideration of the influence of coil misalignment on the Chinese first quasi-axisymmetric stellarator magnetic configuration. *Plasma Fusion Res* (2019) 14:3403151. doi:10.1585/pfr.14.3403151

197. Yang L, Liu H, Shimizu A, Xu Y, Wang X, Liu H, et al. Local axisymmetry-breaking–induced transition of trapped-particle orbit and loss channels in quasi-axisymmetric stellarators. *Europhysics Lett* (2020) 129:35001. doi:10.1209/0295-5075/129/35001

198. Zarnstorff MC, Berry LA, Brooks A, Fredrickson E, Fu GY, Hirshman S, et al. Physics of the compact advanced stellarator NCSX. *Plasma Phys Control Fusion* (2001) 43:A237–49. doi:10.1088/0741-3335/43/12a/318

199. Nelson BE. Design of the quasi-poloidal stellarator experiment (QPS). *Fusion Eng Des* (2003) 66:205.

200. Nuhrenberg J, Zille R. Quasi-helically symmetric toroidal stellarators. *Phys Lett A* (1988) 129:113–7. doi:10.1016/0375-9601(88)90080-1

201. Landreman M, Catto PJ. Omnigenity as generalized quasisymmetry. *Plasmas* (2012) 19:056103. doi:10.1063/1.3693187

202. Ogawa K, Seki R, Yamaguchi H, Murakami S, Isobe M, Shimizu A, et al. Feasibility study of neutral beam injection on Chinese first quasi-axisymmetric stellarator (CFQS). *Plasma Fusion Res* (2019) 14:3402067. doi:10.1585/pfr.14.3402067

203. Varela J, Shimizu A, Spong D, Garcia L, Ghai Y. Study of the Alfven eigenmodes stability in CFQS plasma using a Landau closure model. *Nucl Fusion* (2021) 61:026023. doi:10.1088/1741-4326/abd072

204. Strickler DJ, Hirshman SP, Spong DA, Cole MJ, Lyon JF, Nelson BE, et al. Development of a robust quasi-poloidal compact stellarator. *Sci Technol* (2004) 45:15–26. doi:10.13182/fst04-a421

205. Spong DA, Harris JH. New QP/QI symmetric stellarator configurations. *Plasma Fusion Res* (2010) 5:S2039. doi:10.1585/pfr.5.s2039

206. Hudson SR, Hegna CC, Torasso R, Ware A. Marginal stability diagrams for infinite-*n*ballooning modes in quasi-symmetric stellarators. *Plasma Phys Control Fusion* (2004) 46:869–76. doi:10.1088/0741-3335/46/5/009

207. Spong DA Generation and damping of neoclassical plasma flows in stellarators. *Phys Plasmas* (2005) 12:056114. doi:10.1063/1.1887172

208. Rewoldt G, Ku LP, Tang WM. Comparison of microinstability properties for stellarator magnetic geometries. *Plasmas* (2005) 12:102512. doi:10.1063/1.2089247

209. Ortiz J, Varela J, Spong D, Garcia L, Ghai Y. Study of Alfvén eigenmode stability in Quasi-Poloidal Stellarator (QPS) plasma using a Landau closure model. *Nucl Fusion* (2023) 63:056010. doi:10.1088/1741-4326/acc25f

210. Wolf RC, Hobirk J, Conway G, Gruber O, Gude A, Günter S, et al. Performance, heating and current drive scenarios of ASDEX Upgrade advanced tokamak discharges. *Nucl Fusion* (2001) 41:1259–71. doi:10.1088/0029-5515/41/9/315

211. Wolf RC, Biel W, de Bock MFM, Finken KH, Günter S, Hogeweij GMD, et al. *20th IAEA fusion energy conference, paper IAEA-CN-116/EX/6-5 conference symposium papers CD ROM, IAEA-CSP25/CD*. IAEA Vienna (2005). ISBN 92-0-100405-2, ISSN 1562-4153.

212. Murakami M, John HS, Casper T, Chu M, DeBoo J, Greenfield C, et al. Status of advanced tokamak scenario modelling with off-axis electron cyclotron current drive in DIII-D. *Nucl Fusion* (2000) 40:1257–65. doi:10.1088/0029-5515/40/6/320

213. Wade MR, Murakami M, Luce T, Ferron J, Petty C, Brennen D, et al. Integrated, advanced tokamak operation on DIII-D. *Nucl Fusion* (2003) 43:634–46. doi:10.1088/0029-5515/43/7/318

214. Wade MR. Development in the DIII-D tokamak of advanced operating scenarios and associated control techniques for ITER. *Nucl Fusion* (2007) 47:S543–62. doi:10.1088/0029-5515/47/10/s05

215. Garofalo AM, Gong X, Grierson B, Ren Q, Solomon W, Strait E, et al. Compatibility of internal transport barrier with steady-state operation in the high bootstrap fraction regime on DIII-D. *Nucl Fusion* (2015) 55:123025. doi:10.1088/0029-5515/55/12/123025

216. Ren H. The residual zonal flows in anisotropic tokamak plasmas. *Phys Plasmas* (2016) 23:062511. doi:10.1063/1.4954914

217. Ferron JR, Casper TA, Doyle EJ, Garofalo AM, Gohil P, Greenfield CM, et al. Optimization of DIII-D advanced tokamak discharges with respect to the β limit. *Phys Plasmas* (2005) 12:056126. doi:10.1063/1.1871247

218. Holcomb CT, Ferron JR, Luce TC, Petrie TW, Politzer PA, Challis C, et al. Optimizing stability, transport, and divertor operation through plasma shaping for steady-state scenario development in DIII-D. *Phys Plasmas* (2009) 16:056116. doi:10.1063/1.3125934

219. Piovesan P, Igochine V, Turco F, Chrystal I, Classen M, Dunne NM, et al. Impact of ideal MHD stability limits on high-beta hybrid operation. *Plasma Phys Control Fusion* (2017) 59:014027. doi:10.1088/0741-3335/59/1/014027

220. Doyle EJ, DeBoo J, Ferron J, Jackson G, Luce T, Murakami M, et al. Demonstration of ITER operational scenarios on DIII-D. *Nucl Fusion* (2010) 50:075005. doi:10.1088/0029-5515/50/7/075005

221. Litaudon X, Voitsekhovitch I, Artaud J, Belo P, João PS, Bizarro JP, et al. Modelling of hybrid scenario: from present-day experiments towards ITER. *Nucl Fusion* (2013) 53:073024. doi:10.1088/0029-5515/53/7/073024

222. Hill DN, et al. DIII-D research towards resolving key issues for ITER and steady-state tokamaks. *Nucl Fusion* (2013) 53:104001. doi:10.1088/0029-5515/53/10/104001

223. Chen Y, Munsat T, Parker SE, Heidbrink WW, Van Zeeland MA, Tobias BJ, et al. Gyrokinetic simulations of reverse shear Alfvén eigenmodes in DIII-D plasmas. *Phys Plasmas* (2013) 20:012109. doi:10.1063/1.4775776

224. Varela J, Spong D, Murakami M, Garcia L, D'Azevedo E, Van Zeeland M, et al. Subdominant modes and optimization trends of DIII-D reverse magnetic shear configurations. *Nucl Fusion* (2019) 59:046017. doi:10.1088/1741-4326/ab0052

225. Marinoni A, Brunner S, Camenen Y, Coda S, Graves JP, Lapillonne X, et al. The effect of plasma triangularity on turbulent transport: modeling TCV experiments by linear and non-linear gyrokinetic simulations. *Plasma Phys Control Fusion* (2009) 51:055016. doi:10.1088/0741-3335/51/5/055016

226. Camenen Y, Pochelon A, Behn R, Bottino A, Bortolon A, Coda S, et al. Impact of plasma triangularity and collisionality on electron heat transport in TCV L-mode plasmas. *Nucl Fusion* (2007) 47:510–6.

227. Austin ME, Marinoni A, Walker ML, Brookman MW, deGrassie JS, Hyatt AW, et al. Achievement of reactor-relevant performance in negative triangularity shape in the DIII-D tokamak. *Phys Rev Lett* (2019) 122:115001. doi:10.1103/PhysRevLett.122.115001

228. Marinoni A, Austin ME, Hyatt AW, Walker ML, Candy J, Chrystal C, et al. H-mode grade confinement in L-mode edge plasmas at negative triangularity on DIII-D. *Phys Plasmas* (2019) 26:042515. doi:10.1063/1.5091802

229. Van Zeeland MA, Collins C, Heidbrink W, Austin M, Du X, Duarte V, et al. Alfvén eigenmodes and fast ion transport in negative triangularity DIII-D plasmas. *Nucl Fusion* (2019) 59:086028. doi:10.1088/1741-4326/ab2488

230. Ghai Y, Spong D, Varela J, Garcia L, Van Zeeland M, Austin M. Effects of negative triangularity shaping on energetic particle driven Alfvén eigenmodes in DIII-D *. *Nucl Fusion* (2021) 61:126020. doi:10.1088/1741-4326/ac2bc0

231. Pawley C, Crowley B, Pace D, Rauch J, Scoville J, Kellman D, et al. Advanced control of neutral beam injected power in DIII-D. *Fusion Eng Des* (2017) 123:453–7. doi:10.1016/j.fusengdes.2017.02.106

232. Rauch J, Pace DC, Crowley B, Johnson RD, Kellman DH, Pawley CJ, et al. Upgrade to DIII-D National Fusion Facility PCS and Neutral Beam Systems: In-Shot Variation of Neutral Beam Particle Energy. *Fusion Sci Technol* (2017) 72:500–504. doi:10.1080/15361055.2017.1333845

233. Pace DC, Collins C, Crowley B, Grierson B, Heidbrink W, Pawley C, et al. Control of power, torque, and instability drive using in-shot variable neutral beam energy in tokamaks. *Nucl Fusion* (2017) 57:014001. doi:10.1088/0029-5515/57/1/014001

234. Hegna CC, Callen JD. On the stabilization of neoclassical magnetohydrodynamic tearing modes using localized current drive or heating. *Phys Plasma* (1997) 4:2940–6. doi:10.1063/1.872426

235. Erckmann V, Gasparino U. Electron cyclotron resonance heating and current drive in toroidal fusion plasmas. *Plasma Phys Control Fusion* (1994) 36:1869. doi:10.1088/0741-3335/36/12/001

236. Nagasaki K, Motojima G, Fernández AC, Cappa ÁA, Fontdecaba JM, Yoshimura Y, et al. ECCD experiments in heliotron J, TJ-II, CHS, and LHD. *J.Plasca Fusion Res* (2008) 3:S1008. doi:10.1585/pfr.3.s1008

237. Hegna CC, Callen JD. Stability of bootstrap current-driven magnetic islands in stellarators. *Phys Plasma* (1994) 1:3135–7. doi:10.1063/1.870505

238. Yamamoto S, Nagasaki K, Kobayashi S, Nagaoka K, Cappa A, Okada H, et al. Suppression of fast-ion-driven MHD instabilities by ECH/ECCD on Heliotron J. *Nucl Fusion* (2017) 57:126065. doi:10.1088/1741-4326/aa8f04

239. Takeiri Y, Nakamura Y, Noda N, Osakabe M, Kawahata K, Oka Y, et al. Plasma characteristics of long-pulse discharges heated by neutral beam injection in the Large Helical Device. *Plasma Phys Control Fusion* (2000) 42:147–59. doi:10.1088/0741-3335/42/2/307

240. Shimozuma T, Kubo S, Yoshimura Y, Igami H, Nagasaki K, Notake T, et al. Progress on electron cyclotron heating and electron cyclotron current drive experiments in LHD. *Fusion Sci Technol* (2006) 50:403–11. doi:10.13182/fst06-a1262

241. Notake T, Shimozuma T, Kubo S, Idei H, Ida K, Watanabe K, et al. First demonstration of rotational transform control by electron cyclotron current drive in large helical device. *Plasma Fusion Res* (2008) 3:S1077. doi:10.1585/pfr.3.s1077

242. Yoshimura Y, Kubo S, Shimozuma T, Igami H, Takahashi H, Nishiura M, et al. ECCD experiment using an upgraded ECH system on LHD. *Plasma Fusion Res* (2012) 7:2402020. doi:10.1585/pfr.7.2402020

243. Varela J, Cooper W, Nagaoka K, Watanabe K, Spong D, Garcia L, et al. Effect of the tangential NBI current drive on the stability of pressure and energetic particle driven MHD modes in LHD plasma. *Nucl Fusion* (2020) 60:026016. doi:10.1088/1741-4326/ab60cf

244. Sano F, et al. *30th EPS conference on contr. Fusion and plasma phys* (2003). 27A, O-2.2A.

245. Kobayashi S, Okada M, Kaneko Y, Suzuki T, Mizuuchi K, Nagasaki Y, et al. *20th IAEA fusion energy conference* (2004). EX/P4-41.

246. Varela J, Nagasaki K, Kobayashi S, Nagaoka K, Adulsiriswad P, Cappa A, et al. Analysis of the ECH effect on EPM/AE stability in Heliotron J plasma using a Landau closure model. *Nucl Fusion* (2023) 63:026009. doi:10.1088/1741-4326/aca98e

247. Kazakov YO, Van Eester D, Dumont R, Ongena J. On resonant ICRF absorption in three-ion component plasmas: a new promising tool for fast ion generation. *Nucl Fusion* (2015) 55:032001. doi:10.1088/0029-5515/55/3/032001

248. Kazakov YO, Ongena J, Wright JC, Wukitch SJ, Lerche E, Mantsinen MJ, et al. Efficient generation of energetic ions in multi-ion plasmas by radio-frequency heating. *Nat Phys* (2017) 13:973–8. doi:10.1038/nphys4167

249. Kazakov YO, Nocente M, Mantsinen M, Ongena J, Baranov Y, Craciunescu T, et al. Plasma heating and generation of energetic D ions with the 3-ion ICRF + NBI scenario in mixed H-D plasmas at JET-ILW. *Nucl Fusion* (2020) 60:112013. doi:10.1088/1741-4326/ab9256

250. Nocente M, Kazakov Y, Garcia J, Kiptily V, Ongena J, Dreval M, et al. Generation and observation of fast deuterium ions and fusion-born alpha particles in JET D-3 He plasmas with the 3-ion radio-frequency heating scenario. *Nucl Fusion* (2020) 60:124006. doi:10.1088/1741-4326/abb95d

251. Varela J, Spong D, Garcia L, Ohdachi S, Watanabe K, Seki R, et al. Theoretical analysis of the saturation phase of the 1/1 energetic-ion-driven resistive interchange mode. *Nucl Fusion* (2021) 61:126016. doi:10.1088/1741-4326/ac26a0

252. Todo Y, Van Zeeland M, Heidbrink W. Fast ion profile stiffness due to the resonance overlap of multiple Alfvén eigenmodes. *Nucl Fusion* (2016) 56:112008. doi:10.1088/0029-5515/56/11/112008

253. Varela J, Spong D, Todo Y, Garcia L, Ghai Y, Ortiz J, et al. Simulation of the TAEs' saturation phase in the large helical device: MHD burst. *Nucl Fusion* (2022) 62:126020. doi:10.1088/1741-4326/ac8f5a

254. Spong D, Van Zeeland M, Heidbrink W, Du X, Varela J, Garcia L, et al. Nonlinear dynamics and transport driven by energetic particle instabilities using a gyro-Landau closure model *. *Nucl Fusion* (2021) 61:116061. doi:10.1088/1741-4326/ac2990

255. Van Zeeland MA, Bardoczi L, Gonzalez-Martin J, Heidbrink W, Podesta M, Austin M, et al. Beam modulation and bump-on-tail effects on Alfvén eigenmode stability in DIII-D. *Nucl Fusion* (2021) 61:066028. doi:10.1088/1741-4326/abf174

256. Varela J, Spong DA, Garcia L, Ghai Y, Zarzoso D, del-Castillo-Negrete D, et al. Effect of the neutral beam injector operational regime on the Alfven eigenmode saturation phase in DIII-D plasma. *Plasma Phys Control Fusion* (2023) 65:125004. doi:10.1088/1361-6587/ad05d4

257. Van Zeeland MA, Heidbrink WW, Nazikian R, Solomon WM, Austin ME, Berk HL, et al. Reversed shear Alfvén eigenmode stabilization by localized electron cyclotron heating. *Plasma Phys Control Fusion* (2008) 50:035009. doi:10.1088/0741-3335/50/3/035009

258. Hu W, Olofsson K, Welander A, Heidbrink W, Van Zeeland M, Austin M, et al. Active real-time control of Alfvén eigenmodes by neutral beam and electron cyclotron heating in the DIII-D tokamak. *Nucl Fusion* (2018) 58:124001. doi:10.1088/1741-4326/aaddaf

259. Petty CC, et al. Impact of central ECCD on steady-state hybrid scenario in DIII-D. *AIP Conf Proc* (2015) 1689:090002.

260. Mantsinen M, Ingesson LC, Johnson T, Kiptily VG, Mayoral ML, Sharapov SE, et al. Controlling the profile of ion-cyclotron-resonant ions in JET with the wave-induced pinch effect. *Phys Rev Lett* (2002) 89:115004. doi:10.1103/PhysRevLett.89.115004

261. Tobias B, Bass E, Classen I, Domier C, Grierson B, Heidbrink W, et al. Alfvén eigenmode structure during off-axis neutral beam injection. *Nucl Fusion* (2012) 52:103009. doi:10.1088/0029-5515/52/10/103009

262. Tang SX, Carter TA, Crocker NA, Heidbrink WW, Lestz JB, Pinsker RI, et al. Stabilization of alfvén eigenmodes in DIII-D via controlled energetic ion density ramp and validation of theory and simulations. *Phys Rev Lett* (2021) 126:155001. doi:10.1103/PhysRevLett.126.155001

263. Collins CS, Heidbrink WW, Austin ME, Kramer GJ, Pace DC, Petty CC, et al. Observation of critical-gradient behavior in alfvén-eigenmode-induced fast-ion transport. *Phys Rev Lett* (2016) 116:095001. doi:10.1103/PhysRevLett.116.095001

264. Heidbrink WW, Collins CS, Podestà M, Kramer GJ, Pace DC, Petty CC, et al. Fast-ion transport by Alfvén eigenmodes above a critical gradient threshold. *Phys Plasma* (2017) 24:056109. doi:10.1063/1.4977535

265. Chen L, Zonca F. Nonlinear excitations of zonal structures by toroidal Alfvén eigenmodes. *Phys Rev Lett* (2012) 109:145002. doi:10.1103/PhysRevLett.109.145002

266. Qiu Z, Chen L, Zonca F. Nonlinear excitation of finite-radial-scale zonal structures by toroidal Alfvén eigenmode. *Nucl Fusion* (2017) 57:056017. doi:10.1088/1741-4326/aa6413

267. Ge W, Wang ZX, Wang F, Liu Z, Xu L. Multiple interactions between fishbone instabilities and internal transport barriers in EAST plasmas. *Nucl Fusion* (2023) 63:016007. doi:10.1088/1741-4326/aca10c

268. Mazzi S, Garcia J, Zarzoso D, Kazakov YO, Ongena J, Dreval M, et al. Enhanced performance in fusion plasmas through turbulence suppression by megaelectronvolt ions. *Nat Phys* (2022) 18:776–82. doi:10.1038/s41567-022-01626-8

269. Brochard G, Liu C, Wei X, Heidbrink W, Lin Z, Gorelenkov N, et al. Saturation of fishbone instability by self-generated zonal flows in tokamak plasmas. *Phys Rev Lett* (2024) 132:075101. doi:10.1103/PhysRevLett.132.075101

270. Falessi MV, Zonca F. Transport theory of phase space zonal structures. *Phys Plasmas* (2019) 26:022305. doi:10.1063/1.5063874

271. Falessi MV, Chen L, Qiu Z, Zonca F. Nonlinear equilibria and transport processes in burning plasmas. *New J Phys* (2023) 25:123035. doi:10.1088/1367-2630/ad127d

272. Han X, Liu Y, Zhou T, Zhang T, Shi T, Li Y, et al. Dynamics of electron internal transport barrier formation at the H–L transition on EAST. *Nucl Fusion* (2022) 62:064005. doi:10.1088/1741-4326/ac5c75

273. Varela J, Garcia J, Mazzi S, Kazakov Y, Stancar Z, Burazzo M, et al. Simulation of the AE activity in JET D-T discharges using a Landau closure model*. *65th Annual Meeting of the APS Division of Plasma Physics; 2023 Oct 30-Nov 3; Denver, CO, United States* (2023). Available online at: https://meetings.aps.org/Meeting/DPP23/Session/KI02.2.

274. Varela J, Hidalgo C, Tokuzawa T, Nagaoka K, Nagasaki K, Ohdachi S, et al. Shear flows induced by AE / EPM in LHD plasma. *7th Asia-Pacific Conference on Plasma*

Physics; 2023 Nov 12-17; Nagoya, Japan (2023). Available online at: https://www.aappsdpp.org/DPP2023/html/3contents/pdf/5577.pdf.

275. Hemsworth RS, Boilson D, Blatchford P, Palma MD, Chitarin G, de Esch HPL, et al. Overview of the design of the ITER heating neutral beam injectors. *New J Phys* (2017) 19:025005. doi:10.1088/1367-2630/19/2/025005

276. Putvinski SV, et al. Physics of energetic particles in ITER. *Nucl Fusion* (1998) 38: 1275–81. doi:10.1088/0029-5515/38/9/302

277. Fasoli A, Gormenzano C, Berk H, Breizman B, Briguglio S, Darrow D, et al. Chapter 5: physics of energetic ions. *Nucl Fusion* (2007) 47:S264–84. doi:10.1088/0029-5515/47/6/s05

278. Albergante M, Graves JP, Fasoli A, Jenko F, Dannert T. Anomalous transport of energetic particles in ITER relevant scenarios. *Plasma Phys* (2009) 16:112301. doi:10.1063/1.3257913

279. Todo Y, Bierwage A. Large-scale simulation of energetic particle driven magnetohydrodynamic instabilities in ITER plasmas. *Plasma Fusion Res* (2014) 9: 3403068. doi:10.1585/pfr.9.3403068

280. Pinches SD, Chapman IT, Lauber PW, Oliver HJC, Sharapov SE, Shinohara K, et al. Energetic ions in ITER plasmas. *Plasma Phys* (2015) 22:021807. doi:10.1063/1.4908551

281. Lauber P. Local and global kinetic stability analysis of Alfvén eigenmodes in the 15 MA ITER scenario. *Plasma Phys Control Fusion* (2015) 57:054011. doi:10.1088/0741-3335/57/5/054011

282. Schneller M, Lauber P, Briguglio S. Nonlinear energetic particle transport in the presence of multiple Alfvénic waves in ITER. *Plasma Phys Control Fusion* (2016) 58: 014019. doi:10.1088/0741-3335/58/1/014019

283. Brochard G, Dumont R, Lütjens H, Garbet X, Nicolas T, Maget P. Nonlinear dynamics of the fishbone-induced alpha transport on ITER. *Nucl Fusion* (2020) 60: 126019. doi:10.1088/1741-4326/abb14b

284. White RB, Chance MS. Hamiltonian guiding center drift orbit calculation for plasmas of arbitrary cross section. *Fluids B* (1984) 27:2455–67. doi:10.1063/1.864527

285. Chen J, Jian X, Chan VS, Li Z, Deng Z, Li G, et al. Self-consistent modeling of CFETR baseline scenarios for steady-state operation. *Plasma Phys Control Fusion* (2017) 59:075005. doi:10.1088/1361-6587/aa6d20

286. Shi N, Chan VS, Jian X, Li G, Chen J, Gao X, et al. Study of impurity effects on CFETR steady-state scenario by self-consistent integrated modeling. *Nucl Fusion* (2017) 57:126046. doi:10.1088/1741-4326/aa79d1

287. Shi N, Kessel C, Chan V, Guo Y, Chen J, Jian X, et al. The time-dependent simulation of CFETR baseline steady-state scenarios. *Nucl Fusion* (2018) 58:096009. doi:10.1088/1741-4326/aacb3c

288. Zou Y, Chan VS, Chen W, Wang Y, Hou Y, Zhu Y. Energetic particle transport prediction for CFETR steady state scenario based on critical gradient model. *Chin Phys. Lett.* (2021) 38:045203. doi:10.1088/0256-307x/38/4/045203

289. Ishida S, Barabaschi P, Kamada Y. Overview of the JT-60SA project. *Nucl Fusion* (2011) 51:094018. doi:10.1088/0029-5515/51/9/094018

290. Kamada Y, Barabaschi P, Ishida S, Ide S, Lackner K, Fujita T, et al. Plasma regimes and research goals of JT-60SA towards ITER and DEMO. *Nucl Fusion* (2011) 51:073011. doi:10.1088/0029-5515/51/7/073011

291. Sips ACC, Giruzzi G, Ide S, Kessel C, Luce TC, Snipes JA, et al. *Phys Plasma* (2015) 22:021804. doi:10.1063/1.4904015

292. Giruzzi G, Yoshida M, Artaud J, Asztalos Ö, Barbato E, Bettini P, et al. Physics and operation oriented activities in preparation of the JT-60SA tokamak exploitation. *Nucl Fusion* (2017) 57:085001. doi:10.1088/1741-4326/aa7962

293. Casper T, Gribov Y, Kavin A, Lukash V, Khayrutdinov R, Fujieda H, et al. Development of the ITER baseline inductive scenario. *Nucl Fusion* (2015) 54:013005. doi:10.1088/0029-5515/54/1/013005

294. Hanada M, Kojima A, Tanaka Y, Inoue T, Watanabe K, Taniguchi M, et al. Progress in development and design of the neutral beam injector for JT-60SA. *Fusion Eng Des* (2011) 86:835–838. doi:10.1016/j.fusengdes.2011.04.068

295. Kojima A, Umeda N, Hanada M, Yoshida M, Kashiwagi M, Tobari H, et al. Progress in long-pulse production of powerful negative ion beams for JT-60SA and ITER. *Nucl Fusion* (2015) 55:063006. doi:10.1088/0029-5515/55/6/063006

296. Bierwage A, Toma M, Shinohara K. MHD and resonant instabilities in JT-60SA during current ramp-up with off-axis N-NB injection. *Plasma Phys Control Fusion* (2017) 59:125008. doi:10.1088/1361-6587/aa8ae8

297. Coelho R, Vincenzi P, Vallar M, Rodrigues P, Tholerus E, Särkimäki K, et al. Predictive modeling of Alfvén eigenmode stability in inductive scenarios in JT-60SA. *Front Phys* (2023) 11:063006. doi:10.3389/fphy.2023.1267696

298. Adulsiriswad P, Todo Y, Sato M, Aiba N, Narita E, Wang H, et al. Simulation study of interaction between energetic particles and magnetohydrodynamic modes in the JT-60SA inductive scenario with a flat q≈1 profile. *Nucl Fusion* (2023) 63:126030. doi:10.1088/1741-4326/acfcca

299. Varela J, Watanabe K, Shinohara K, Honda M, Suzuki Y, Shiraishi J, et al. MHD stability of JT-60SA operation scenarios driven by passing energetic particles for a hot Maxwellian model. *Nucl Fusion* (2020) 60:096009. doi:10.1088/1741-4326/ab9dd1

300. Varela J, Watanabe KY, Ohdachi S. The internal disruption as hard Magnetohydrodynamic limit of 1/2 sawtooth like activity in large helical device. *Phys Plasmas* (2012) 19:082512. doi:10.1063/1.4747534

301. Varela J, Watanabe KY, Ohdachi S, Narushima Y. Hard magnetohydrodynamic limit in 1/3 sawtooth like activity in LHD. *Phys Plasmas* (2014) 21:032501. doi:10.1063/1.4867066

302. Varela J, Watanabe KY, Ohdachi S, Narushima Y. Magnetic turbulence and pressure gradient feedback effect of the 1/2 mode soft-hard magnetohydrodynamic limit in large helical device. *Phys Plasmas* (2014) 21:092505. doi:10.1063/1.4895499

303. Breizman BN, Arefiev AV, Fomyts'kyi MV. Publisher's Note: "Nonlinear physics of laser-irradiated microclusters" [Phys. Plasmas 12, 056706 (2005)]. *Plasmas* (2005) 12: 112506. doi:10.1063/1.2008263

304. Graves JP, Coste-Sarguet M, Wahlberg C. Pressure driven long wavelength MHD instabilities in an axisymmetric toroidal resistive plasma. *Plasma Phys Control Fusion* (2022) 61:014001. doi:10.1088/1361-6587/ac3496

305. Brochard G, Bao J, Liu C, Gorelenkov N, Choi G, Dong G, et al. Verification and validation of linear gyrokinetic and kinetic-MHD simulations for internal kink instability in DIII-D tokamak. *Nucl Fusion* (2022) 62:036021. doi:10.1088/1741-4326/ac48a6

306. Mikhailovskii AB, Huysmans GTA, Kerner WOK, Sharapov SE Optimization of computational MHD normal-mode analysis for tokamaks. *Plasma Phys Rep* (1997) 23: 844. doi:10.1063/1.3224035

307. Cheng CZ, Chance MS Low-*n* shear Alfvén spectra in axisymmetric toroidal plasmas. *Phys Fluids* (1986) 29:3695–701.

308. Adulsiriswad P, Todo Y, Kado S, Yamamoto S, Kobayashi S, Ohshima S, et al. Numerical investigation into the peripheral energetic-particle-driven MHD modes in Heliotron J with free boundary hybrid simulation. *Nucl Fusion* (2021) 61:116065. doi:10.1088/1741-4326/ac2779

309. Adulsiriswad P, Todo Y, Yamamoto S, Kado S, Kobayashi S, Ohshima S, et al. Effects of the resonance modification by electron cyclotron current drive on the linear and nonlinear dynamics of energetic particle driven magnetohydrodynamics modes in Heliotron J. *Nucl Fusion* (2024) 64:016036. doi:10.1088/1741-4326/ad0a0c

310. Duarte B, Kerner W. CASTOR-K: stability analysis of Alfvén eigenmodes in the presence of energetic ions in tokamaks. *J Comput Phys* (1999) 153:101–38.

311. Borba D, Berk HL, Breizman BN, Fasoli A, Nabais F, Pinches SD, et al. Modelling of Alfvén waves in JET plasmas with the CASTOR-K code*. *Nucl Fusion* (2002) 42:1029–38.

312. Imbeaux F, Pinches S, Lister J, Buravand Y, Casper T, Duval B, et al. Design and first applications of the ITER integrated modelling and analysis suite. *Nucl Fusion* (2015) 55:123006. doi:10.1088/0029-5515/55/12/123006

313. Gorelenkov NN, Berk H, Budny R. Beam anisotropy effect on Alfvén eigenmode stability in ITER-like plasmas. *Nucl Fusion* (2005) 45:226–37. doi:10.1088/0029-5515/45/4/002

314. Chen Y, Parker SE, Lang J, Fu GY. Linear gyrokinetic simulation of high-n toroidal Alfvén eigenmodes in a burning plasma. *Phys Plasmas* (2010) 17:102504. doi:10.1063/1.3490213

315. Figueiredo ACA, Rodrigues P, Borba D, Coelho R, Fazendeiro L, Ferreira J, et al. Comprehensive evaluation of the linear stability of Alfvén eigenmodes driven by alpha particles in an ITER baseline scenario. *Nucl Fusion* (2016) 56:076007. doi:10.1088/0029-5515/56/7/076007

316. Bass EM, Waltz R. Prediction of Alfvén eigenmode energetic particle transport in ITER scenarios with a critical gradient model. *Nucl Fusion* (2020) 60:016032. doi:10.1088/1741-4326/ab54fb

317. Hayward-Schneide T, Lauber P, Bottino A, Lu Z. Global linear and nonlinear gyrokinetic modelling of Alfvén eigenmodes in ITER. *Nucl Fusion* (2021) 61:036045. doi:10.1088/1741-4326/abdca2

318. Varela J, Garcia J, Mazzi S, Kazakov Y, Štancar Ž, Baruzzo M, et al. *31st meeting of ITPA topical group on energetic particle physics EP20 - id51*. contibuted talk; Apr 16–18; Daejeon, South Korea (2024).

319. Varela J, et al. *FY'24 US-Japan MHD workshop 43rd ITPA MDC TG meeting* (2024). In: contributed talk.

320. Varela J, Nagaoka K, Takemura Y, Watanabe KY, Ida K, Yoshinuma M, et al. MHD stability trends and improved performance of LHD inward shifted configurations: the role of the neutral beam current drive and thermal plasma density. *Phys Plasmas* (2024) 31. under review. doi:10.1063/5.0206400

321. Betar H, et al. Transport and losses of energetic particles in tokamaks in the presence of Alfvén activity using the new full orbit TAPaS code coupled to FAR3d. *Nucl Fusion* (2024). under review.

322. Melnikov AV, Eliseev L, Jiménez-Gómez R, Ascasibar E, Hidalgo C, Chmyga A, et al. Internal measurements of Alfvén eigenmodes with heavy ion beam probing in toroidal plasmas*. *Nucl Fusion* (2010) 50:084023. doi:10.1088/0029-5515/50/8/084023

323. Melnikov AV, Eliseev L, Castejón F, Hidalgo C, Khabanov P, Kozachek A, et al. Study of NBI-driven chirping mode properties and radial location by the heavy ion

beam probe in the TJ-II stellarator. *Nucl Fusion* (2016) 56:112019. doi:10.1088/0029-5515/56/11/112019

324. Melnikov AV, Ascasibar E, Cappa A, Castejón F, Eliseev L, Hidalgo C, et al. Detection and investigation of chirping Alfvén eigenmodes with heavy ion beam probe in the TJ-II stellarator. *Nucl Fusion* (2018) 58:082019. doi:10.1088/1741-4326/aabcf8

325. Collins CS. *Fusion REactor Design and Assessment (FREDA): enabling whole facility modeling and optimization via advanced simulation of integrated physics and engineering*. Oak Ridge National Laboratory ORNL (2023).

326. Leboeuf JN, Lynch VE, Carreras BA, Alvarez JD, Garcia L. Full torus Landau fluid calculations of ion temperature gradient-driven turbulence in cylindrical geometry. *Phys Plasmas* (2000) 7:5013–22. doi:10.1063/1.1323757

327. Johnson JL, Oberman CR, Kulsrud RM, Frieman EA. Some stable hydromagnetic equilibria.*Phys.Plasmas* (1958) 1:281–296.

328. Mukhovatov VS, Shafranov V. Plasma equilibrium in a tokamak. *Nucl Fusion* (1971) 11:605–33. doi:10.1088/0029-5515/11/6/005

329. Anania G, Johnson JL. Application of the stellarator expansion for plasma stability studies in stellarators. *Phys.Fluids* (1983) 26:3070–8. doi:10.1063/1.864031

330. Dimits AM, Joseph I, Umansky MV. A fast non-Fourier method for Landau-fluid operators. *Phys Plasmas* (2014) 21:055907. doi:10.1063/1.4876617

331. Freidberg JP. *Plasma physics and fusion energy*. Cambridge University Press (2007). doi:10.1017/CBO9780511755705